Philipps Universität Marburg

Open Microwave Systems: Tunneling, Correlations and Time-Dependent Variations

Dissertation

zur

Erlangung des Doktorgrades

der Naturwissenschaften

(Dr. rer. nat.)

dem

Fachbereich Physik

der Philipps-Universität Marburg

vorgelegt von

Stefan Gehler

aus Gera

Marburg/Lahn 2013

Vom Fachbereich Physik der Philipps-Universität Marburg/Lahn
als Dissertation angenommen am 09.09.2013
Erstgutachter: Prof. Dr. U. Kuhl
Zweitgutachter: Prof. Dr. B. Eckhardt
Tag der mündlichen Prüfung: 16.09.2013
Hochschulkennziffer 1180

Abstract

In this thesis three possibilities of external influences in wave mechanical systems are analyzed. In all three cases I used microwave devices to study quantum mechanical systems. The first analyzed property is the decay rate from states in so-called regular islands in a billiard system to the chaotic sea. Afterwards I characterize the influence of open decay channels in transport through chaotic wave systems. The last topic is the introduction of a time-dependently changed microwave device.

In the first chapter the decay of a wave function from one classically isolated phase space region to another is analyzed. The main interest lies on the influence of additional states corresponding to the same original phase space region. I will show that these states can lead to an enhancement of the decay rate. The decay rates are measured via an indirect absorption process, leading to an increase of the corresponding resonance widths. Alternatively to mode depending width properties, which were typically analyzed in numerical calculations, a parameter depending variation of the system is introduced to verify the demanded effect.

The experimental and numerical determination of channel correlations are the subject of the second chapter. After defining the correlation function, an experimental demonstration is presented. The results of the experiment and the describing numerics show that the correlation functions are important for the characterization of universal conductance fluctuations.

The last chapter deals with the realization of a periodically driven microwave system. The principal setup is a resonant circuit with a time-dependent capacity. The properties of the setup, e.g. sideband structures for different driving signals, are analyzed experimentally, theoretically and numerically. This is the first step to create a system where a huge subset of resonances is changed. The fulfilled description of the single resonance system is presented and the next steps to realizations of time-dependent driven wave mechanical systems are sketched.

Zusammenfassung

In dieser Arbeit werden drei Möglichkeiten äußerer Einflüsse auf wellenmechanische Systeme analysiert. In allen drei Fällen nutze ich Mikrowellensysteme, um quantenmechanische Systeme zu simulieren. Zuerst werden Zerfallsraten von Wellenfunktionen, die in sogenannten regulären Inseln von Billard-Systemen konzentriert sind, untersucht. Danach wird der Einfluss von offenen Zerfallskanälen auf den Transport durch chaotische Wellensysteme charakterisiert. Das letzte Thema ist ein zeitlich veränderliches Mikrowellen-System.

Im ersten Kapitel wird der Übergang einer Wellenfunktion eines klassisch isolierten Bereichs des korrespondierenden Phasenraums zu einem anderen analysiert. Das Hauptaugenmerk liegt auf dem Einfluss von zusätzlichen Zuständen des ursprünglichen Phasenraumbereichs. Es wird gezeigt, dass diese Zustände zu einer Steigerung der Zerfallsrate führen können. Die Zerfallsraten werden indirekt über Absorption gemessen, was zu einem Anstieg der entsprechenden Resonanzbreiten führt. Zusätzlich zu dem sonst üblichen modenabhängigem Tunnelverhalten, welches typischerweise in numerischen Berechnungen genutzt wird, ist eine parametrische Änderung des Systems durchgeführt worden. Dadurch wurde der Nachweis des Effekts zusätzlich untermauert.

Die experimentelle und numerische Bestimmung von Kanal-Korrelationen sind Gegenstand des zweiten Kapitels. Nach der Definition der Korrelationsfunktion wird das experimentelle Modellsystem vorgestellt. Die Ergebnisse des Experiments und der sie beschreibenden Numerik zeigen, dass die Korrelationsfunktionen bei der Beschreibung der allgemeinen Leitwertfluktuationen nicht vernachlässigbar sind.

Das letzte Kapitel beschäftigt sich mit der Realisierung eines periodisch angetriebenen Mikrowellen-Systems. Der prinzipielle Aufbau ist ein Schwingkreis mit einer zeitlich veränderbaren Kapazität. Analysiert werden die Eigenschaften des Systems, wie die Seitenbandstrukturen für verschiedene Treibungssignale, sowohl experimentell, als auch theoretisch und numerisch. Dies ist der erste Schritt zur Konstruktion eines Systems, in welchem ein großer Teil der Resonanzen durch einen äußeren Parameter verändert werden kann. Die vollständige Beschreibung einer einzelnen getriebenen Resonanz wird vorgestellt und die nächsten Schritte zur Realisierung von zeitabhängig getriebenen wellemechanischen Systemen werden gezeigt.

Contents

Introduction **1**

I. Experimental observation of resonance-assisted tunneling **5**
I.1. Motivation 6
I.1.1. Dynamic tunneling in systems with mixed phase space 6
I.1.2. Resonance-assisted tunneling 7
I.2. Experimental proof of the existence of resonance-assisted tunneling . 10
I.2.1. Model system, experimental realization and its characterization 10
I.2.2. Brief description of numerically calculated results 22
I.2.3. Frequency dependent tunneling rates 23
I.2.4. Parametric proof of resonance-assisted tunneling 26
I.3. Conclusion 33

II. Channel correlation in transport through chaotic wave mechanical systems **35**
II.1. Motivation 36
II.1.1. Random matrix theory 36
II.1.2. From Ericson to conductance fluctuations 37
II.1.3. How do microwave cavities mimic nuclei scattering? 38
II.2. Definition of channel correlations 40
II.3. Experimental setup and data evaluation 42
II.3.1. Experimental setup - characteristics 42
II.3.2. Numerical calculations 46
II.3.3. Experimental results 46
II.4. Conclusion 50

III. Realization of a microwave Floquet system **51**
III.1. Motivation 52

III.2. Single driven resonance - linear regime 53
III.2.1. Experimental setup 53
III.2.2. Preliminaries 58
III.2.3. Sidebands generated by a single driven resonance 59
III.2.4. Experimental results 66
III.3. Single driven resonance - nonlinear regime 75
III.3.1. Nonlinear microwave Floquet system 78
III.4. Driven systems with several resonances 82
III.4.1. Microwave cavity 82
III.4.2. Graphs 85
III.5. Conclusions 88

Appendix **V**

A. Mimicking quantum mechanics with microwave equipment VI
B. Spectra for stronger couplings VII
C. Frequency depending tunneling rates - alternative analysis; other antenna position VIII
D. Parametric dependence of divers modes X
E. Resonance-assisted tunneling description by (2×2)-model XVI
F. Width characteristics by opening an one dimensional potential well by one realistic absorbing wall XVIII
G. Scattering theory for open quantum mechanical systems XX
H. Global phase calibration XXI
I. Capacity and inductivity of the tin cup XXII
J. Analytic calculation of sidebands generated by rectangular driving . XXIII
K. Foldover in a nonlinear RLC-circuit XXVI

Bibliography **XXIX**

Introduction

Properties of quantum mechanical systems coupled to their environment, so-called open quantum mechanical systems, generated great attention within the last twenty years. The main reason might be the missing understanding of the process when a quantum mechanical system looses its phase information and is becoming a classical mechanical system. This transition is tried to be caught with decoherence models [1] and was a subject of my own former work [2, 3]. But also for pure quantum mechanical systems the openness is a very important property. Every measurement of a quantum mechanical system means opening it. Decay processes of e.g. nuclei can be characterized as open channels [4]. Even a laser is nothing else but many coherent quantum mechanical states coupled to the environment via a partial mirror.
In this thesis I will present three wave mechanical systems which are either opened by absorbers or coupled channels, or perturbed by an external source. All three projects are in the progress of publication as independent works [5, 6, 7].
In addition all three studied systems are motivated by quantum chaos. Quantum chaos might be a misleading term. The Schrödinger equation cannot produce chaos in a meaning of trajectories which diverge exponentially fast. This is due to the linear time derivative and the impossibility of defining trajectories in quantum mechanics. Quantum chaos refers to the quantum mechanical properties of corresponding classical chaotic systems.
One can speak of wave mechanical and quantum mechanical systems up to here synonymously, because one can mimic quantum mechanics with a flat electromagnetic cavity. The fundamental derivation of the equivalence of the time independent Schrödinger equation and the Helmholtz equation, which describes the electromagnetic cavity is shown in the appendix A.

Already Poincaré found out, that classical Hamiltonian systems can lead to irregular so-called chaotic behaviors. Many problems in classical mechanics seem

regular, e.g. pendula and two body systems. But in fact, the next complicated systems like a three body system can show an irregular behavior. But the physical world is not divided into regular and chaotic systems. As we know from the system concerning the sun, the moon and the earth, there are also in three body systems regular solutions, otherwise life on earth would not be possible. In the first chapter we are interested in systems, which can show both regular and chaotic behavior. That means that in these system it depends on the initial conditions, if the motion is regular or chaotic. Classically it is not possible to start at one region of the phase space and end up in the other region. In quantum mechanics this is possible due to tunneling. I will introduce the effect of dynamical tunneling from one classical phase space region to another which is separated due to its classical dynamics in this chapter. As it will be shown, this effect can be enhanced by the presence of additional states in the original phase space region. The enhancement is called resonance-assisted tunneling and its experimental observation will be the topic of the first chapter. Until now, only the coupling between two regular resonances for a nearly integrable system was measured before [8].

In the second chapter of the thesis I will deal with the results of properties which are typical for random matrix theory. This theory is suited to calculate both analytically and numerically spectral properties of fully chaotic systems [9]. Mainly spectral correlations like nearest neighbor distance distribution of the eigenenergies can be calculated exact within this theory [10]. I will show experimental data and numerical calculations for the correlation of the cross sections (σ_{ab}) between different channels (a, b, c, d) like $C = \overline{\langle \sigma_{ab}\sigma_{cd}\rangle} - \overline{\langle \sigma_{ab}\rangle\langle \sigma_{cd}\rangle}$.
We call this correlation function "channel correlation" to distinguish it from already analyzed correlations [11]. A complete definition will be given in the main part (section II.2).
The correlation function is firstly interesting by itself. Would one expect that the cross section between two different channels, which is in our case the transport probability, is correlated with the cross section between two other channels? Especially if one is interested in the correlation as function of the channel coupling in a regime, where the transport is not generated by a single mode of the system.
It turns out that the correlation with one index in common (either $a = c$ or $b = d$) is anticorrelated to the correlation with no index in common.
In the context of universal conductance fluctuations [12, 13] for the transmission

through a chaotic medium, correlation functions of this type play an important role. Continuum shell model calculations [14, 15, 16] show that the correlation functions contributes in a non negligible way [17]. A discrepancy by a factor of 2 appears if one neglects these two correlation functions. I will give a short overview in section II.1.2 of the universal conductance fluctuations and their relation to Ericson fluctuations.
I will present experimental results and compare them with numerics of random matrices. A good agreement is found.

The third chapter deals with periodically driven wave systems. Periodically driven or kicked quantum systems attract significant interest due to the substantial difference from their classical analogs. Already a simple model of the kicked rotor [18] shows a saturation of the linear raise of energy of a particle as a function of the number of kicks. This phenomenon was called dynamical localization due to its similarity to Anderson localization [19, 20]. There were a few experimental demonstrations using either highly excited hydrogen atoms (Rydberg atoms) in strong microwave fields [21] or ultra-cold atoms within optical traps [22, 23]. However, these experiments require a rather complicated experimental setup and usually do not provide a possibility for a large variation of parameters. The main and also future goal is to introduce a microwave experiment, where an intuitive and comprehensible description of dynamical localization is possible.
Up to now only time-independent systems have been studied with microwave techniques. To realize time-dependent microwave cavities one has to vary either the physical shape, i.e. moving a wall or inset, or its electrical properties. The introduction of a device being the first step of a realization of time-dependent microwave setups is the subject of the third chapter. I will show that a simple circuit with an integrated changeable capacity obeys all basic requirements. The setup was started to be analyzed already in my Diploma thesis [3]. There arose a lot of problems with an adequate description of the setup and also teething troubles with new measurement equipment had to be overcome. Meanwhile these problems could be solved.
Since the changeable capacity is performed by a varicap, nonlinear effects can arise. Firstly, I will restrict myself to the linear regime, but the nonlinear regime will be introduced in a later section.
The chapter is structured in the following way: At first I introduce the experimental resonance circuit and characterize its properties by static measurements. In section

III.2.2 I give hand waving arguments for some of the expected results. Thereafter, I derive theoretically the sideband structure characteristics for different drivings in the single resonance approximation and compare them to numerical calculations. In section III.2.4 I present the experimental Floquet results and compare them to the theoretical predictions (see III.2.3) and numerics. The investigation and theoretical as well as numerical comparison of the experimental results are in the process of publishing [7].
As future works I will present the investigation of nonlinear effects for the single driven system. At the end I will show the next and probably the most complicated step to construct two setups, where more than one resonance can be varied by an external parameter. This opens up the field of time-dependent wave mechanical systems.

I. Experimental observation of resonance-assisted tunneling

I.1. Motivation

The investigation of resonance-assisted tunneling is of course not the first step to understand quantum mechanical systems with a mixed phase space [24]. During the last 30 years many publications with great relevance appeared on this topic. From statistical properties like amplitude distributions [25], autocorrelation functions [26] and trace formulas [27, 28] to Weyl law characterizations [29, 30] many questions were asked and answered. Also microwave experiments were used to investigate this topic [31, 32], mainly on direct tunneling from regular islands to the chaotic sea.

I.1.1. Dynamic tunneling in systems with mixed phase space

Tunneling through a potential barrier is one of the first examples physicists tell people without an education in physics to demonstrate counterintuitive propositions in quantum mechanics. Also in the basic lectures on quantum mechanics it plays an important role due to its easy applicability in many fields of modern physics (scanning tunneling microscopy [33], radioactive decay [34], etc.). The main issue is that the quantum mechanical wave function decays exponentially in a potential barrier with a higher energy than the considered state and if the barrier is ending, the state has a remaining probability density proportional to e^{-cd}. Here d is the length of the wall and c is the so-called tunneling rate, which depends on the height and the width of the barrier. This means a quantum particle can tunnel through such a barrier, hence one speaks from a tunneling process.

Going one step further in a quantum mechanics lecture, one can see that the tunneling effect leads to a break down of degeneracy if two identical potential wells are coupled via a finite barrier [35, 36]. Sometimes students have to calculate the spectrum of the double-well-potential to test semiclassical methods, namely the WKB-approximation [37], where one can see the connection between the tunneling rate c and the level repulsion of the ground state. The tunneling effect is leading to mixed wave functions due to a non vanishing overlap.

In 1981 Davis and Heller discovered in numerical calculations of vibrational modes of molecules exactly such a mixing of modes [38]. The surprising new finding was that the two mixing modes belonged to two different parts of the classical phase

space. This means in analogy to the double-well potential that tunneling from one classically isolated area to another is possible. They called this effect "dynamic tunneling" to distinguish it from tunneling through a potential barrier, which is not existing in this context. From the mixing of the modes and the level repulsion of the concerned eigenenergies a tunneling rate can be extracted.

As a conclusion to the similarity to the double-well potential, the tunneling rate γ determines the exponential decay for one state placed at one part of the phase space towards another classical region of the phase space. In theoretical investigations of this tunneling effect typically the tunneling from a state inside a regular island to the surrounding chaotic sea is analyzed.

A natural question is now, how this tunneling rate behaves as a function of $1/h_{\text{eff}}$. Here h_{eff} is the effective Planck constant and means the ratio $\frac{h}{S}$ of the Planck constant and the typical action of the system. Typically this means that for increasing energies, $1/h_{\text{eff}}$ goes to zero. Since one is going to the semiclassical regime it is clear that the tunneling rate has to decrease, because tunneling is impossible in classical mechanics. In fact Hansen, Ott and Antonsen showed some years after Davis and Hellers finding that the tunneling rate decreases exponentially as a function of $1/h_{\text{eff}}$ [39].

I.1.2. Resonance-assisted tunneling

It took almost twenty years until deviations were found, now in the dependence of the tunneling rate γ on $1/h_{\text{eff}}$, in numerical calculations of maps with mixed phase space. The observed deviations showed sharp peaks and plateaus at certain values of $1/h_{\text{eff}}$ and could thus not be explained by a simple correction of the exponent. In figure I.1 an overview of this effect is given (with kind permission of the authors of [40], here the standard map is used). In the lower left corner one can see the classical phase space with one regular island (red) and the chaotic sea (blue). The blue points correspond to the numerically evaluated tunneling rates for different modes. At the beginning one can see the overall exponential decay (predicted by [39]) of the tunneling rates for the different modes (blue points) as a function of $1/h$, in particular for the first seven or eight resonances. The main deviations are manifested in the relatively sharp peaks e.g. at $1/h \sim 30$ (note that the authors are using dimensionless units).

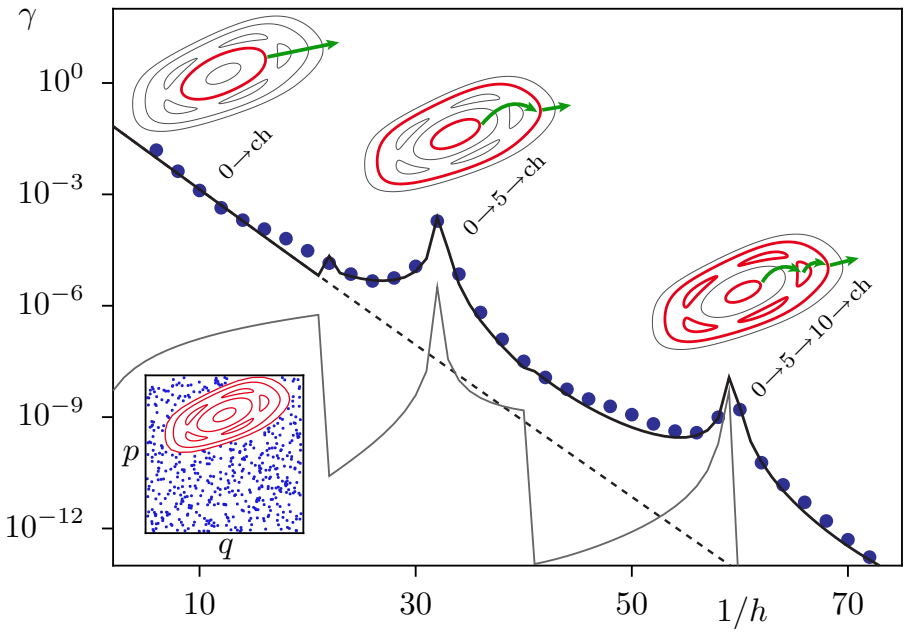

Figure I.1.: Tunneling rates for an one dimensional kicked system as a function of $1/h$ (with kind permission of the author of [40]). In the lower left corner the corresponding classical phase space representation (red regular islands, blue chaotic sea) is shown. The points are the numerical results. The grey lower solid line corresponds to semiclassical calculations. The dashed line is predicted by only considering direct dynamical tunneling. The solid line, which is in nearly perfect agreement with the numerical points, is quantum mechanical theory considering resonance-assisted tunneling. The phase space sketched above the lines symbolizes the pathways of resonance-assisted tunneling (Copyright 2010 by the American Physical Society).

Heuristically, these peaks can be understood as possible enhancement of the tunneling if the eigenstate in the center of the island is coupled to a regular state which is living closer to the boundary of the two areas (see for example the sketch above the peak at $1/h \sim 30$). This second regular state can tunnel much faster to the chaotic sea. Of course these two regular states need to have nearby energy levels. The enhancement could be described semiclassically some years ago [41, 42]. In this system the grey solid line corresponds to the semiclassical calculations. As this system is the standard map, it is even possible to find an expression for the tunneling rate (solid black line, [40]), which combines direct and resonance-assisted tunneling.

Up to now it is not possible to find such an expression for an arbitrary billiard system. The problem is that one needs a fictitious integrable system to calculate the overlap of the regular modes with the chaotic sea. There are a few examples where it seems to be not so hard to find an adequate fictitious integrable system [43]. This is the main reason why in the following chapter experimental data can be compared only to numerical results. Nevertheless, time will show if there will be an adequate analytical expression for resonance-assisted tunneling in billiard systems.

I.2. Experimental proof of the existence of resonance-assisted tunneling

I.2.1. Model system, experimental realization and its characterization

In the following part of this thesis an introduction to the model system and its experimental realization is given.

First one should clarify which requirements have to be fulfilled by the experiment. Afterwards one can think about optimizations and issues that might improve the recognizability of resonance-assisted tunneling.

Model system

To show resonance-assisted tunneling in a billiard system it is necessary to have a system with a mixed phase space. Additionally one needs a periodic orbit structure which couples better to the continuum. For simplicity, a sharp boundary between the regular islands and the chaotic sea without a hierarchical structure of smaller islands is preferable. Then in the best case only one periodic orbit near the boundaries can enhance the quantum mechanical tunneling rate.

In collaboration with my colleagues in Dresden we decided to use a desymmetrized cosine shaped billiard. In figure I.2 (a) the boundary of the billiard is plotted, in (c) and (e) the phase spaces are shown (for aesthetic reasons the phase space of the fully symmetrized billiard (mirrored at the left boundary) is plotted). Every point in the phase space (precisely one should speak about the Poincaré section) corresponds to a collision of a point-like ball with the boundary. The abscissa refers to the place at the boundaries (circumference scaled to 1; started at the right lower corner) and the ordinate represents the sine of the incidence angle of the incoming ball to the boundary. The blue points mark the chaotic sea. In red and orange one can see the regular island structure.

The parameters of the billiard (amplitude of the cosine and distance to the bottom wall) are chosen in such a way that the period 3 orbit (see figure I.2 (c),(e) in orange, notice that for the symmetric billiard the period 3 orbit becomes a period 6 one,

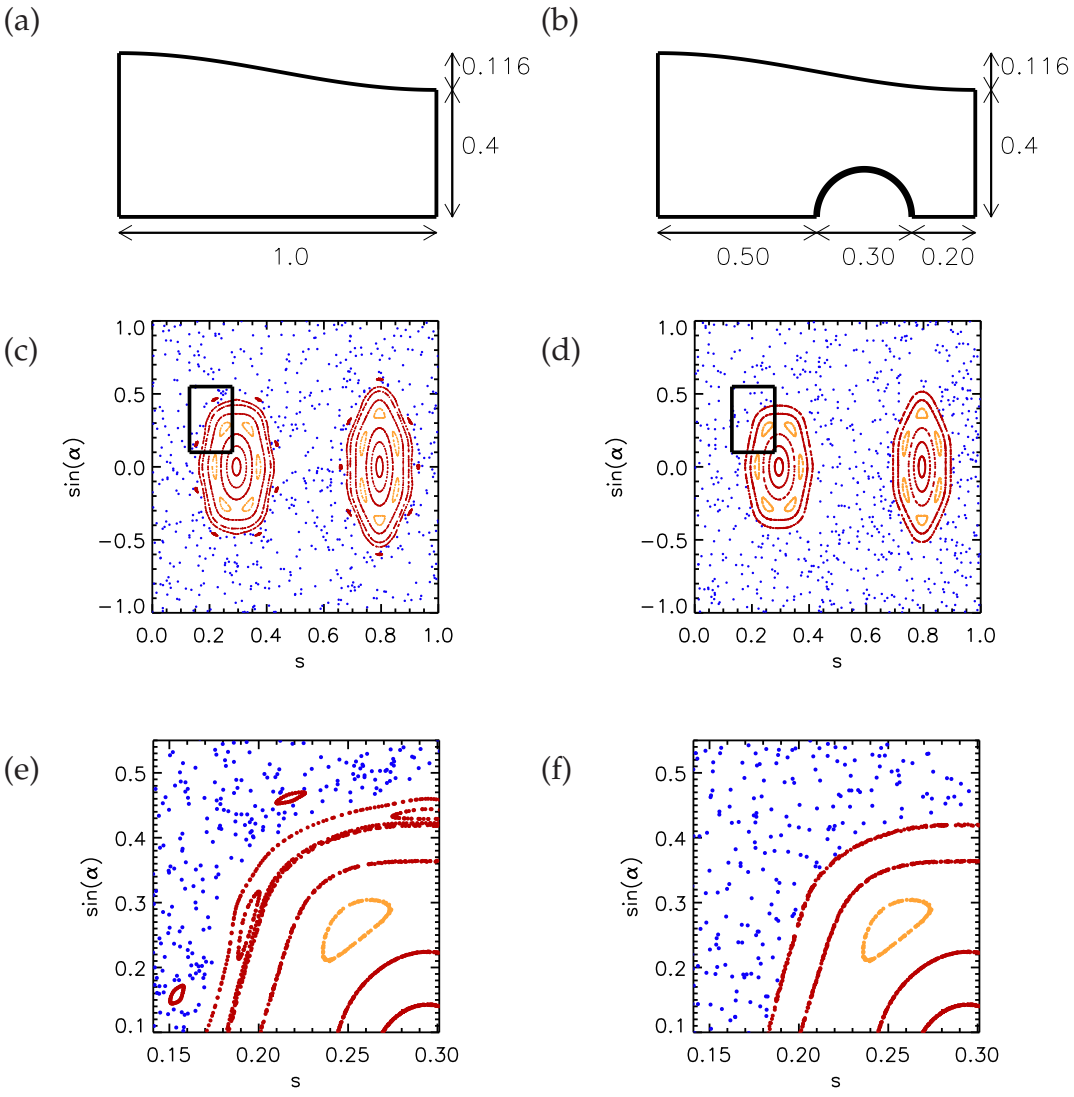

Figure I.2.: Sketch of cosine shaped billiards (a) and (b) and their classical phase space representations (for aesthetic reasons the Poincaré plot of the symmetrized billiard (mirrored on the left wall) is plotted). The phase spaces (c) and (d) correspond to the billiards (a),(b) respectively, where (e), (f) show zooms to the black boxes in (c), (d).

thats why one can see 6 orange islands in (c) and (d)) of the regular island cover a huge area in the island.

To avoid the hierarchical structure and to give the modes corresponding to the period 3 orbits a sufficient high direct tunneling rate we placed a half circle on the bottom boundary (figure I.2 (b)). One can see that this does not affect the regular orbits up to a critical value. At that value there is now a clear boundary between the regular island and the chaotic sea. It can be seen that now the hierarchical island structure in the chaotic sea is destroyed (compare figure I.2 (e) and (f)) and in the wave mechanical situation only via the period three orbit an enhancement of the tunneling rate is expected.

The main advantage of this system is the simplified extraction of the tunneling rates. In former experiments [31] one had to analyze the avoided crossings of regular modes with chaotic ones. This complicated extraction of tunneling rates is in the current device not longer necessary. The wave functions belonging to the two different parts of the classical phase space are differently distributed in position space and thus the tunneling can be extracted by introducing an absorber.

Therefore in figure I.3 (a) and (b) regular and chaotic classical orbits are plotted. Below (figure I.3 (c) and (d)) one can see typical quantum mechanical wave functions [1]. The wave functions corresponding to the regular orbits show a nice similarity to wave functions of a rectangular billiard (infinite high two dimensional rectangular potential well). To classify these wave functions we introduce a horizontal (n) and vertical (m) wave number. In the case of figure I.3 (c) it is $n = 2, m = 17$. We will call resonances with a horizontal wave number $n = 1$ up to now first modes, with $n = 2$ second modes and so on. Only the chaotic modes are spread over the whole billiard, whereas the regular modes are concentrated near the left wall. This can be understood from a semiclassical point of view. Regular classical orbits like in figure I.3 (a) are concentrated near the left wall. The focussing first part of the cosine is leading to stable periodic orbits. An arbitrary chaotic orbit (figure I.3 (b)) shows that the corresponding wave function should also spread over the whole billiard (compare figure I.3 (d)). This is in accordance with the so called semiclassical eigenfunction hypothesis which predicts, that the eigenstates only concentrate on one part of the divided phase space, either the regular islands or the chaotic

[1] At this place I want to thank Steffen Löck for his procedures to calculate the quantum mechanical wave functions in Python.

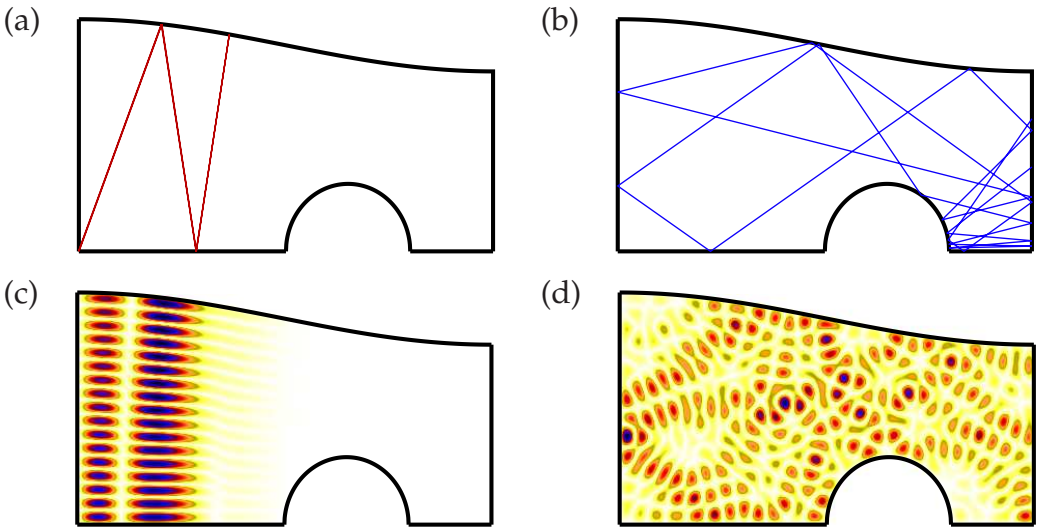

Figure I.3.: Regular (a) and chaotic (b) periodic orbits. Arbitrary wave functions from the regular island (c) and from the chaotic sea (d).

sea [44, 45]. This hypothesis can be understood as a consequence of the correspondence principle. In the limit of classical mechanics states have to concentrate along the classical orbits.

This spatial separation of the regular wave function is directly leading to the idea of placing an absorber at the right part of the billiard. Thereby we identify the chaotic sea with the continuum. If the absorber is working well, the chaotic modes should not be observable anymore. In addition the tunneling rate which predicts the time constant of the exponential, now predicts the decay to the absorber. Under the assumption that the absorber works perfectly, the tunneling rate can be identified directly with the time constant of the decay of the whole wave function itself. By a Fourier transformation the decaying exponentials in the time domain transform to Lorentz curves in frequency domain [46, 47]. The decay rates are thus related to the widths of the measured microwave resonances.

The modes belonging to the inner part of the regular island (red lines in figure I.2 (f), right bottom) have horizontal wave numbers of $n = 1, 2$ or 3. The horizontal fourth, fifth, and sixth modes are corresponding to the period three orbits (in orange in figure I.2 (d) and (f)). Thinking of a situation like in figure I.1 the tunneling rate of the first modes can be enhanced by the fourth, the tunneling rate of the second modes by the fifth and so on.

(a) (b)

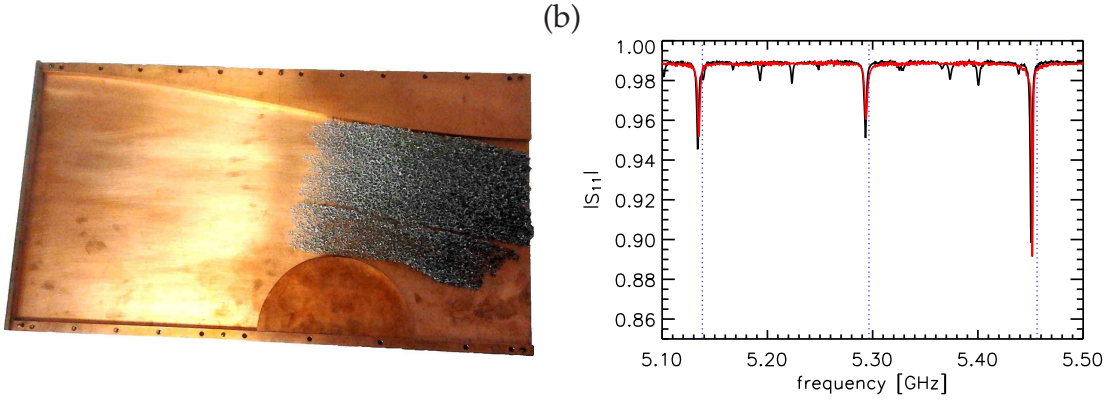

Figure I.4.: Photograph of cosine shaped billiard (a) and typical spectra (b). On the photograph one can see the copper cavity with a size of 60 cm × 30.96 cm × 1 cm and the absorber (grey foam mat right). In (b) in black the spectrum for the closed cavity without absorbers, in red the spectrum for the open system (with absorbers) and in the blue dashed lines the numerically calculated positions for the regular states.

Experimental setup and data evaluation

A photograph of the setup is shown in figure I.4 (a). The resonator is fabricated by the mechanical workshop with a precision of 0.1 mm out of oxygen free copper, which has a high conductivity to minimize the Ohmic losses (compare figure I.6 and corresponding text passage (equation (I.6))). The height of the cavity is 1 cm so by equation (A.3) for frequencies up to 15 GHz only TM_0 modes are excited and the describing Helmholtz equation is fully equivalent to the two dimensional Schrödinger equation (compare appendix A).

The length of the resonator is 60 cm and the width is on the left side 30.96 cm and on the right side 24 cm. At the bottom boundary one can see the movable half circle with a radius of 18 cm. The black foam mat is the absorber. With a rough estimate one can see, that the absorber works in a frequency range from $\frac{\text{speed of light}}{\text{length of absorber}} \sim \frac{300000\,\text{km/s}}{20\,\text{cm}} \sim 1.5\,\text{GHz}$ (the absorber should be at least as long as the wavelength) to $\frac{\text{speed of light}}{\text{mean free path}} \sim \frac{300000\,\text{km/s}}{1\,\text{cm}} \sim 30\,\text{GHz}$ (the substructure of the absorber should be at least of the order of the wavelength). In figure I.4 (b) one can see how good the absorber is working. In red the spectrum with absorber is plotted. In the background the black curve is a spectrum without the absorber and a closed right end (the left end is of course every time closed). The vertical blue

dashed lines indicate the numerically calculated regular resonances. One can see a very good agreement according to our argumentation. The regular modes are minimally affected, whereas modes not related to the islands are so much broadened that they cannot be observed in the red spectrum anymore. Indirectly the regular modes should be affected by resonance-assisted tunneling, but in this plot (figure I.4 (b)) this is not observable.

It is known for years that for microwave billiards with a cylindric dipole antenna the so called billiard-Breit-Wigner formula describes the scattering matrix similar to nuclear physics [9, 48, 49, 50]:

$$S_{11}(\nu,\vec{r}_1) = 1 - i\sum_n \frac{\mathrm{Re}(\lambda)\psi_n(\vec{r}_1)\psi_n^*(\vec{r}_1)}{\nu^2-\nu_n^2-\frac{i}{2}\Gamma_n}; \quad \Gamma_n = 2\mathrm{Re}(\lambda)\psi_n(\vec{r}_1)\psi_n^*(\vec{r}_1). \tag{I.1}$$

The widths Γ_n of these resonances are just appearing by opening the system due to the measurement. That is why they are also called the antenna widths. The width depends on the coupling parameter λ of the antenna (typically frequency dependent) and on the magnitude of the wave function at the position of the antenna. In principle the coupling is additionally leading to a shift of the resonance position. Due to the fact, that we do not want to compare the position with theoretically or numerically evaluated positions, we neglect this shift. The constant 1 in equation (I.1) is not realizable in the experiments. Due to the finite length of the dipole antenna and the occurring capacity by the passing of the antenna through the top plate there is an additional phase response of the reflection signal. This phase response can be either calibrated by a phase calibration (as it will be done in the experiments in chapter II, compare appendix H) or considered by fitting the underground of the reflection signal and taking the modulus of the amplitude. In this special situation we are interested in the properties of sharp resonances and a phase calibration cannot be performed in an accuracy of the order of the widths of the resonances. So taking the modulus of the amplitudes should be more suited and is chosen in this chapter.

In our case the resonances ν_n are not just real numbers. Two additional effects are contributing to an imaginary part. The first is the broadening due to the tunneling to the chaotic area of the billiard and the connected absorption. The second contribution is the Ohmic loss caused by the skin effect of the electromagnetic waves in the metallic boundaries. In order to minimize the Ohmic loss a copper cavity was

chosen due to its good conductivity compared to the price (silver e.g. has only a better conductivity by 2-3%). Therefore equation (I.1) now looks like [49]

$$S_{11}(\nu,\vec{r}_1) = 1 - i\sum_n \frac{\mathrm{Re}(\lambda)\psi_n(\vec{r}_1)\psi_n^*(\vec{r}_1)}{\nu^2 - (\nu_n - \frac{i}{2}\gamma_{Wall} - \frac{i}{2}\gamma_{Abs})^2 - \frac{i}{2}\Gamma_n}. \tag{I.2}$$

The Breit-Wigner formula can be transformed to a Lorentzian line shape by using the binomial law and the assumption, that the real part of $\widetilde{\nu}_n = \nu_n - \frac{i}{2}\gamma_{Wall} - \frac{i}{2}\gamma_{Abs}$ is large compared to its imaginary part (typical ratio of the order 10^3),

$$S_{11}(\nu,\vec{r}_1) = 1 - i\sum_n \frac{\mathrm{Re}(\lambda)\psi_n(\vec{r}_1)\psi_n^*(\vec{r}_1)}{(\nu - \widetilde{\nu}_n)(\nu + \widetilde{\nu}_n) - \frac{i}{2}\Gamma_n} \tag{I.3}$$

$$\cong 1 - i\sum_n \frac{\mathrm{Re}(\lambda)\psi_n(\vec{r}_1)\psi_n^*(\vec{r}_1)}{(\nu - \widetilde{\nu}_n)\cdot 2\cdot \nu_n - \frac{i}{2}\Gamma_n} \tag{I.4}$$

$$= 1 - i\sum_n \frac{\mathrm{Re}(\lambda')\psi_n(\vec{r}_1)\psi_n^*(\vec{r}_1)}{\nu - \nu_n - \frac{i}{2}\gamma_n}; \quad \gamma_n = \gamma_{Ant} + \gamma_{Wall} + \gamma_{Abs} \quad , \tag{I.5}$$

where $\gamma_{Ant} = \Gamma_n/2\nu_n$ as well as $\lambda' = \lambda/2\nu_n$.

In all measurements the antenna is placed at the left part of the billiard near the boundary (see crosses in figure I.2 (b)). The goal is to excite all regular modes of at least one horizontal wave number. The neighborhood to the boundaries is meaningful because the wave functions of the regular modes do not have a nodal line in this region and are of the same order of magnitude. Also in order to excite modes with higher vertical mode number an antenna position near the boundary is suitable, because the wave function amplitudes do not change as fast as for an antenna position in the center.

To justify the chosen antenna positions in figure I.5 the amplitudes of the wave function at the position of the antenna are plotted. The contribution of the wave function to the width is declared in equation (I.1). As one can see the amplitude oscillates much faster for an antenna position just a few centimeter further in the middle of the cavity (black curve).

In textbooks for electrodynamics (compare e.g. chapter 8.8 in [47], an application in [3]) it is shown that the skin effect (γ_{Wall}) is leading to Lorentzian line shapes, where the width depends on the frequency, the type of the mode (TM or TE modes) and

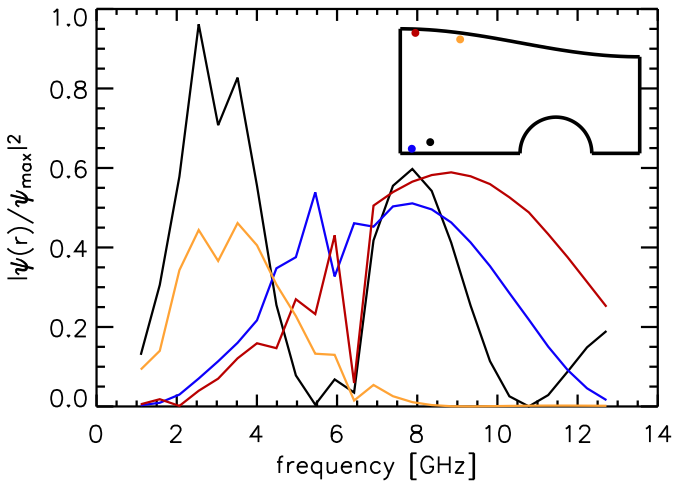

Figure I.5.: Modulus square of amplitude of wave function for different places in the cavity. The curve of each color corresponds to the antenna position in the inset of the same color. With respect to a coordinate system on the lower left corner of the billiard, the antenna positions are: position 1 (28.8 mm,11.4 mm) - blue, position 2 (37.8 mm,299.4 mm) - red, position 3 (150 mm,283.3 mm) - yellow, position 4 (84 mm,27.9 mm) - black.

the value of the derivative of the wave function in normal direction to the boundary of the billiard. The formulas are available for rectangular cavities with a justifiable effort, but not for numerically calculated wave functions. A non perfect closing of the billiard due to the finite number of screws, and the resulting not well defined contact between side walls and top respectively bottom plate leads to deviations from the theory. Another aspect is the surface corrosion. This effect might just lead to deviations in the order of some percents (typically the skin depth of copper is $\sim 1\,\mu$m, the width of copper oxide is ~ 5 nm [51]). To identify the Ohmic losses in the analysis of the experimental results I took the overall frequency dependence of the resonance width

$$\gamma_{Wall}(\nu) \sim \sqrt{\nu} \tag{I.6}$$

into consideration. In order to determine the proportionality constant various measurements were performed with different antennas and at different antenna posi-

tions, to get rid of the effect of the antenna coupling. The billiard was closed and no absorber was inside. In figure I.6 the width of all fitted resonances are plotted as crosses (width as function of resonance frequency). One can clearly see huge fluctuations of the widths of different modes at nearby frequencies. This is due to the antenna coupling and the absorption of the side walls. The absorption induced by the top and bottom plate should not fluctuate and could be understood as an overall offset. This offset is taken into account by the square-root function plotted in red.

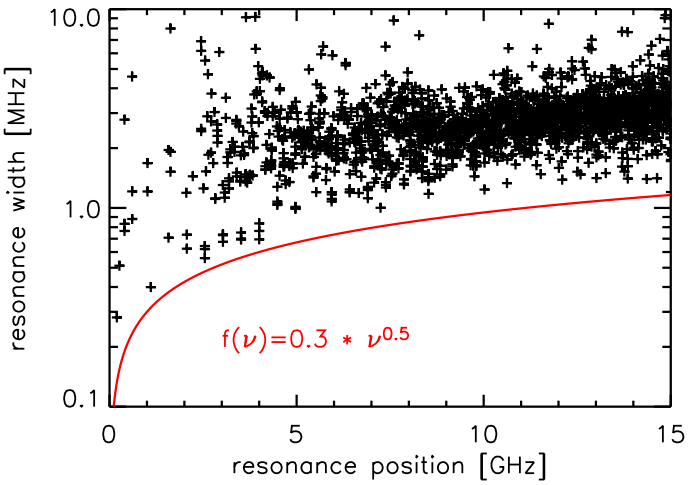

Figure I.6.: Width of resonances as function of resonance positions (black crosses). Different antennas at different positions were taken to eliminate γ_{Ant} and no absorber was placed in the cavity to cancel γ_{Abs}. As solid red line, the square root dependence of width as function of frequency with reasonable proportional constant is plotted.

The consideration of the antenna coupling will be performed by using the direct correspondence of the width (Γ_n in equation (I.1)) and the resonance amplitude ($\mathrm{Re}(\lambda)\psi_n(\vec{r}_1)\psi_n^*(\vec{r}_1)$ also in equation (I.1)), which also holds under the assumptions from equation (I.5). But this cannot be done as easy as for the width due to the Ohmic losses. In the case of two resonances coming close in frequency, equation (I.1) does not hold. The reason is the assumption of non-overlapping resonances in the scattering theory derivation of equation (I.1) (see e.g. chapter 6.1 in [9]). The spectrum can still be described by the same Breit-Wigner like line shapes but now the relation of the amplitude ($2\mathrm{Re}(\lambda)\psi_n(\vec{r}_1)\psi_n^*(\vec{r}_1)$) and the width γ_{Ant} is more

complicated. This will be explained by the help of figure I.7.

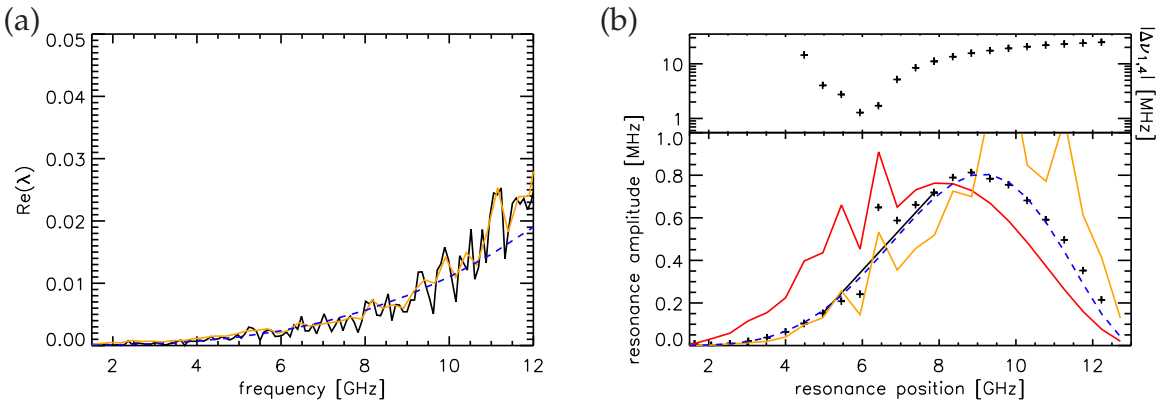

Figure I.7.: (a) The coupling to the billiard in black, in yellow extracted values for the resonance positions and in blue dashed a cubic approximation. (b) top: experimental distance of the first modes to the nearest fourth. bottom: the amplitude of the Lorentz fits for only first horizontal modes ($n = 1$; antenna position 1 (blue in figure I.2)(b)) in black pluses, in red the amplitude of the wave function (numerics, scaled). In yellow the product of the blue curve and the red curve in (a) (to mimic the amplitude as $2\mathrm{Re}(\lambda)\psi_n(\vec{r}_1)\psi_n^*(\vec{r}_1)$; no scaling factor). The blue dashed line is an approximation for the amplitude of the form of $\sim \nu^3 \sin^2(d\nu)$ as one would expect it from the dependencies in (a) and (b), whereas the black solid line corresponds to a linear approximation for the values with nearby resonance.

In figure I.7 (a) the coupling as a function of the frequency is plotted. The coupling can be extracted by $\frac{1-\langle S_{11}\rangle}{1+\langle S_{11}\rangle}$ ([11, 50], see also chapter II). The average is taken over different systems of the same size. I placed the movable half circle on all plane sidewalls of the billiard at different positions and measured at different antenna positions. The cavity was closed and no absorber was placed inside. After averaging over approximately twenty systems and frequency windows of 100 MHz the black curve in figure I.7 (a) arises. The slow increase of the coupling can be explained by the short antenna ($l \sim 0.3\,\mathrm{cm}$) in comparison to the wavelength of the microwave signal ($\sim 3\,\mathrm{cm}$ at 10 GHz, so $l < \lambda/2$) and the isolated sharp resonances. Additionally a cubic function is plotted (yellow dashed line) to mimic the frequency dependence in this range.

In figure I.7 (b) the modulus of the measured resonance amplitude is plotted against the position of the mode in black pluses. To make the diagram meaningful, only modes with the wave number 1 in horizontal direction are considered ($n = 1$).

To explain the dependence, also the numerical values for the modulus squared amplitude of the wave function at the position of the antenna (blue point in figure I.5 (b)) are plotted in red. The red curve in figure I.7 (b) was multiplied with the cubic behavior of (a) and the yellow curve arises.

To consider γ_{Ant} in the evaluation of the experimental data, there are three possibilities. The first possibility is to directly subtract the measured amplitudes from the experimental widths. This is the easiest way but not the best due to the critical extraction of the antenna width for two nearby resonances. The next possibility is to lay a straight line (black line in figure I.7 (b)) between the amplitudes you trust because of the sufficient distance to the corresponding fourth mode (compared to the width). This avoids the non monotonic behavior in the case of resonance-assisted tunneling (therefore on top of I.7 (b) the distance of the first mode to the nearest fourth mode is plotted). The last possibility is motivated by the qualitative agreement of the yellow curve in figure I.7 (b). One can assume that the amplitude as a function of the frequency is given by $\sim \nu^3 \sin^2(d\nu)$. The squared sine is extracted from the similarity to the red curve and in analogy to wave functions of rectangular cavities. The cubic function is chosen because it fits best to the coupling. Without any scaling parameter one can adapt this dependence to the experimental data and gets the blue dashed line. One has to mention that the last procedure is not automatically the most accurate. It is only an attempt to mimic the functional dependence between 5 and 8 GHz. Especially for higher frequencies there might be deviations due to the missing consideration of the real wave functions (for higher frequencies the wave function compresses in $x-$direction) at the position of the antenna. Nevertheless I decided to use this last possibility in this work. But in fact it turns out that all three possibilities show a similar quantitative agreement (see appendix C).

The main message of this section so far is that a quantitative examination of the width of modes over several GHz is not suitable. I showed that one can extract the two additional width contributions in principle. But a comparison to numerical data makes only sense by comparing the order of magnitude. Nevertheless it is obvious, that one should minimize the two contributions as much as possible (compare appendix B).

As it can be observed in figure I.4 (b) the resonances are quite sharp. In the case of resonance-assisted tunneling the modes are coming so close in frequency that

simple fit routines fail in trying to fit two resonances. In figure I.8 (a) a spectrum with very close resonances and two fits are shown. The problem is that the routines need good starting points to find the global minimum. Otherwise only one resonance will be fitted.

Due to the fact that a double line fit,

$$S_{11} \sim a\nu + b - \frac{d_1}{\nu - \nu_1} - \frac{d_2}{\nu - \nu_2} \tag{I.7}$$

has up to 6 complex parameters (complex background b with slope a, and Lorentzian amplitudes d_1, d_2 and resonance position including widths ν_1, ν_2) it is not manageable to find good starting positions by hand. There is another tool, called harmonic inversion, to extract complex resonances out of a strongly overlapping spectrum. In recent publications it has been shown that this tool is very useful to extract statistical properties like counting functions [52] of eigenfrequencies or width distributions [53]. I performed the harmonic inversion with a huge set of parameters (up to 1000 parameter sets per fit). For each parameter I took the resonances out of the harmonic inversion and used them in an additional double-line Lorentz fit (see figure I.8 (a)). By comparing the deviations from the experimental

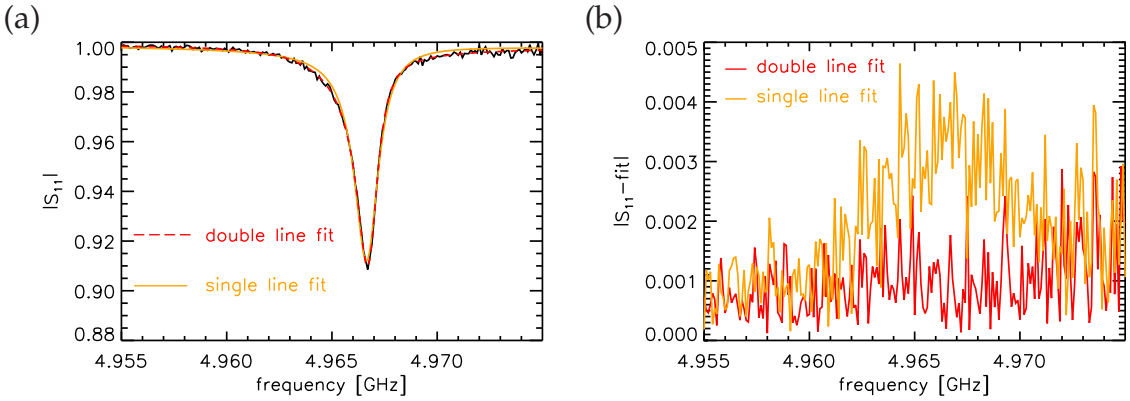

Figure I.8.: (a) Measured spectrum in black double, line fit performed with starting points from the harmonic inversion (red dashed) and single line fit performed by Lorentz fit with insufficient starting parameters. (b) Deviations of the two fits from the experimental data.

data one gets for the double line fit clearly better agreements to the experimental data (in the case of figure I.8 about 60%). In the plotted deviations of the fits one can see the not fitted second resonance (figure I.8 (b)). If the harmonic inversion

found more than two resonances an additional fit with every pair of these resonances was performed. Afterwards the χ-square tests ($\chi^2 = \sum_{n \in data}^{N} \frac{|data_n - fit_n|^2}{N}$) were compared and the fit with the best reconstruction was chosen.

I.2.2. Brief description of numerically calculated results

As the numerical calculations are performed by my colleagues in Dresden, I will just give a brief introduction to the calculation of the numerical values we will compare to the experimental data.

As it is very difficult to handle the open billiard system numerically, it was preferred to simulate the closed system. To extract tunneling rates one has to change the system. As it was shown in the introduction, the tunneling rate can be extracted from the avoided crossing between a chaotic and a regular mode (compare e.g. [31]). Therefore instead of the half circle a piston downwards was attached in the simulations. The piston begins at the starting point of the half circle and ends at the right billiard boundary. By changing the depth of the piston, only chaotic modes can be parametrically changed in such a way that they perform avoided crossings with the stable regular modes (the regular modes are not affected by the piston due to their vanishing wave function at the half circle (piston)). From the level repulsion one can calculate the tunneling rate Γ^{qm}. To transform the numerical tunneling rate Γ^{qm} [54] into a width of a microwave resonance, one has to take the dispersion relation into account. By going to the quantum mechanical case one has to consider all solutions of the Helmholtz equation. In addition to every frequency ν_n also the negative frequency $-\nu_n$ is a solution. Within a complete derivation (see e.g. section 4.1 in [55] or [56]) one gets for the quantum mechanical energy a proportionality with the square to the frequency

$$E_n^{qm} \sim \nu_n^2. \tag{I.8}$$

The quantum mechanical width corresponds to

$$\Gamma_n^{qm} \sim \nu_n \gamma_n. \tag{I.9}$$

As the numerical calculations were not performed by myself, I do not go into detail concerning the employed units and scalings. In the numerics everything is scaled to the so-called typical length which is the length of the billiard, i.e. 0.6 m. For simplicity $\frac{\hbar^2}{2m} = 1$ and thats why the energy in the numerics has the unit of $\frac{1}{m^2}$.

I.2.3. Frequency dependent tunneling rates

From figure I.4 (b) it is clear that one can identify the modes which were analyzed numerically. The numerically calculated widths are plotted in figure I.9 with red empty circles. Let us shortly discuss the numerical expectations. For the first four resonances of the first modes (figure I.9 (a) and (b)) an exponential decay of the tunneling rate as a function of the resonance position is found. At approximately 4-5 GHz the influence of the corresponding fourth mode seems to start to become relevant. This is not surprising by looking at figure I.7 (b) on the top. There at 5 GHz, the fourth mode is getting closer to the first. After having a high and sharp peak at 6.5 GHz the widths are decaying very fast by loosing nearly two orders of magnitude to the next resonance.

The experimental data is plotted in black plus symbols. In this section the results for the antenna position 1 (blue point in figure I.2) are presented. The results for the second antenna position and also the diagram to extract γ_{Ant} can be seen in the appendix C. As it was mentioned before, the effect is superposed by two other effects that broaden the resonances. It was shown in section I.2.1, that this effects can be considered in an approximative way. To visualize them in figure I.9 (a) the frequency dependence of the wall absorption (γ_{Wall}) and the antenna coupling (γ_{Ant}) are shown.

For the wall absorption (dotted in blue) the square root behavior of figure I.6 was used. The antenna coupling could be considered by the dashed yellow line which is the same as in figure I.7 (b).

The results of the corrections can be seen in figure I.9 (b) for the first mode (black crosses). A good agreement between the numerical predictions and the experimental results is found. The peak of the enhanced tunneling rate due to resonance-assisted tunneling might be shifted a little bit to lower frequencies. This is due to experimental imperfections, mainly coming from the uncertainty of the half circle

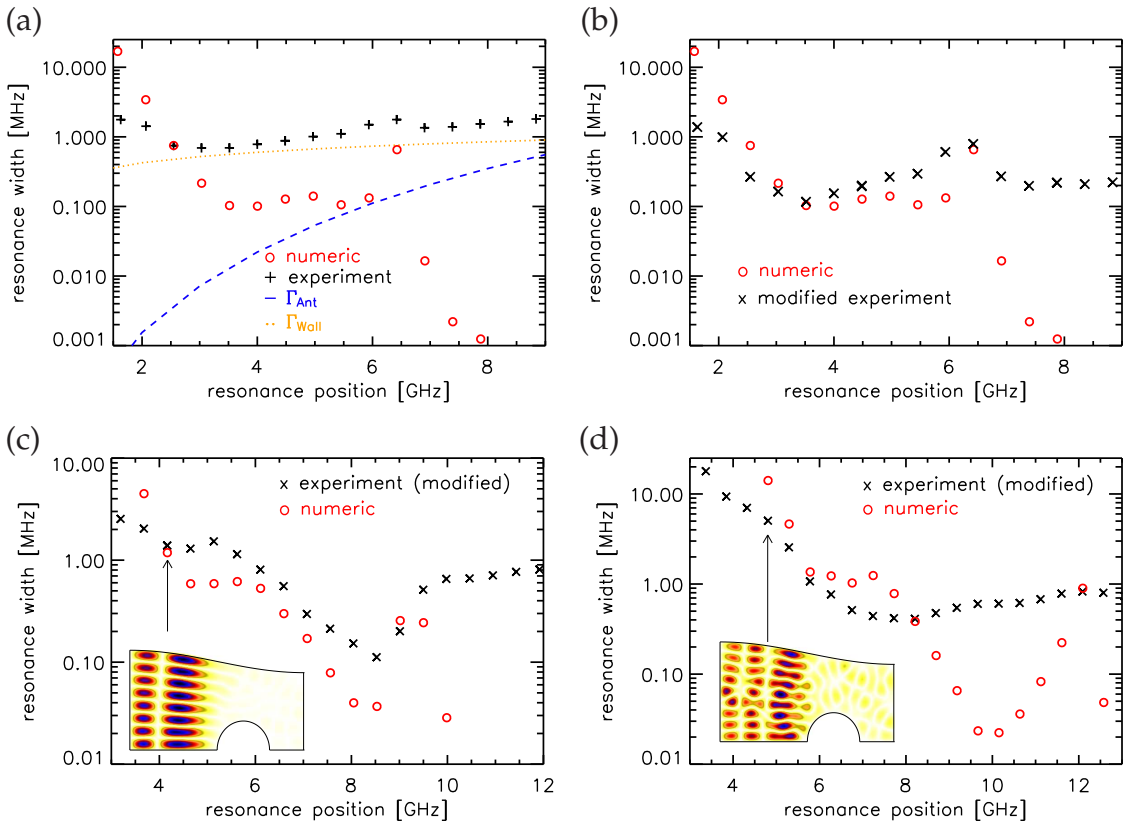

Figure I.9.: Experimental and numeric resonance width (in the case of numerics calculated out of tunneling rates) as function of the resonance position. In (a) pure data with contributions of partial widths (blue dashed and yellow dotted line). In (b) (first), (c) (second) and (d) (third) horizontal mode series with modified experimental data.

position. Numerically it was tested that for deviations of the order of the position uncertainty of the half circle a shift of the order of 1 MHz is possible. We will see in section I.2.4 that even this shift can change the situation of the tunneling slightly. As it was mentioned before in appendix C the results for the other two modification possibilities are shown.

In the case of second (figure I.9 (c)) or third (figure I.9 (d)) horizontal modes it was not possible to find such a good quantitative agreement. Qualitatively the exponential decay of the tunneling rate can be seen. The resonance-assisted tunneling is not observable any more. The rapid increase around 9 GHz in figure I.9 (c) might be an indicator for resonance-assisted tunneling. After 9.5 GHz the increase becomes lower, so in between these two slopes there could be a peak-like structure on a smoother background. But because of the missing decrease of the

widths afterwards this cannot be taken as an example for resonance-assisted tunneling. At least for the third horizontal modes the increase for the tunneling rate at the numerically predicted frequency position is not observable any longer. In both cases the underground structure of the width does not allow an observation of the enhancing effect. This problem can be explained by the complex correction procedure. The modification was performed for second and third modes like for the first. In the case of the second mode the resonance-assisted tunneling takes place at the maximum of the amplitude dependence, so no suitable approximation for this dependence can be found (compare figure C.3 in appendix C). In case of the third mode the overall exponential decay can be found as predicted but for higher frequencies the absorption correction might fail. So this nearly constant width distribution is too high to extract the enhanced tunneling effect. Even for the first modes one can see that for resonances above 8 GHz the widths are staying constant. In fact the parameters were chosen in a reasonable way but there were too many free scaling parameters to trust them overall. E.g. a small error in the square-root behavior of the wall absorption is leading to a large effect for higher frequencies. For all three series of modes a deviation for the exponential decay is found. Especially for lower frequencies the resonances should be much broader. This deviation can be explained by the non perfect absorber. The absorber quality is frequency depending and as I have shown in the beginning it starts working around 1.5 GHz. Nevertheless the absorber is not perfect and so a lower resonance width is possible. In addition the wall absorption is also mode depending (compare [47] for rectangular modes), which cannot be taken into account.

After finding this good agreement with the numerical predictions for the first modes one has to admit that the deviations for the second and third modes allow not yet a clear proof of resonance-assisted tunneling. There are several parameters with uncertainties in the correction process. The overall problem is that the correction terms depend too much on the features of every single mode.

The solution is to focus on only one resonance and try to eliminate the cause of the resonance-assisted tunneling.

I.2.4. Parametric proof of resonance-assisted tunneling

In the previous section we discussed the results of mode dependent tunneling rates. As mentioned at the end it is necessary to vary our system such that the resonance-assisted tunneling effect is eliminated. Remembering the trick to simplify the structure of the phase space in section I.2.1, one finds a relatively easy way to manage that. By including a half circle on the lower boundary one introduces a well defined border between the two phase space regions. By shifting the half circle to the left boundary one can vary the outer border of the island. The quantum mechanical states living on the outer part of the islands are influenced most. As one can see in figure I.2 the period three orbits are comparatively close to the boundary. They are affected more than the states in the inner part (the 1^{st}, 2^{nd} and 3^{rd} modes). This can be also understood by the approximation of the regular modes as rectangular wave functions. If one thinks about a hard wall instead of the beginning of the half circle shifting to the left, it is obvious that wave functions of higher horizontal wave numbers are affected more than those with lower ones. For both wave functions it might lead to a larger frequency because of the smaller wavelength in the direction to the half circle/hard wall.

To verify resonance-assisted tunneling the peak in the widths of the first mode in figure I.9 (b) (at approx. 6.4 GHz) was analyzed. By shifting the half circle in units of 0.6 mm to the left wall it was tried to eliminate the resonance-assisted tunneling effect. The presented measurements were performed at antenna position 2 (red point in figure I.2 (b)). There were also measurements performed at antenna position 1. But for these measurements a slightly different dipole antenna with a higher coupling was used. The results are presented in appendix B.

In figure I.10 (a) - (d) one can see the behavior of the two resonances as a function of the half circle positions (in the lower left corner a sketch of the positions is plotted). One can clearly see that one resonance is nearly immobile and the other resonance is shifted to higher frequencies as predicted. One should now take a closer look at the behavior of the resonances as a function of the shift of the half circle.

In figure I.11 the dependence on the half circle position is plotted. The first important fact is that the resonances get very close in the real parts. The distance is only one order of magnitude higher than the frequency resolution of the measurement device and of the order of the width of the resonance. At 0.5 in dimensionless units

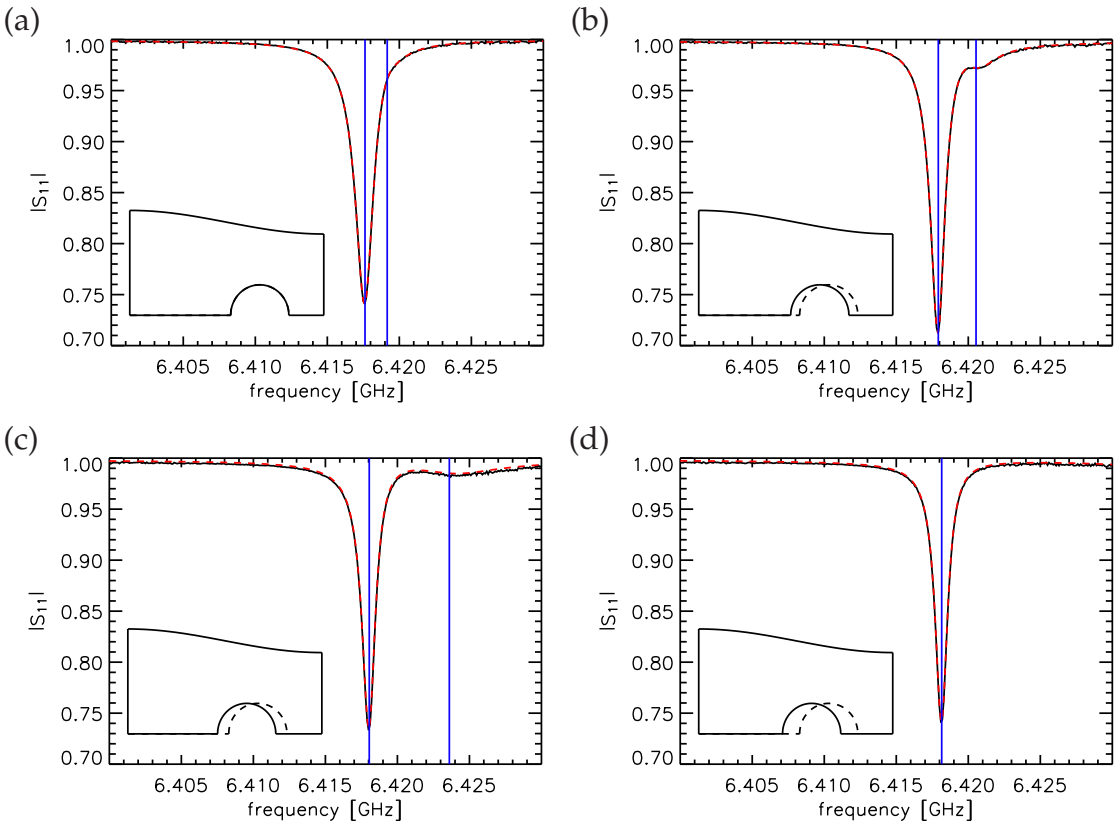

Figure I.10.: Spectra including double Lorentzian fits for 4 different half circle positions. Black curves are data, red dashed lines fits and blue solid lines fitted positions of the resonances.

the setup is at its original condition (see figure I.2 (b)). If one shifts the half circle in the direction of the left wall, that means going to the left in the diagram, the fourth mode is shifted to a higher frequency, whereas the first mode is stable. The fourth, which is living in the phase space near the boundary to the chaotic sea, is also affected in the width. For higher perturbations (the half circle is coming closer to the left wall) the width is increasing. This seems to be an obvious relation, but we will see later that the dependence of the width on the tunneling enhancing mode is not trivial. The most important observation is the clear decrease of the width of the first mode. While the fourth mode is getting away from the first in real part, the first mode is losing width. Thinking in the other direction that means, if the two modes are coming close in frequency (position) the width of the observed first mode is becoming larger. Because of the identification of the width in our setup with the tunneling rate in the corresponding quantum mechanical billiard, this is the proof of resonance-assisted tunneling. The width of the first mode is decreasing

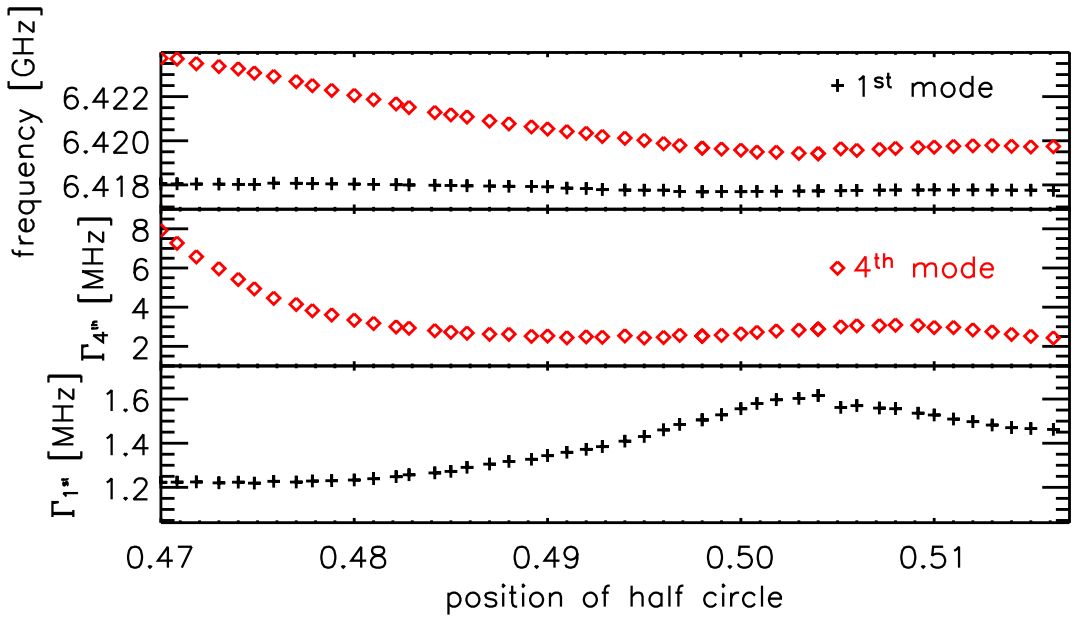

Figure I.11.: Resonance positions and widths of the two interacting modes near 6.42 GHz as a function of the half circle position. On top resonance positions of the first (black pluses) and fourth (red diamonds) mode. In the middle the width of the fourth mode and on the bottom the width of the first mode.

from 1.6 MHz to 1.2 MHz. The difference is of the order of the height of the peak in the numerical data.

To understand the effect in our setup in more detail and also to verify the found resonance-assisted tunneling quantitatively it is reasonable to look for a more significant situation, where two modes are coming close in resonance position. There is no reason why only these two modes (figure I.11) should come close in energy. One can even create resonance-assisted tunneling parametrically. Each fourth mode should be affected by the shift of the half circle more than the first modes. If we take a closer look at the first and the fourth modes around 5 GHz one can see a clear crossing of the two modes just next to the original circle position (see figure I.12).

In figure I.12 the parametrically dependence of the two modes at 4.97 GHz are visualized like in figure I.11. In the upper part one can see a clear crossing of the

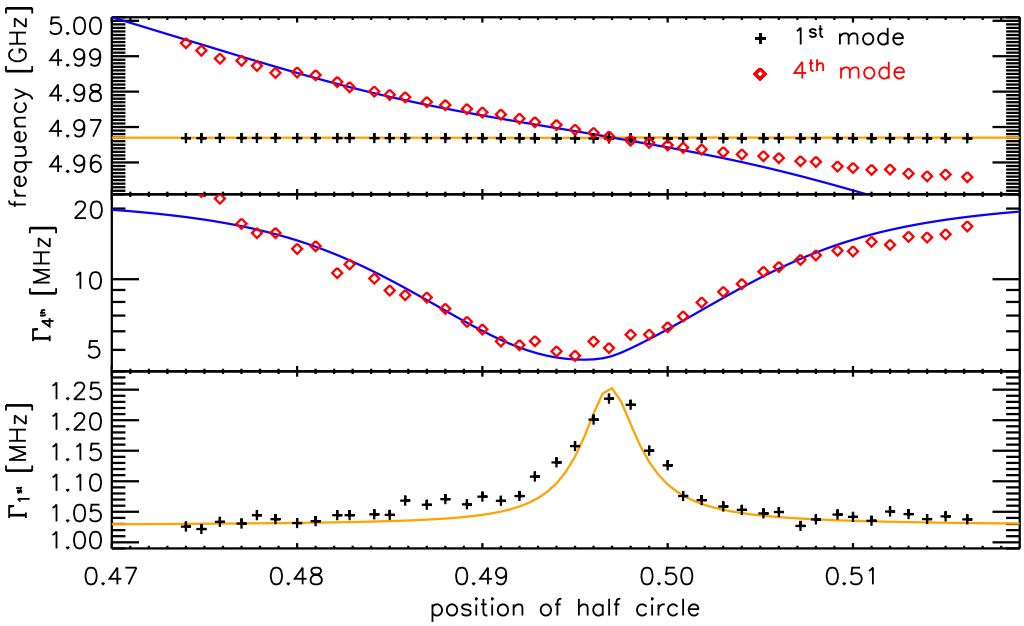

Figure I.12.: Resonance positions and widths of the two interacting modes near 4.97 GHz as a function of the half circle position. On top resonance positions of the first (black pluses) and fourth (red diamonds) mode. In the middle the width of the fourth mode and on the bottom the width of the first mode. In all three diagrams underlying numerical results from a (3×3)-matrix model are shown as lines.

two modes, at least in the order of the experimental resolution. The corresponding fourth mode is crossing the stable first mode under a higher angle than the fourth mode did in figure I.11 (note the different scales on the y-axis in the upper plots in figures I.11 and I.12). This is why the peak in the half circle position-width plot is much sharper. Also here one can see clearly the signatures of resonance-assisted tunneling. It is not the only example for such a clear crossing behavior (compare appendix D). But as mentioned in the last example, the width dependence of the fourth mode is not easily explainable. A simple explanation for this is given in the next paragraph.

To quantify the parametrical dependence of the tunneling rate an approximation of the Hamiltonian by a matrix is suitable (see e.g.[57]). As we want to understand the crossing behavior, the matrix has to contain a (2×2) sub matrix with the first and

the fourth mode on the diagonal. For the first mode the stable position is appropriate, whereas the fourth mode should show a linear drift in the position. For the widths one should take the values far away from the crossing. From calculations with (2×2)-matrices one can see that only if the off diagonal matrix elements are either real or purely imaginary the modes can cross in the real part (resonance position). As it is known from semiclassics [41, 42] and also from quantum mechanical calculations [40] the two modes are coupled via a so-called $\mathcal{V}_{r:s}$ term (here $r = 3$ and $s = 1$). This is a property which can be extracted from the classical phase space [40, 58, 59]. In our case it is a real number, only depending on the horizontal mode number. As the trace of the matrix is invariant, one needs at least one additional state to create the asymmetric width dependence of the two modes. The easiest possibility is to use a (3×3)-matrix.

In scattering through an open quantum mechanical system the openness can be described by open channels. Especially in nuclear physics effective Hamiltonians have been used to simulate open systems (for a detailed description see chapter 6.1.3 in [9] or [60], typical examples [4, 61]). In the case of a billiard opened by an absorber the effective Hamiltonian is of the form

$$\mathcal{H} = \mathcal{H}_0 - iWW^\dagger, \text{ with } w_{nk} = \int \psi_n(\vec{r}) u_k^*(\vec{r}) d\vec{r}. \tag{I.10}$$

Here $\psi_n(\vec{r})$ is the wave function in the billiard, but now with modified boundary conditions due to the open channels (can be understood as an open wall, at the line where the absorber begins) and $u_k(\vec{r})$ is the wave function of the kth channel (in this case the wave function of a wave guide). For simplicity the absorber would be represented by the number of wave channels of width $\lambda/2$ covering the line the absorber starts (here approximately 18 cm in top of the half circle).

The principle ansatz was e.g. used to calculate width distributions of the eigenvalues of $\mathcal{H}$, where interesting effects like resonance trapping [62] appears. Resonance trapping means in simple words that in case of strong coupling to open channels actually not all resonances are becoming broader. Only a few resonances are taking so to say the main part of the width and the rest is becoming sharper. This is similar to our situation. Due to the invariance of the trace of our (3×3)-matrix the third mode has to become broader. This similarity was the motivation of the application of the $WW^\dagger$ ansatz.

Since the third mode represents the chaotic sea it should be really broad. The coupling to the regular modes is, according to equation (I.10), proportional to the overlap of the regular modes and the channels. In our case the channels are the absorber, so the coupling should be of the order of the direct tunneling rate of the modes. This is leading to nearly no coupling of the first mode to the chaotic mode (so $\mathcal{H}_{13} = \mathcal{H}_{31} \sim 0$). As we are measuring the poles of the Helmholtz equation one firstly has to calculate the quantum mechanical energies (E) and tunneling rates (Γ) from the resonances like in equations I.8 and I.9. Now the assumed Hamiltonian is in detail

$$\mathcal{H} = \begin{pmatrix} E_1 - i\frac{\Gamma_{nat,1}}{2} & \mathcal{V}_{3:1} & 0 \\ \mathcal{V}_{3:1} & E_4(d) - i\frac{\Gamma_{nat,4}}{2} & -i\frac{\Gamma_{dir,4}}{2} \\ 0 & -i\frac{\Gamma_{dir,4}}{2} & E_{chaos}(d) - i\frac{\Gamma_{cont}}{2} \end{pmatrix}. \tag{I.11}$$

To verify the numerical found $\mathcal{V}_{3:1}$, the values of $\Gamma_{dir,4}$, $E_{chaos}(d)$ (with offset and slope) and Γ_{cont} were used as free fitting parameters. The values $E_1 = 10833\frac{1}{m^2}$, $\Gamma_{nat_1} = 2.4\frac{1}{m^2}$ and $\Gamma_{nat_4} = 53\frac{1}{m^2}$ are extracted from figure I.12 and transferred to the energy axis (equations (I.8) and (I.9)). The results can be seen in figure I.12 (blue and yellow lines, the quantum mechanical energies and widths were calculated back into a frequency axis) for the two sharpest resonances. An amazing agreement with the experimental results is observed. The fitted parameters are on the energy scale $\Gamma_{dir,4} = 151\frac{1}{m^2}$, $\Gamma_{cont} = 305\frac{1}{m^2}$, what corresponds on the frequency axis to a width of about $\gamma_{cont} = 70\,\text{MHz}$. The chaotic mode crosses the first mode near the other crossing point with a slope, which is approximative the same as $E_4(d)$ but in the opposite direction. The main output is that the used $\mathcal{V}_{3:1}$ is just deviating about 10 % from the numerically calculated one (the fitted value is $\mathcal{V}_{3:1} = 2.2\frac{1}{m^2}$ in comparison to the numerically evaluated $\mathcal{V}_{3:1} = 2.0\frac{1}{m^2}$ [54]). Using the simplifying (3×3)-matrix approach for an open system one can extract the resonance-assisted tunneling rate $V_{r:s}$ sufficiently. Also if one takes the frequency dependence of $\Gamma_{dir,4}$ as given from the open system and solves just a (2×2)-matrix model, the same good agreement for $\mathcal{V}_{3:1}$ can be found (see appendix E). But what is the physical origin of this third mode, which is necessary for our model? The first surprising fact is the width of this resonance. For a chaotic nearly completely absorbed resonance one would perhaps expect a width of the order of some hundreds of MHz.

In fact, it turns out that for a non perfect absorber the widths of the affected resonances are going with $\gamma = -\Delta \ln |R|$ (appendix F). Here Δ is the mean level spacing of the whole system and R is the reflection coefficient for the amplitudes. Due to the logarithmic dependence of the widths and a reflection coefficient of approximatively 2-3 percent, the widths are just of the order of three to four times the mean level spacing. The Weyl law [63] for the half resonator (only the part starting from the left wall to the beginning of the half circle is considered) predicts a number of resonances of $N(\nu) \sim \frac{A \cdot \pi}{c^2} \cdot \nu^2$, which is leading to an approximate mean level spacing of $\Delta \sim \frac{c^2}{2A \cdot \pi \cdot \nu}$ which is 32 MHz at 5 GHz. So the width of the expected channel/chaotic resonance might be of the order of 125 MHz. The real origin of this resonance could not yet be found. One only can suppose where these resonances come from. One possibility is given by the fractal repeller between the half circle and the upper cosine shaped wall (for an introduction in fractal repellers see [64, 52]). A second possibility are standing waves between the left wall and the absorbers.

I.3. Conclusion

In the last chapter I presented the experimental observation of resonance-assisted tunneling.

First modes corresponding to one regular periodic orbit were analyzed. There, for one series of modes, a very good agreement to the numerical expectations was found (figure I.9 (b)). For the other two possible series of modes the agreement was not convincing (figure I.9 (c),(d)). This was caused by a complicated procedure to extract the tunneling rates from the experimental data, which obviously fails for higher frequencies. To proof the found enhancement of tunneling, the origin of the effect, i.e. the nearly degeneracy of two regular modes was destroyed by parametrically changing the system. Here a clear proof was presented (figure I.11). To extract the coupling parameter between two regular modes a situation was presented where a clear crossing appears (figure I.12). In this case a good agreement with the numerically predicted value was found. Additionally another aspect concerning the width of the second mode was found. This could be explained by an extended matrix model (equation (I.11)) in the context of resonance trapping. As discussed in the last section the question of the origin of the third mode remains open. Nevertheless, it was shown that this does not affect the quantitative and qualitative agreement of the resonance-assisted tunneling effect. As only for a nearly integrable system the coupling between two regular modes was measured before [8], this work is the first experimental proof of resonance-assisted tunneling for a system with mixed phase space.

II. Channel correlation in transport through chaotic wave mechanical systems

II.1. Motivation

In this chapter I will show experimentally and numerically determined correlation functions of the transport through a chaotic microwave cavity. In the context of quantum chaos many models are known among which random matrix theory is suited to calculate correlation functions as the past has shown [11]. That is the motivation for a short introduction into random matrix theory. Then I will show the importance of the chosen correlation function and explain why we can use microwave devices to study results from nuclear physics.
In the main part I will stepwise define the correlation function, introduce the setup[1] and show the analyzing procedure. Since the numerical results, which were compared to the experimental ones, were performed by myself I will explain their basic components. At the end, I will show the good agreement of the experimental data with the numerics. After concluding the state of the art I will show preliminary results for the understanding of imperfections of the microwave setup.

II.1.1. Random matrix theory

Random matrix theory was originally developed to describe spectral properties of heavy nuclei. One assumes that the Hamiltonians for such systems are so complex that one can model them by random matrices. That means that the matrix has randomly chosen entries, where the distribution considers the remaining symmetries like time-reversal symmetry. From random matrix results both analytical or approximative derivations as well as numerical calculations are often available. For calculating analytic results super symmetry techniques are often suitable, but also hard to understand. For a comprehensive treatment in random matrix theory [10] is suited. The main results and calculations are summarized in [65] or [9]. As it was shown in the very beginning of quantum analog microwave experiments, these devices are qualified to test random matrix theory [66]. It was expected from the conjecture of Bohigas and coworkers [67] that random matrix theory might be applicable to all chaotic systems. Besides nearest neighbor distance distributions [66], spectral auto- and cross-correlation functions [11] are just one example for the

[1] All the experiments for the channel correlations were performed in Nice, France. At this place, I want to thank Prof. Dr. U. Kuhl and Prof. Dr. F. Mortessagne for the opportunity to perform the experiments.

test of random matrix theory approaches with microwave setups. Also open microwave systems were described by random matrices e.g. the fidelity decay [68].

II.1.2. From Ericson to conductance fluctuations

In the early sixties of the last century, just at the time when random matrix theory was developed, Ericson described spectra of strongly overlapping resonances in nuclei [69, 70, 71]. In the regime where the life time of states in the nucleus are so short that the widths become larger than the mean level spacing, it becomes impossible to identify individual resonances. Ericson found that the auto correlation function of the cross section is proportional to a Lorentzian curve whose width is the mean width of the contributing resonances. Thus, he could estimate the mean width of the resonances without identifying one certain resonance. In this context he performed a splitting of the averaged cross section (from a channel a to a channel b) into a direct and a fluctuating part:

$$\langle \sigma_{ab}(E) \rangle_E = \sigma_{ab}^{dir} + \langle \sigma_{ab}^{fluct} \rangle. \tag{II.1}$$

Ericson fluctuations appear in a wide range of physical systems. In the literature the term is mainly used to describe transmission properties of chaotic systems with strongly overlapping resonances.

The point, on which we should focus is described in [17]: the transition from one cross section between two different channels (as Ericson described) to universal conduction properties. Introducing many channels describing an incoming wave and the same number of channels describing an outgoing wave, one can describe conductance as a sum of all cross sections between the channels corresponding to the in and outgoing waves. Celardo and coworkers used a continuum shell model, where the interplay of intrinsic dynamics and coupling to the continuum has to be taken into account. For an introduction to such techniques and assumptions see [14, 15]. The model of Celardo and coworkers is presented in [16]. In [17] it is pointed out very clearly that going strictly from the Ericson ansatz of splitting the average cross section, one gets for the variance of the conductance for perfect coupled channels a value twice as large as the correct one. The mistake is that by splitting the cross sections no correlations of the type

$$C = \overline{\langle \sigma_{ij}\sigma_{i'j'}\rangle} - \overline{\langle \sigma_{ij}\rangle\langle \sigma_{i'j'}\rangle} \tag{II.2}$$

were considered. As Ericson pointed out in 1963 [70], this is due to the assumption that direct interactions in the nucleus are independent from compound reactions. These correlations appear, if one calculates the variance of the conductivity as defined in [17]:

$$G = \sum_{i=0}^{N/2} \sum_{j=N/2+1}^{N} \sigma_{ij}. \tag{II.3}$$

The consideration of this neglected dependence is the merit of Celardo and coworkers.

II.1.3. How do microwave cavities mimic nuclei scattering?

The transition from properties of nucleus scattering can be understood by looking at the model of Celardo and coworkers in reference [16]. They model the Hamiltonian as

$$\mathcal{H} = \mathcal{H}_0 - \frac{i}{2}\mathcal{W}. \tag{II.4}$$

$\mathcal{H}_0$ is the unperturbed Hamiltonian. In the nuclear physics situation this is the many body Hamiltonian, for example described by a shell model. In the microwave setup this is the Hamiltonian describing the chaotic quantum mechanical billiard. The additional part $-\frac{i}{2}\mathcal{W}$ is giving the coupling to the continuum or so to say to the decay channels and is often of the form $-\frac{i}{2}WW^{\dagger}$. In nuclear physics this exactly corresponds to the interaction of the bound states with the continuum [4]. In microwave experiments this part is due to the coupling of the antenna channels and the absorption of the walls.

Until the shell model arises in [16] the calculations are similar to them in e.g. [9], where one considers open decay channels in an unperturbed Hamiltonian. It is thus not surprising that for overlapping resonances the same behavior of the widths arises as in [62]. In this context the effect of resonance trapping (compare

also equation (I.10) in this work, section 6.1 in [9] or [72]) was rediscovered and described in more detail but now denoted as superradiance.

A short description of scattering theory and the derivation of the scattering matrix from the perturbed Hamiltonian will be given in the appendix G.

II.2. Definition of channel correlations

In the context of quantum chaos much attention was payed to correlation functions. Nearest neighbor distance distributions, auto correlation functions, two or n-point correlation functions are just a part of the huge amount of measured, simulated and calculated correlation functions.

In our case the correlations are related to transport between different channels (see sketch in figure II.1 (a)) as function of coupling. That is why one should strictly distinguish between spectral correlations and channel correlation functions (which is how we call this correlation).

The cross section and the elements of the scattering matrix are related by [17]

$$\sigma_{ab}(\nu) = |S_{ab}(\nu)|^2 \tag{II.5}$$

We are interested in the cross section (II.5) as a function of the coupling κ and not as a function of the frequency, so one defines the transmission in the attached channel as

$$T_i = 1 - |\langle S_{ii}(\nu)\rangle|^2, \tag{II.6}$$

where $\langle \cdots \rangle$ denotes an average over different systems (same size) and suitable frequency windows. Now we introduce the coupling κ_i to the channels indirectly via

$$T_i = \frac{4\kappa_i}{(1+\kappa_i)^2}. \tag{II.7}$$

If $\langle S_{ii}(\nu)\rangle$ is real, the coupling has to be of the form

$$\kappa_i = \frac{1 - \langle S_{ii}(\nu)\rangle}{1 + \langle S_{ii}(\nu)\rangle}, \tag{II.8}$$

which can be seen by inserting κ_i into equation (II.7). But the mean scattering amplitude $\langle S_{ii}(\nu)\rangle$ is not always real. In a recent work it has been shown [50] that for

this situation the real part of equation (II.8) plays the role of coupling. Nevertheless one has to pay attention to the global phase shift due to the antennas. For the principles of how the phase calibration works, see appendix H. All these properties and relations are well known in the community of scattering through nuclei [73].

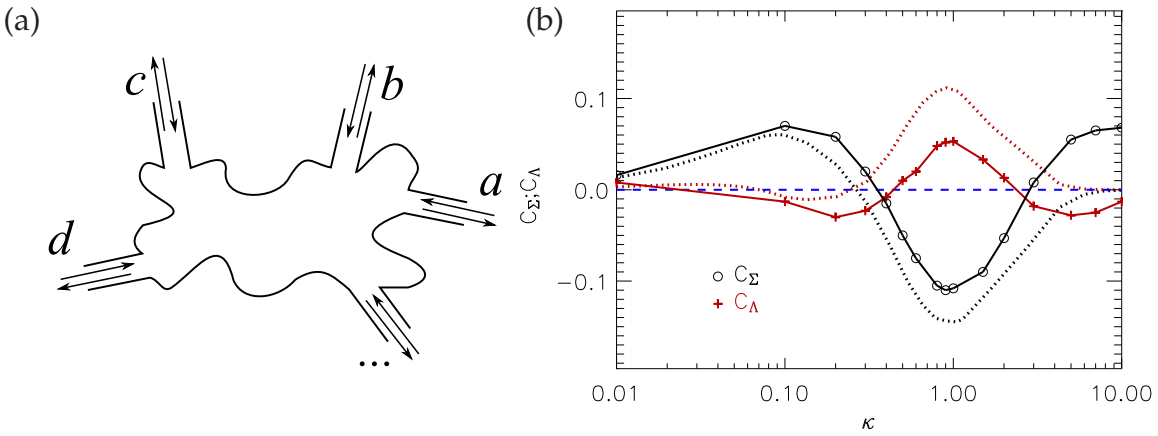

Figure II.1.: (a) Sketch of an arbitrary chaotic scattering system with more than 4 channels. (b) The two channel correlation function C_Σ in black and C_Δ in red. The combined symbols are taken out of [17], the dotted lines are from random matrix numerics, without any absorbing channels. The numerics were scaled by a factor of 30.

The channel correlation function is defined as

$$C(\kappa) = \overline{\langle \sigma_{ab}(\kappa)\sigma_{cd}(\kappa)\rangle} - \overline{\langle \sigma_{ab}(\kappa)\rangle\langle \sigma_{cd}(\kappa)\rangle}, \text{ with } a \neq b \text{ and } c \neq d. \tag{II.9}$$

The $\langle \cdots \rangle$ represents an average over energy/frequency and the $\overline{\cdots}$ over different combinations of the indices. As motivated in the introduction we distinguish between two different possibilities for II.9. The so-called C_Σ-correlation is defined as II.9 with exactly one identical index in the first and second factor. So either $a = c$ or $b = c$ ($a = d$ or $b = d$ respectively). The C_Δ-correlation forbids any equal index.

Exemplarily the channel correlations as a function of the coupling are plotted in figure II.1 (b).

Here one can see the predicted dependence of C_Σ (black empty circles) and C_Λ (red crosses) as functions of the channel coupling κ. The combined symbols are taken from [17]. The dotted lines are results from random matrix numerics as it

will be sketched in section II.3.2. In this figure no absorption is considered, which corresponds to the absence of additional channels in the model (see appendix G). One can clearly see the antiphased behavior of the two correlation functions in both predictions. On the logarithmic coupling scale there is approximately an axial symmetry around $\kappa = 1$ in both models. The dashed curves had to be scaled by a factor of 30 to match the data. The quantitative discrepancies could not be clarified until today. The main reason is the missing absorption in the continuum shell model. As absorption plays a non-negligible role in the experimental results, I will only compare the experimental data with random matrix calculations.

II.3. Experimental setup and data evaluation

II.3.1. Experimental setup - characteristics

Looking for an experimental verification of the predicted channel correlation, I performed microwave measurements using the billiard shown in figure II.2. In (a) one can see a photograph of the setup with a raised top plate, made out of aluminium. As we do not have to take care of Ohmic losses, we can chose a cheaper and lighter material as in the experiments of chapter I. In (b) one can see the shape of the billiard, which generates a classical chaotic behavior. The four circle insets with variable positions were introduced to avoid direct processes between the four antennas (a, b, c, d). For the ensemble average, different positions of the circles and rotations of the ellipse in the center (in the photograph left the brass ellipse in the middle of the top plate) were chosen. For each configuration of the circles I measured the scattering matrix for 200 different angles (in steps of 1.8°).
For these measurements a four port vector network analyzer (Agilent E5071C) was used, which allows to measure all components of the (4×4) scattering matrix ($S-$matrix) within one measurement without the need of a permanent change of cables between the different antennas. The $S-$matrix was determined in a frequency range from 2 to 18 GHz in steps of 0.2 MHz. The height of the billiard is $h = 8$ mm and so for frequencies $\nu < \frac{c}{2 \cdot h} \sim 18.7$ GHz only TM_0 modes are excited and the Helmholtz equation is fully equivalent to the two dimensional Schrödinger equation (compare appendix A). The four attached antennas were chosen to be as similar as possible. In this chapter I present data with antenna sets of 5 and 8 mm

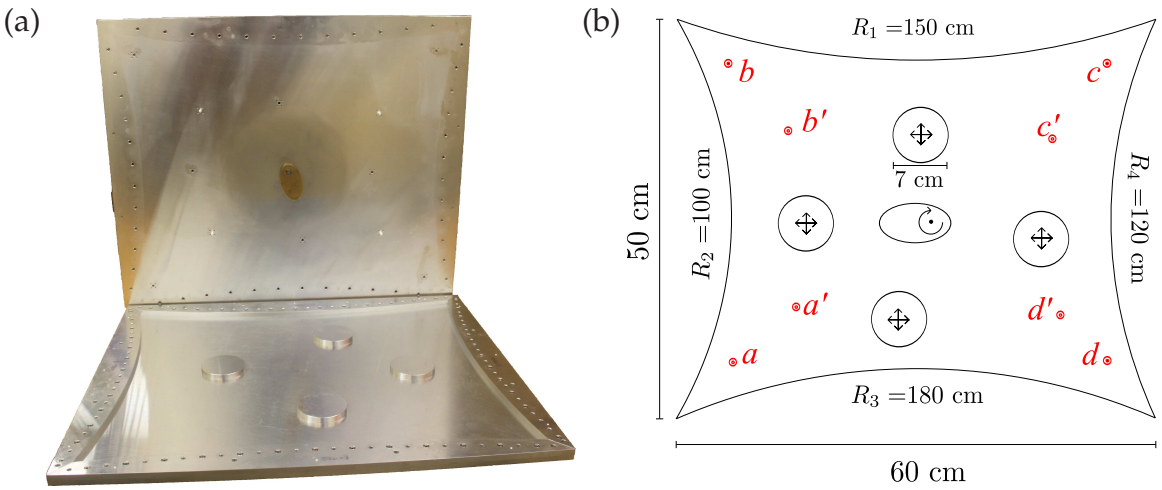

Figure II.2.: (a) A photograph of the setup and (b) sketch of the microwave resonator with a height of 8 mm.

length inside the resonator (note: 8 mm is already the height of the resonator). With shorter antennas one cannot reach couplings of the order of 1, therefore one cannot gain further information by using more antenna lengths.

Typical spectra are shown in figure II.3. On the left-hand side one can see a typical reflection spectrum in the frequency range of 4 to 5 GHz and on the right-hand side one can see the corresponding transmission spectrum. In the insets one can see the whole spectra.

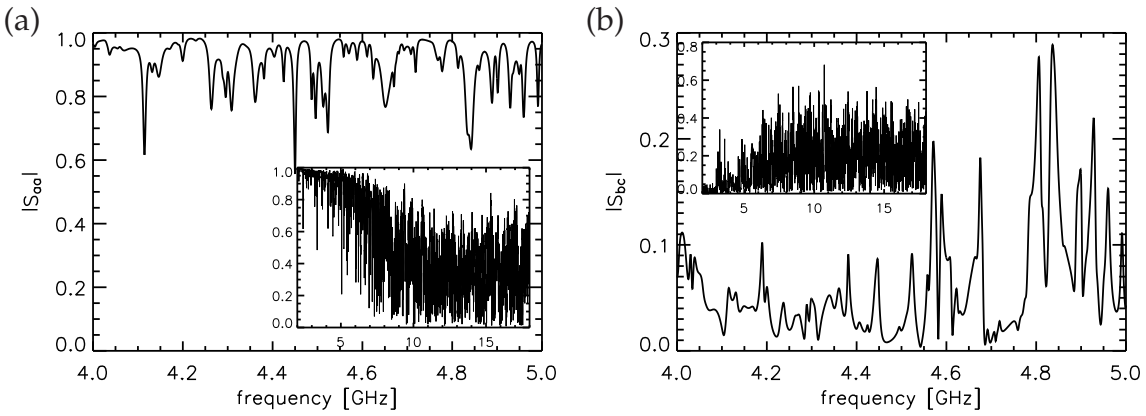

Figure II.3.: (a) Reflection and (b) transmission spectrum of a measurement of the experiment shown in figure II.2 with antennas of 5 mm length. The insets show the whole measured spectra.

In the spectrum of figure II.3 (b) it is approximately the situation where Ericson fluctuations appear. The mean level spacing (according to the Weyl formula [63])

is of the order $\Delta \sim \frac{c^2}{2A\pi\nu} \sim 15\,\mathrm{MHz}$. The widths of the resonances might be at least of the same order or even higher. Hence the requirement for Ericson fluctuations are met. Auto-correlation functions of these kind of spectra and other properties were calculated a couple of years ago, even for microwave devices [74, 75, 76]. In a former work of our group it was shown that from the spectral autocorrelation function of the reflection spectra one can calculate the absorption due to the resonator walls [11]. Precisely one would speak of the auto-correlation function ($C[\sigma_{aa}, \sigma_{aa}]$) of the cross sections σ_{aa} (for a complete definition see [11]). In that work the same expressions for the calculations of the scattering matrix and for the coupling parameters were used as in this thesis (compare section II.2 and appendix G). Using the procedure of this publication I extracted the frequency dependence of the wall absorption from the reflection spectra. In figure II.4 (a) the Fourier transform of the auto-correlation function for the frequency range of 13 to 14 GHz is plotted. In yellow a fit in accordance to the results from [11] is plotted. From the exponential decay one can extract the coupling to the wall channels, which is necessary for the numerics.

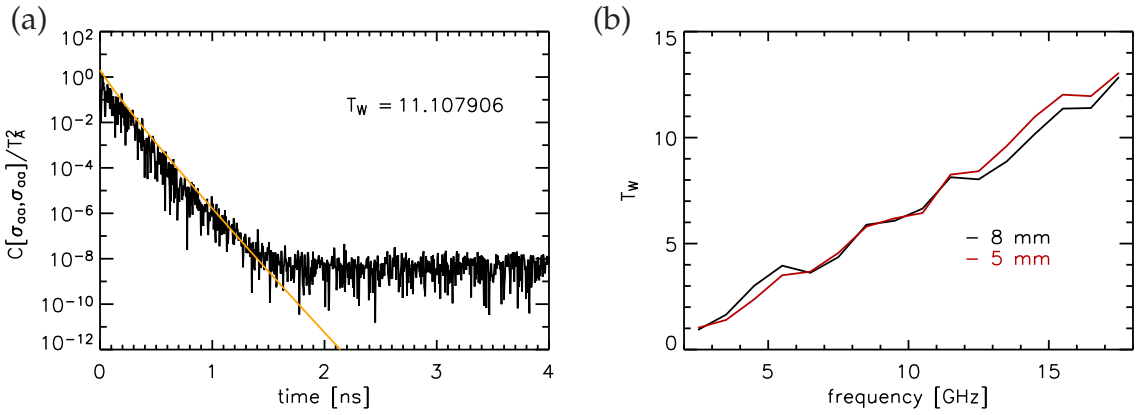

Figure II.4.: (a) Auto-correlation function of the reflection signal scaled by the transmission to the antenna. The yellow line corresponds to an exponential function to determine absorption (see [11]). (b) Wall absorption (T_W is the transmission to the wall channels) as a function of the frequency for both antenna types, averaged over all antennas and all performed measurement sets.

Figure II.4 (b) shows the dependence of wall absorption (T_W) of the used aluminium billiard extracted from the exponential decay of the auto-correlation functions like the one presented in figure II.4 (b). The data points in the right figure are averaged over 1000 measurements each (per antenna type) and for all four anten-

nas.

Before one can take a look at the channel correlation, the transformation of the frequency depending scattering matrix elements to a coupling dependence needs to be performed. One assumes that the coupling is a local parameter depending on the length of the antenna and local resonator properties like the distance to the next wall or symmetries. For example the primed antenna positions in figure II.2 (b) are expected to have other resonator properties than the ones not primed, which are quite close to the walls and on a symmetry point. By averaging over windows of 100 MHz the coupling is extracted according to equation (II.8). The results are plotted in figures II.5 (a) (5 mm long antenna) and (b) (8 mm long antenna).

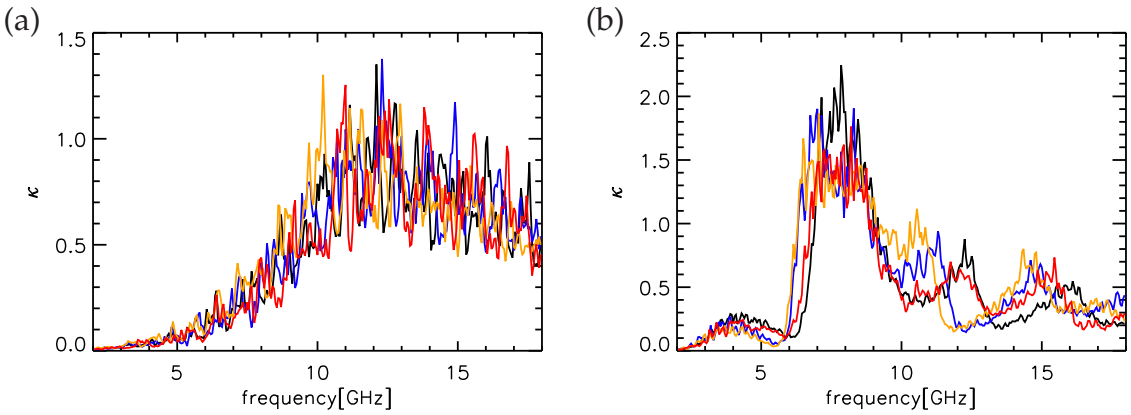

Figure II.5.: Coupling κ as a function of the mean frequency $\langle \nu \rangle_{100\,\mathrm{MHz}}$. The graphic shows the coupling for the channels a (black), b (blue), c (orange) and d (red). On the left-hand side (a) the 5 mm long antennas are shown, on the right the 8 mm antennas.

In both diagrams one can see that the coupling is changing similarly for the four antennas for each antenna set overall. Nevertheless the difference between the four antennas is comparatively strong. As we suppose that the coupling is similar for each antenna, we also average over the four antennas. With this averaged coupling dependence we have a mapping between the frequency axis and the coupling axis. Obviously the situation is easier manageable for the 5 mm long antenna as there the mapping is bijective until $\kappa = 1$.

II.3.2. Numerical calculations

In previous works of our group [77, 78] scattering matrix properties were calculated from random matrices numerically. As scattering theory predicts one can calculate the scattering matrix with the so-called Heidelberg ansatz. This is done in appendix G. The scattering matrix is calculated by

$$S(E) = \mathbb{1} - 2iW^{\dagger}\frac{1}{E - \mathcal{H}_0 + iWW^{\dagger}}W. \tag{II.10}$$

and has to be a quadratic matrix with the rank of 4 antenna channels plus a suitable number of wall channels. For all calculation I chose 50 wall channels, so S is of the size of 54×54. Later we just take the upper left (4×4) sub matrix to compare with the experiment. To make the numerics as simple as possible I chose the Hamiltonian to be a matrix of the same size. As it is shown in [9] the elements of $\mathcal{H}_0$ have to be Gaussian distributed. We do not break time-reversal symmetry. Therefore the variance for the off-diagonal elements has to be twice the variance of the non-diagonal elements (compare [9]). In the matrix W (see equation (G.24)) the coupling to the different channels has to be inserted. For both couplings we take a constant number for every channel reproducing the values of the experiment. As we are interested in the scattering matrix as a function of the coupling and not as a function of the energy we choose $E = 0$. The rest is matrix calculation, performed by standard procedures. To cancel out effects of the finite Hamiltonian size and distributions of single resonances I performed 10000 realizations for every coupling and treated them like different experimental realizations (see section II.3.1).

II.3.3. Experimental results

In the last three sections I discussed the definition of the channel coupling, the experimental properties of this system and the numerical calculations. Now it is time to take a look at the experimental data. For both antennas I measured the scattering matrix and calculated the cross sections (equation (II.5)). After rearranging σ as a function of the coupling I calculated the correlation functions (equation (II.9)). Than I averaged them in a grid of step size $\Delta\kappa = 1/50$. Afterwards I averaged over

the 200 rotation positions (steps of 1.8°) and several positions of the circle. At last I averaged over all possible antenna combinations. The results can be seen in figures II.6 (a) for the 5 mm antenna and (b) for the 8 mm antenna. Whereas the 8 mm long antennas were placed at the positions (a, b, c, d), the 5 mm long antennas had been attached at the primed positions (a', b', c', d'). The two sets of antenna positions were used for two reasons. The first is that due to a construction fault a direct classical path between the antennas was possible, we will later see the reason why one would like to avoid this. The second effect was that the coupling has an unexpected local maximum at approximately 4 GHz (see figure II.5 (b)). The reason for this might be the local structure of the nearly symmetric distance to the two walls. Therefore I used the second measurements with the shorter antennas.

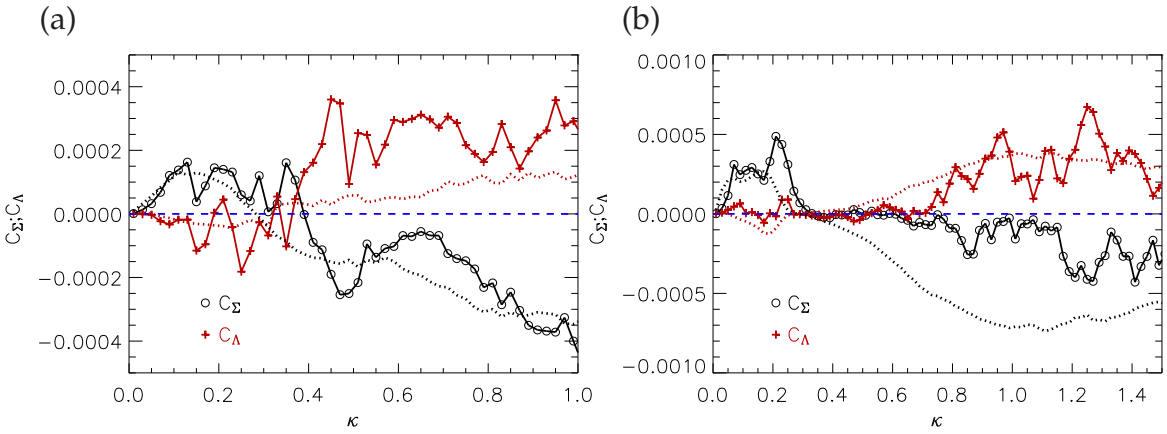

Figure II.6.: Correlation functions C_Σ (black) and C_Λ (red) as a function of the mean coupling κ for a frequency average of 100 MHz. Combined symbols are experimental date, dotted curves numerics.

To compare the results to the theory it is not sufficient to assume a constant absorption. As it was prepared in the last sections, it is possible to extract the absorption not only as a function of the frequency, but also as a function of the coupling. As we know the frequencies which contributes to one coupling, we can estimate a mean or effective absorption for each coupling value. This was considered in the numerical calculations presented as dotted lines in figure II.6.

For both antenna sets we can see a clearly antiphased behavior between the C_Δ and the C_Σ correlation. The experimental data is in good agreement with the numerical predictions. Especially at $\kappa = 1$, i.e. a perfect coupling of the channels, both correlations do not vanish.

Quantitative deviations are found which are of the form of an additional oscillating function. This can be seen between $\kappa = 0.1$ and $\kappa = 0.3$. It might be an interesting observation and the basis for a future analysis. The other discrepancy is the nearly vanishing correlation functions between $\kappa = 0.3$ and $\kappa = 0.8$ for the long antennas (figure II.6 (b)). The disappearance of the correlations is caused by the huge frequency range ($10 - 18\,\mathrm{GHz}$) of the corresponding κ values and the high absorption differences in this frequency range. E.g. at 12 GHz the coupling of the four antennas is differing between 0.15 and 0.8. Also this inconsistency of equivalent antennas within one set is a reason for the discrepancies.

The basic idea to understand the additional oscillations of figure II.6 is that remaining direct classical paths between the antennas can lead to artifacts in the frequency dependence and afterwards also in the coupling dependence. In measurements without the circles direct classical pathways should be less perturbed, at least for the primed antenna positions (compare figure II.2 (b)). Here the correlation functions have the form shown in figure II.7.

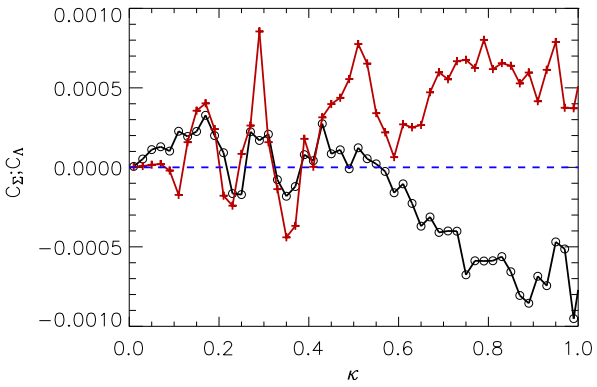

Figure II.7.: Correlation function for 5 mm antennas with direct pathways between antennas (a', b', c', d').

Up to a value of approximatively $\kappa = 0.4$ the C_Σ and the C_Δ correlation are overall similar. Oscillations on the κ-axis occur similarly to those found in figure II.6 (a) and (b) between $\kappa = 0.1$ and $\kappa = 0.3$. After $\kappa = 0.4$ both correlations become clearly different and a good agreement with the numerics is visible. Their clear oscillations are the reason why one would try to avoid direct classical paths between the antennas. If one wants to get rid of these artificial structures one could think of more complicated billiard systems where also indirect classical paths with only on

reflection are impossible.

Although the consideration of absorption within the random matrix calculation seems to work really good, one can try to construct correlation functions where the absorption is canceled by itself. The correlation function

$$C = \frac{\overline{\langle \sigma_{ab}\sigma_{cd}\rangle} - \overline{\langle \sigma_{ab}\rangle\langle \sigma_{cd}\rangle}}{\sqrt{\langle \sigma_{aa}\rangle\langle \sigma_{bb}\rangle\langle \sigma_{cc}\rangle\langle \sigma_{dd}\rangle}}, \tag{II.11}$$

might be a candidate. The idea is to get rid of the absorption dependence and in that way make experimental results comparable also with continuum shell model calculations. Results of such correlation functions are shown in figure II.3.3.

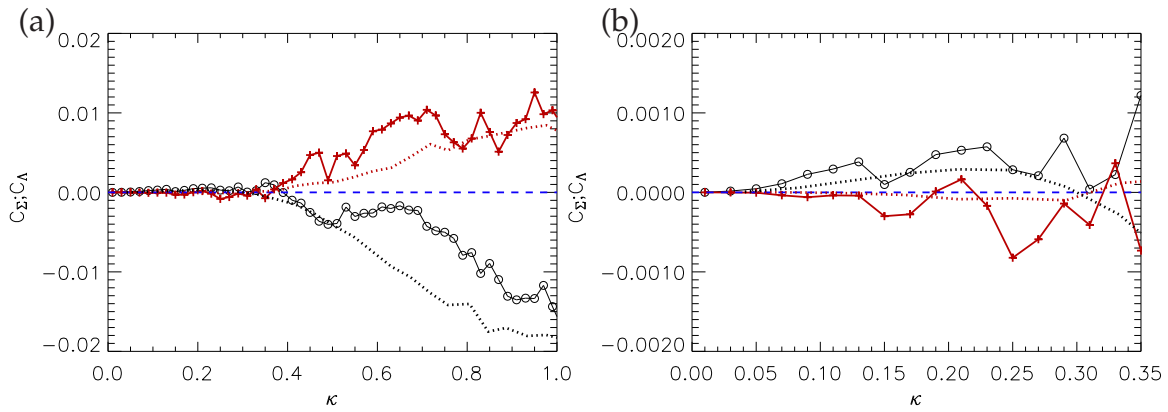

Figure II.8.: (a) The same experimental data as in II.6 (a) now with the modified correlation function (compare equation (II.11)). (b) Zoom into the κ range up to 0.35.

In the numerics absorption is present as a constant absorption. Here one can see also a good qualitative and quantitative agreement. A profound theoretical understanding of this type of correlations is necessary. Nevertheless this correlation function seems to be suited to eliminate the frequency dependence of the former analyzed ones.

II.4. Conclusion

In this chapter I presented results on channel correlation functions I defined in section II.2. It was shown that these types of correlations are very important for understanding the relation of Ericson and universal conductance fluctuations. The qualitative behavior of the two different types of analyzed channel correlations are in accordance with continuum shell model calculations.

With random matrix numerics I considered the frequency depending absorption and found a very good agreement with the experimental results. On the one hand I showed that the channel correlations do not vanish and have a typical antiphased coupling dependence. On the other hand this manifests the mistake of neglecting channel correlations in the transition from Ericson to universal conductance fluctuations.

Quantitative deviations with oscillating character could be explained with a not completely complicated channel to billiard correspondence as remaining direct classical pathways between the antennas.

For comparison to continuum shell model calculations another correlation function is introduced. As it is shown the effect of frequency depending absorption could be considered within the derivation of the correlation. A good agreement of this correlation function with the numerics was presented.

This chapter gave the first experimental proof of the existence of channel correlation in transport through chaotic wave mechanical systems. It was possible to catch the difference between the Ericson ansatz for universal conductance fluctuations and the coupled channel Hamiltonian ansatz (Heidelberg ansatz) within this presentation.

III. Realization of a microwave Floquet system

III.1. Motivation

In previous chapters only time-independent microwave systems were studied. In the correspondence to quantum mechanics this means a static Hamiltonian $\mathcal{H}$.
In the introduction it is illustrated that the investigation of time-dependent microwave systems is a promising goal. Mainly dynamical localization would be analyzed and understood by microwave experiments in a new quality.

For a realization of a microwave cavity showing, e.g. dynamical localization it is necessary that time-dependent changes care for a complete rearrangement of the spectrum. This means that the eigenvalues have to be shifted at least by the order of the mean level spacing and the variation of the frequency should also be of the same order of magnitude.
For a physical change of the system this would mean wall shifts of centimeters with frequencies of several 100 kHz, which is not realizable mechanically. An alternative approach is a variation of its electrical properties. One possibility is to induce variable capacities, e.g. varicaps, which can operate up to a few GHz. The varicaps can be either positioned inside the cavity or a varicap outside the system can be coupled via an antenna to the system. In both cases this will be a local perturbation. By using several varicaps the effect might be increased. A third possibility is to attach a system with a variable resonance frequency via an antenna which can be tuned over a broad frequency range.
In all this cases one starts from a local coupling, e.g. a point-like perturbation. To this end, a theory which had been developed previously for time-independent local perturbations [79, 80] had been extended to perturbations with time-dependent couplings [81]. In the limit of isolated resonances this theory reduces to a basic differential equation, which also describes a resonance circuit.
I will firstly investigate a setup, where a single resonance can be changed parametrically. The properties of the measured setup will be analyzed both analytically and numerically. The peculiarities of the setup can also be seen in the light of semiclassical calculations, as I will show. The single driven resonance setup will be described completely, so the next steps to the goal of establishing a microwave setup which is able to illustrate dynamical localization can be presented.

III.2. Single driven resonance - linear regime

III.2.1. Experimental setup

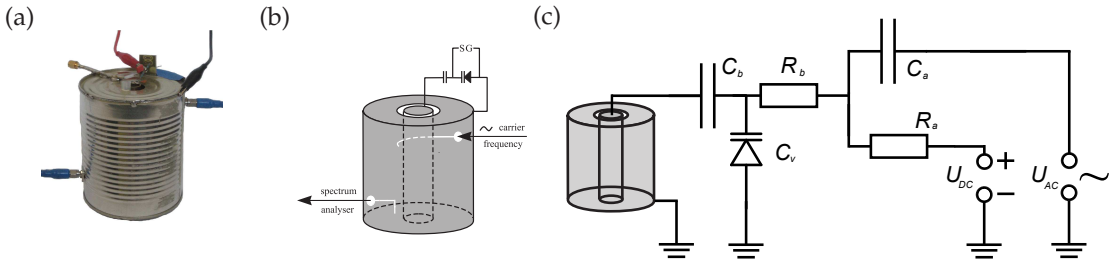

Figure III.1.: A photograph of the experimental tin (a), a sketch of the experimental setup (b), a schematic of the varicaps actuation (c). The varicap is shown as the capacitor with an arrowhead (C_v).

As discussed above the basic requirement on the setup is that it has a resonance of a typical microwave cavity ($\approx 1\,GHz$) which can be shifted electronically via a varicap. In addition one must be able to couple to the system with typical microwave devices to avoid a bad matching.

These requirements are ideally met by the tin cup shown in figure III.1 (a) in a photograph and figure III.1 (b) in a corresponding sketch.

The tin cup with a metallic core can be described as a cylindrical capacitor with a capacitance of the order of some pF and an inductance of about 45 nH [82, 83] (see appendix I). As the core is connected to the tin cup only at the bottom, one can describe it by a parallel connection of an inductor and capacitor. Its resonance frequency is of the order of some hundred MHz and a modern UHF-varicap (here infineon BB833) can change its capacitance in the pF-regime.

To excite and measure this system two antennas (white in figure III.1 (b)) were placed at the tin cup. The upper antenna forms a capacitor with the core of the tin cup, thus couples capacitively. This is in contrast to the lower antenna, which couples inductively to the magnetic field of the core, as the last part of the antenna is parallel to the core. Because of these two different couplings there is no direct communication between the two antennas.

Figure III.1 (c) shows the circuit in more detail, including the capacities $C_a = 100\,\text{nF}$, $C_b = 22\,\text{pF}$, and the resistances $R_a = R_b = 47\,\text{k}\Omega$.

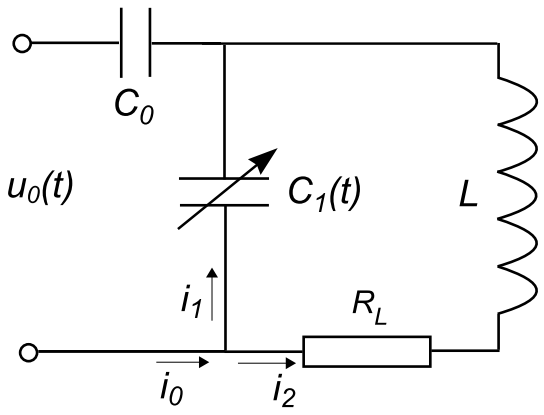

Figure III.2.: Approximate equivalent electric circuit of the whole setup is shown. The varicap (C_v in figure III.1 (c)) reduces to a changeable capacitor (C_1).

A simplified equivalent circuit diagram for the whole setup is shown in figure III.2. Due to the description of the tin cup as a parallel circuit L, C_0, C_1, and R_L depend slightly on frequency. In the following these dependencies are neglected. Feeding a signal $u_0(t)$ from a source (Anritsu 68047C) to the upper antenna one applies to the circuit an external sinusoidal AC voltage with an angular carrier frequency $\omega_c = 2\pi\nu_c$. One can apply to the terminals of the varicap either a DC voltage (U_{DC} - for the static measurement) or an AC voltage (U_{AC}) with frequency $\omega_d = 2\pi\nu_d$. For the major measurements a signal generator (HP 33120A, constant bias voltage adjustable) was used to achieve a periodic modulation of the resonance frequency. Via the lower antenna the current through the inductor is measured by the spectrum analyzer (Rohde&Schwarz FSU), which measures the intensities of the different frequency components of the applied signal.

Let us describe the electric circuit shown in the figure III.2. By i_0, i_1, i_2 we denote currents on the corresponding transmission lines. The application of Kirchhoff's first law gives

$$i_0 = i_1 + i_2. \tag{III.1}$$

The charging current at the capacitor C_0 is $i_0 = \dot{q}_0$, where q_0 is the charge of the capacitor, and $i_1 = \dot{q}_1$, where q_1 is the charge of the capacitor $C_1(t)$.

The application of Kirchhoff's second law for the two loops gives

$$L\frac{di_2}{dt} + R_L i_2 + q_0/C_0 = u_0(t), \tag{III.2}$$

$$q_1/C_1(t) + q_0/C_0 = u_0(t). \tag{III.3}$$

Integrating equation (III.1) we obtain

$$q_1 = q_0 - q_2, \quad q_2 = \int i_2(t)\, dt. \tag{III.4}$$

On the other hand, we have from equation (III.3):

$$q_1 = u_0(t)C_1(t) - q_0 C_1(t)/C_0. \tag{III.5}$$

From equation (III.4) and equation (III.5) we find

$$q_0 = \frac{C_0 C_1(t)}{C_0 + C_1(t)} u_0(t) + \frac{C_0}{C_0 + C_1(t)} q_2. \tag{III.6}$$

Substituting equation (III.6) into equation (III.2) we obtain

$$L\ddot{q}_2 + R_L\dot{q}_2 + \frac{1}{C_0 + C_1(t)} q_2 = \frac{C_0}{C_0 + C_1(t)} u_0(t). \tag{III.7}$$

Experimentally the change of the varicap capacity is comparatively small, i.e. $C_1(t) = C_1 + \delta C_1(t)$, $|\delta C_1(t)| \ll C_1$. Introducing the notation $C = C_0 + C_1$ we rewrite equation (III.7) as

$$L\ddot{q}_2 + R_L\dot{q}_2 + \frac{1}{C + \delta C_1(t)} q_2 = \frac{C_0}{C + \delta C_1(t)} u_0(t). \tag{III.8}$$

We consider $u_0(t) = u_0 e^{-i\omega_c t}$, where ω_c is the carrier frequency. We restrict ourselves to the case when the sideband structure is generated by a single driven resonance. In this case we expect that current i_2 is modulated with a carrier frequency ω_c. Therefore we write $q_2(t) = -e^{-i\omega_c t} u_0 C_0 f(t)/2$,

$$\left(\frac{\omega_c^2}{\omega_0^2} - \frac{C}{C + \delta C_1(t)} + \frac{2i\gamma\omega_c}{\omega_0^2}\right) f + \frac{2(i\omega_c - \gamma)}{\omega_0^2}\dot{f} - \frac{\ddot{f}}{\omega_0^2} = \frac{2C}{C + \delta C_1(t)}. \tag{III.9}$$

where $\gamma = R_L/2L$ and $\omega_0^2 = 1/LC$. The first two terms in the brackets can be written as

$$\frac{\omega_c^2}{\omega_0^2} - \frac{C}{C+\delta C_1(t)} = \frac{\omega_c^2-\omega_0^2}{\omega_0^2} + \frac{\delta C_1(t)}{C+\delta C_1(t)}. \tag{III.10}$$

Supposing $\delta C_1(t) \ll C$ we find

$$\left(\frac{2(\omega_c-\omega_0)}{\omega_0} + \frac{\delta C_1(t)}{C} + \frac{2i\gamma}{\omega_0}\right) f + \frac{2i}{\omega_0}\dot{f} - \frac{\ddot{f}}{\omega_0^2} = 2. \tag{III.11}$$

Let us estimate the magnitude of f. Neglecting derivatives we find $f \sim \omega_0/\Delta\omega$, where $\Delta\omega = \omega_0(\delta C_1/C_1)$ is the width of the modulation band. From the requirement that the term, containing the first derivative, is comparable to $\Delta\omega f/\omega_0$ we conclude that $\dot{f} \sim \Delta\omega f$. Hence $\ddot{f} \sim (\Delta\omega)^2 f \sim (\Delta\omega)\omega_0$ and $\ddot{f}/\omega_0^2 \sim (\Delta\omega)/\omega_0$.

Therefore the term containing the second derivative in equation (III.11) can be neglected. Finally we obtain

$$\left(i\frac{d}{dt} + \omega_c - \omega_0 + d_1(t) + i\gamma\right) f = \omega_0, \quad d_1(t) = \frac{\delta C_1(t)}{2C}\omega_0. \tag{III.12}$$

Experimentally one measures the current $i_2 = \dot{q}_2$ flowing through the coil. In the considered case one can use the approximation

$$i_2 = \frac{i}{2}\omega_c u_0 C_0 e^{-i\omega_c t} f(t). \tag{III.13}$$

Thus the spectrum measured by the spectral analyzer is given by the Fourier transform of $f(t)$.

To characterize the values of the devices in figure III.2, measurements with a time-independent $d_1(t) = d_1$ were performed. In these static measurements the amplitude f as a function of the carrier frequency ω_c has a resonant behavior

$$f = \frac{\omega_0}{\omega_c - \omega_0 + d_1 + i\gamma}. \tag{III.14}$$

The power of the transmitted signal is proportional to $|f|^2$, i.e. it is described by a Lorentzian function. The dependencies of the transmitted power on the carrier frequency for different values U of the voltage on the terminals of the varicap are shown in figure III.3 (a). The increase of the resonance height is due to the ω_0 de-

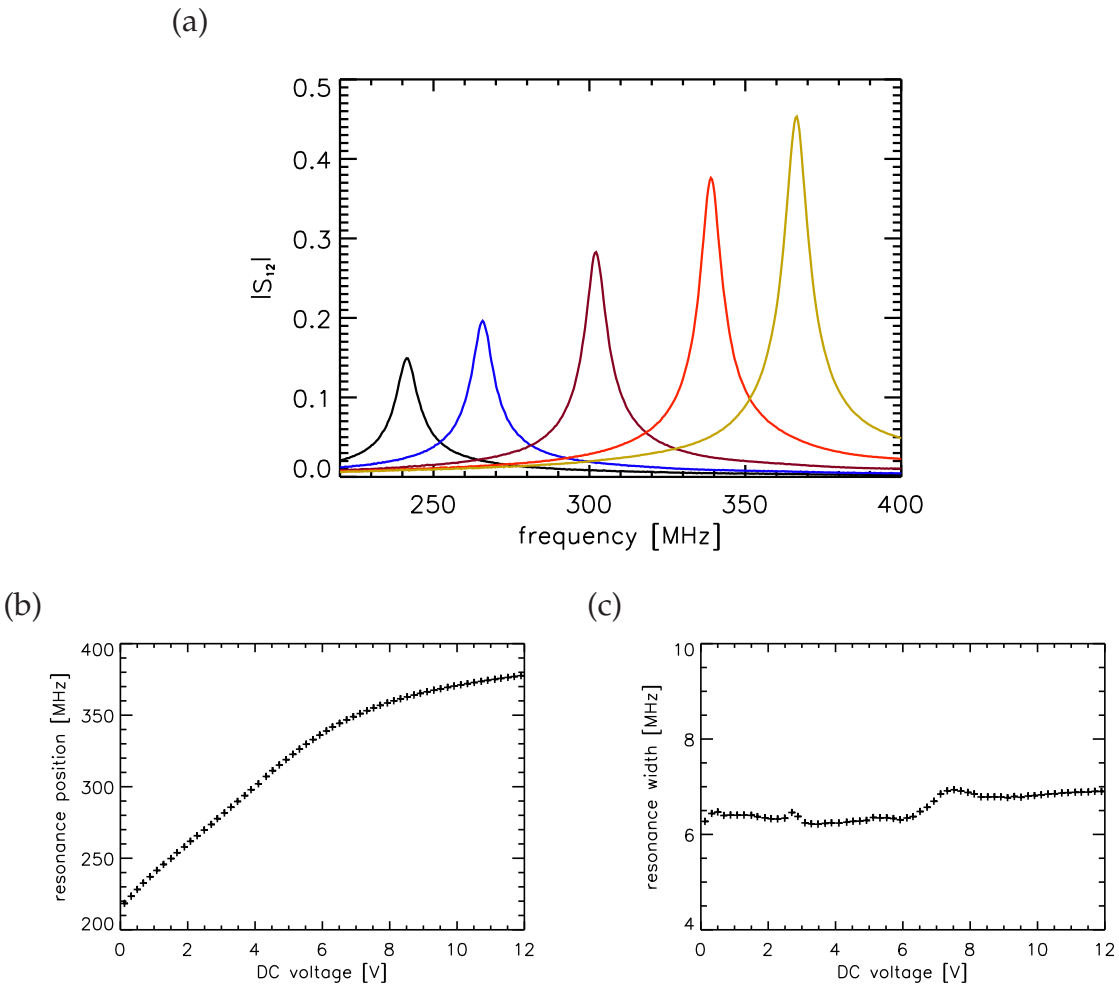

Figure III.3.: (a) Experimentally measured resonances for different DC voltages U_{DC} applied to the diode. Voltage values from the left to the right: U_{DC}= 1 V, 2.2 V, 4 V, 6 V, and 9 V. Resonance position and width as a function of the applied DC voltage are shown in (b) and (c).

pendence in the nominator in equation (III.14). The resonance frequency is given by $\omega_0 - d_1$. In figure III.3 (b) the dependence of the resonance frequency is shown, from which the dependence of $d_1 = d_{DC}(U)$ can be extracted. The width of the resonance, associated to $2\gamma = 2\gamma_{DC}(U)$, depends only weakly on the applied voltage as can be seen from figure III.3 (c).

Replacing U by $U(t)$ in the case of the dynamic measurement one obtains

$$d_1(t) = d_{AC}\big(U(t)\big), \qquad \gamma(t) = \gamma_{AC}\big(U(t)\big). \tag{III.15}$$

III.2.2. Preliminaries

Let us take a heuristic look at the introduced setup. If one applies an AC-voltage with driving frequency ω_d at the terminals of the varicap, then the properties of the circuit are changing in time periodically. The shape of the AC-signal can be chosen arbitrarily, shape restrictions are imposed only by the available signal generator.

The periodically driven circuit is excited at a given carrier frequency ω_c, which means an additional AC-voltage applied to the circuit. ω_c is assumed to be close to the resonance frequency of the circuit. Since the system is changing in time periodically, it will respond at the frequencies ω_c, $\omega_c \pm \omega_d$, $\omega_c \pm 2\omega_d$, ... leading to a sideband structure (see figure III.4). Experimentally the amplitudes of sidebands can be detected by a spectrum analyzer. The analysis of these structures is the main subject of this section.

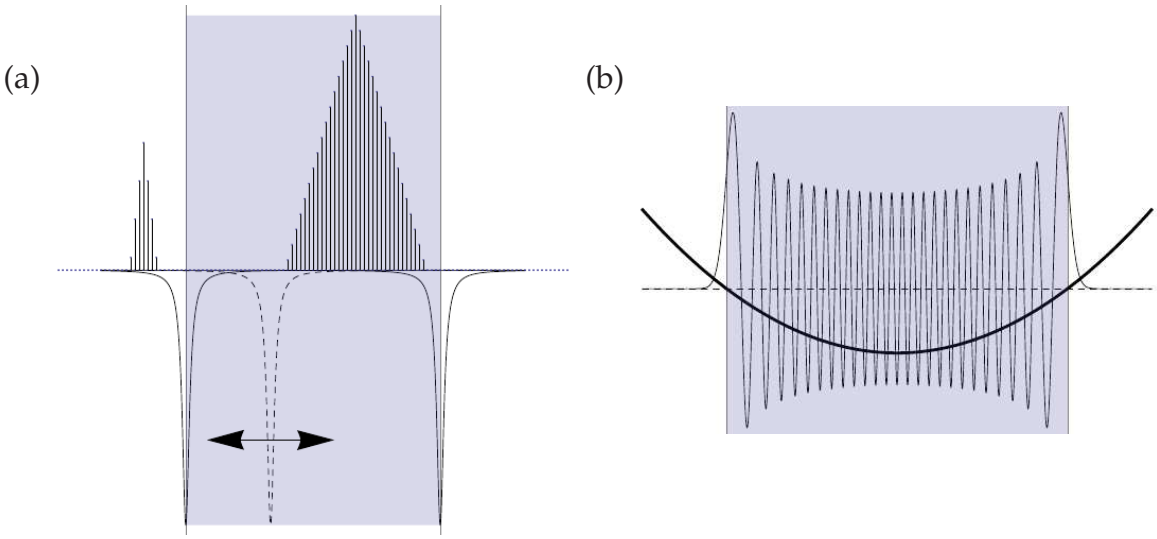

Figure III.4.: (a) Schematic illustration of the expected sideband structure. The upper part corresponds to the sideband structure of two different AC driving frequencies, one outside and the other one within the allowed region. Below the DC resonance structure for the maximal and minimal AC voltage is shown, defining the classically allowed range (shaded in blue). (b) A typical eigenfunction of the harmonic oscillator.

The circuit shown in figure III.2 assumes a linear dependence of the response on the strength of the carrier signal. However I found that a seemingly weak signal can already lead to a nonlinear dependence of the shape of sideband structures on

the applied power. To avoid complications associated with non-linear characteristics of the setup the strength of the signal was lowered to $-20\,\mathrm{dBm}$. If one now slightly changes the power ($\sim 1\,\mathrm{dBm}$), only the overall amplitude of the peaks will be altered. As we are also interested in the investigation of non-linear effects we will come to that point again in section III.3.

What do we expect in the linear regime? In figure III.4 (a) it is summarized schematically what happens when one changes the voltage on the varicap terminals in the static regime between two limiting values (solid resonances, lower half-plane) and in the dynamic regime (upper half-plane). In the static measurement of the transmitted signal one sees the peak at the resonance frequency which depends on the voltage on the terminals. Changing the voltage the resonance is shifted. The modulation band between two limiting positions of the resonance peak (filled range in figure III.4 (a)), corresponding to two limiting values of the voltage on the terminals, forms the "classically allowed" range of frequencies. Analogously the range outside this interval is called "classically forbidden". These notations will be motivated below in III.2.3.

Let us turn to the sideband structures observed in the dynamic regime. Periodically changing the voltage within the range corresponding to the "classically allowed" frequencies, and exciting the setup at some carrier frequency, a transmitted signal is generated. The characteristic Fourier spectrum of the transmitted signal is shown in figure III.4 (a), upper part. As long as the carrier frequency is taken within the classically allowed region, a large number of sidebands is observed. The situation is qualitatively different if the carrier frequency is taken in the classically forbidden region. Now there is only a small number of sidebands visible decaying rapidly with the sideband number. With the carrier frequency taken close to one of the turning points, peculiar asymmetric sideband structures are observed. All these features will be discussed in detail in section III.2.4.

In the next section I go on with a more detailed theoretical description.

III.2.3. Sidebands generated by a single driven resonance

In this section I consider sideband structures generated by a single driven resonance within the approximation of equation (III.12). The equation is inhomoge-

neous, i.e. it has a non-zero right hand side associated with a source. Let us introduce a solution

$$\psi(t) = \exp\left[i(\omega_c - \omega_0)t - \gamma t + i\int_0^t dt' d_1(t')\right] \tag{III.16}$$

of the homogeneous equation

$$\left[i\frac{d}{dt} + \omega_c - \omega_0 + d_1(t) + i\gamma\right]\psi = 0. \tag{III.17}$$

Then the periodic solution of equation (III.12) reads

$$f(t) = -i\omega_0\psi(t)\int_{-\infty}^t dt'\psi^{-1}(t'). \tag{III.18}$$

Now we can expand $f(t)$ in a Fourier series. To this end we write

$$\exp\left[i\int_0^t dt' d_1(t')\right] = \sum_{n=-\infty}^{\infty} a_n \exp(-in\Omega t), \tag{III.19}$$

with

$$a_n = \frac{\Omega}{2\pi}\int_{-T/2}^{T/2} dt \exp\left[in\Omega t + i\int_0^t dt' d_1(t')\right], \tag{III.20}$$

where $\Omega = 2\pi/T$. Then

$$f(t) = \omega_0 \sum_{n,m=-\infty}^{\infty} a_n a_m^* \frac{e^{-i(n-m)\Omega t}}{\omega_c - \omega_0 - m\Omega + i\gamma} = \sum_{n=-\infty}^{\infty} f_n e^{-in\Omega t}, \tag{III.21}$$

with

$$f_n = \omega_0 \sum_{m=-\infty}^{\infty} \frac{a_{n+m}a_m^*}{\omega_c - \omega_0 - m\Omega + i\gamma}. \tag{III.22}$$

The coefficients f_n correspond to the amplitudes of sidebands shown in figure III.4 (a). In the experiment the Fourier analysis was performed by a signal analyzer, as was mentioned above, yielding, however, only the moduli of the sideband amplitudes but not their phases.

Calculation of harmonics

To determine f_n from equation (III.22) one has to compute coefficients a_n from equation (III.20) first. Let us consider two examples, where a_n can be calculated exactly.

For the sinusoidal driving

$$d_1(t) = Z\cos(\Omega t), \tag{III.23}$$

we obtain

$$a_n = (-1)^n J_n\Big(Z/\Omega\Big), \tag{III.24}$$

where J_n is the Bessel function of the first kind. In case of rectangular driving

$$d_1(t) = \begin{cases} -Z, & \text{for } -T/2 < t < 0, \\ Z, & \text{for } 0 < t < T/2, \end{cases} \tag{III.25}$$

we find

$$a_n = \begin{cases} \dfrac{Z}{i\pi\Omega}\dfrac{1-(-1)^n e^{i\pi Z/\Omega}}{n^2-(Z/\Omega)^2}, & \text{if } \; n \neq \pm Z/\Omega, \\ 1/2, & \text{if } \; n = \pm Z/\Omega. \end{cases} \tag{III.26}$$

In figures III.5 (a) and (b) the moduli of coefficients a_n are shown for sinusoidal and rectangular driving for $Z/\Omega = 100$. A rise of amplitudes near the points $n = \pm Z/\Omega$ is found in both cases. Figure III.5 (a) shows an exponential decay of amplitudes outside of the region $-Z/\Omega < n < Z/\Omega$ (see inset), while in figure III.5 (b) the decay is algebraic (see inset). Using equation (III.22) the corresponding sideband structures have been calculated. They are shown in figure III.5 (c) and (d). In case of the sinusoidal driving an exponential decay is observed, whereas in case of the rectangular driving an algebraic decay was found. As usual, exponential and algebraic decays of sidebands correspond to an analytic and a step-wise driving respectively. One can notice a peculiar behavior of the sideband structure close to the turning points in figure III.5 (c). An intuitive argument explaining this behavior is given in the next paragraph.

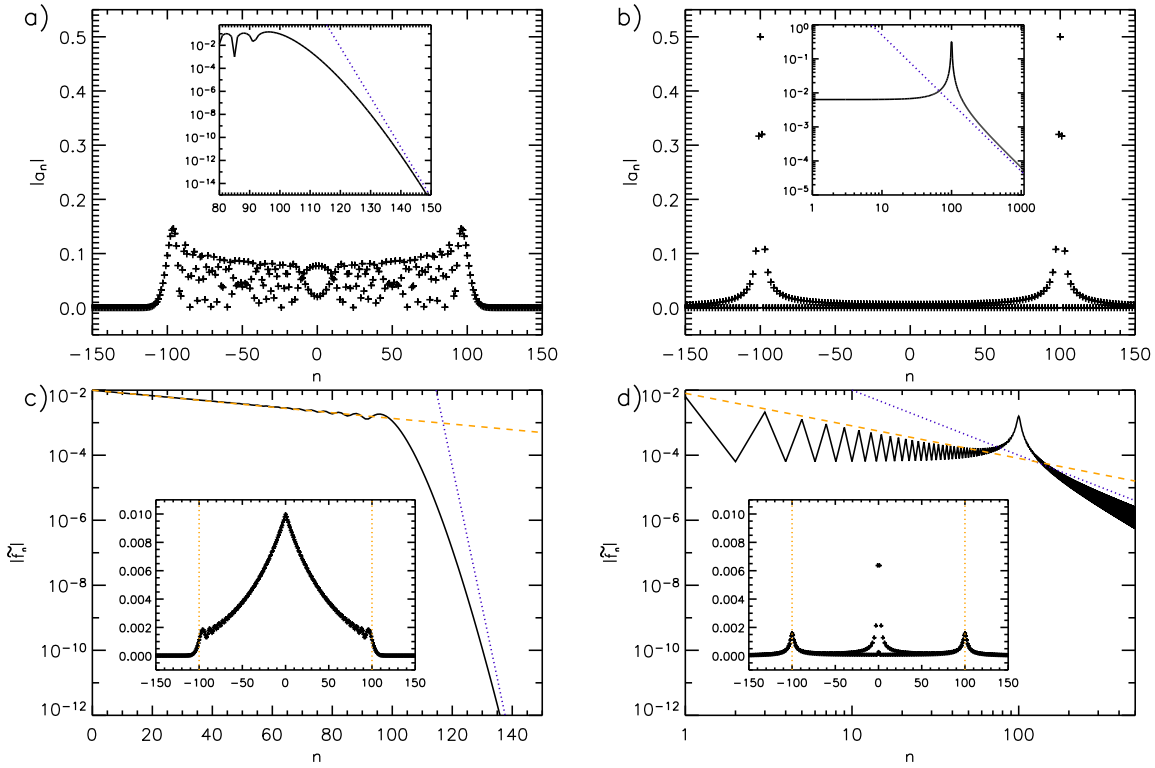

Figure III.5.: Coefficients $|a_n|$ without external excitation with $Z/\Omega = 100$ for sinusoidal (a) and rectangular (b) driving (see equation (III.24) and equation (III.26)). The inset in (a) shows a corresponding semi-logarithmic plot, where the dotted line $\propto e^{-n}$. The $(-1)^n$ in the upper equation (III.26) results in an odd-even staggering of the amplitudes a_n, for that reason the inset in (b) shows the odd n in a double-logarithmic plot, where the dotted line $\propto n^{-2}$. The resulting sideband structures f_n (equation (III.22)) are plotted for sinusoidal (c) and rectangular (d) driving. The carrier frequency was chosen to be at the center of the modulation band. The insets show the corresponding data in a linear plot. In (c) the orange dashed line corresponds to $\propto e^{-n}$ and the blue dotted line to $\propto e^{-2n\Omega/Z}$. In (d) the orange dashed line corresponds to $\propto n^{-1}$ and the blue dotted line to $\propto n^{-2}$.

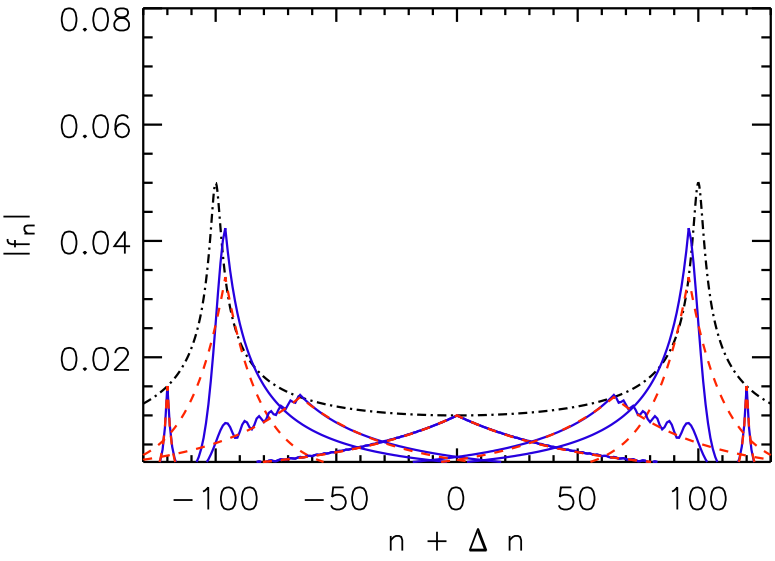

Figure III.6.: Envelops of sideband structures f_n for the sinusoidal driving with $Z/\Omega = 100$, $\gamma/\Omega = 2$ at different driving frequencies. The blue lines correspond to equation (III.22), the dashed red lines represent the approximation equation (III.28). The dashed-dotted curve is an envelope of the main peaks equation (III.29).

The features of sideband structures

In the last subsection an analytical solution of equation (III.12) is presented. However this solution is not convenient for further analysis due to the infinite sum in equation (III.22). For this reason we will simplify the solution.

Let us first neglect the time derivative in equation (III.12). Then the solution reads

$$f(t) = \frac{\omega_0}{\omega_c - \omega_0 + d_1(t) + i\gamma} \tag{III.27}$$

and

$$f_n = \frac{\Omega}{2\pi} \int_{-T/2}^{T/2} \frac{\omega_0 e^{in\Omega t} dt}{\omega_c - \omega_0 + d_1(t) + i\gamma}. \tag{III.28}$$

Approximation of equation (III.27) fails when the derivative $f'(t)$ becomes large and therefore cannot be neglected in equation (III.12). For an analytic signal this happens only in the case of a weak absorption if the carrier frequency lies within a modulation band. Then close to the time t^*, with $d_1(t^*) = \omega_0 - \omega_c$, expression

(III.27) is no longer valid. A precise behavior of the function $f(t)$ close to t^* is the origin of the peculiar behavior of sidebands close to the turning points.

Figure III.6 shows envelops of sideband structures for different carrier frequencies for the case of sinusoidal driving (equation (III.23)) and weak absorption. Sideband structures generated by equation (III.22) are compared with approximative results equation (III.28) gives. One can see that equation (III.28) generates sideband structures with a smooth profile and a width dependent on the location. Within the modulation band sideband structures are broader while outside this range they are narrower. Amplitudes of harmonics beyond the classically allowed range decay much faster than those inside.

Far from the two turning points equation (III.28) works well. In the vicinity of a turning point equation (III.22) produces oscillations on top of smooth profiles given by equation (III.28). These oscillations appear due to the localized singularities of $f(t)$ which are not reproduced by equation (III.27).

The amplitude of the main peak f_0 for the sinusoidal driving in the framework of equation (III.28) can be calculated analytically. One finds

$$f_0 = \frac{\omega_0}{\sqrt{(\omega_c - \omega_0 + i\gamma)^2 - Z^2}}. \tag{III.29}$$

In figure III.6 the envelope $f_0(\omega_c)$ is shown by the dashed-dotted line.

Semiclassical analysis of the spectrum

The direct numerical calculation of harmonics a_n for an arbitrary driving function $d_1(t)$ requires the computation of integrals of the rapidly oscillating function in equation (III.20). This leads to a hardly controllable accuracy. A proposal to avoid this problem in practice is to use an analytical approximation for a_n. The first step in the approximation is to use the stationary phase method [84, 85] to compute equation (III.20). It gives

$$a_n = \sum_i \frac{\Omega}{\sqrt{2\pi d_1'\left(t_n^{(i)}\right)}} \exp\left(in\Omega t_n^{(i)} + i\int_0^{t_n^{(i)}} d_1(t)dt + \frac{i\pi}{4}\mathrm{sgn}\left(d_1'(t_n^{(i)})\right)\right), \tag{III.30}$$

where stationary points $t = t_n^{(i)}$ are solutions of the equation

$$n\Omega + d_1\big(t_n^{(i)}\big) = 0 \tag{III.31}$$

within the interval $-T/2 < t_n^{(i)} < T/2$ and the summation in equation (III.30) should be performed over all solutions. If equation (III.31) does not have solutions, the corresponding harmonics a_n are exponentially small. In the frame of the considered approximation one can put $a_n = 0$ if equation (III.31) has no solutions and the frequency $n\Omega$ is far outside the classically allowed region.

If $t_n^{(i)}$ lies in the vicinity of a stationary point t^*, where $d_1'(t^*) = 0$, the denominator equation (III.30) becomes small and the approximation equation (III.30) fails. To overcome this problem one can expand the exponent in equation (III.20) in a Taylor series

$$\begin{aligned} in\Omega t \quad & +i\int_0^t dt' d_1(t') \simeq \\ in\Omega t^* \quad & +i\int_0^{t^*} dt' d_1(t') + i(t-t^*)\big(n\Omega + d_1(t^*)\big) + \frac{i}{6}(t-t^*)^3 d_1''(t^*) \end{aligned} \tag{III.32}$$

and perform the integration replacing the limits of integration $\pm T/2$ by $\pm\infty$. This gives

$$a_n = \frac{2^{1/3}\Omega}{(d_1''(t^*))^{1/3}} \exp\left(in\Omega t^* + i\int_0^{t^*} d_1(t)dt\right) \mathrm{Ai}\left(\frac{2^{1/3}\big(n\Omega + d_1(t^*)\big)}{\big(d_1''(t^*)\big)^{1/3}}\right), \tag{III.33}$$

where $\mathrm{Ai}(x)$ is an Airy function. The last equality is valid provided that

$$\frac{2^{1/3}\big(n\Omega + d_1(t^*)\big)}{\big(d_1''(t^*)\big)^{1/3}} \lesssim 1, \tag{III.34}$$

i.e. within the frequency range much smaller than the size of the modulation band.

The situation is very similar to the quantum-mechanical treatment of the movement of a particle in a potential well. Let us take for the sake of simplicity a harmonic oscillator potential, $V(x) = \frac{D}{2}x^2$. Its eigenfunctions (figure III.4 (b)) are

obtained as solutions of the Schrödinger equation

$$\psi_n''(x) = -\frac{2m}{\hbar^2}(E_n - V(x))\psi_n(x) \tag{III.35}$$

with $E_n = \hbar\omega(n + \frac{1}{2})$ and $\omega = \sqrt{D/m}$. The WKB approximation yields for the eigenfunctions in the classically allowed region (see e.g. section 3.2.3 of [9])

$$\psi_n(x) = \mathrm{Re}\,\frac{1}{\sqrt{2\pi|p_n(x)|}} e^{i(\int_0^x p_n(z)dz - \frac{n\pi}{2})} \tag{III.36}$$

where $p_n(x) = \sqrt{\frac{2m}{\hbar^2}(E_n - V(x))}$. Outside the classically region the eigenfunctions become exponentially small. At the classical turning points corresponding to $p_n(x) = 0$ the WKB approximation fails, but just as in equation (III.33) again the transition regime can be covered in terms of Airy functions.

This close analogy in particular of equation (III.30) and equation (III.36) was the motivation to transfer terms like "classically allowed","classically forbidden" etc. to the Floquet system.

III.2.4. Experimental results

Now we can turn to the analysis of the experimental spectra and compare them with predictions based on equation (III.12). Figure III.7 (a) shows a typical experimental sideband structure for sinusoidal driving. As expected the sidebands are equidistant with a distance corresponding to the driving frequency. The base value of -100 dBm is the noise threshold of the spectrum analyzer. The input power of the carrier wave is -20 dBm for all shown experimental results. I carefully checked that a change of the input power in this regime leads only to the same shift for all sideband structures. Figure III.7 (b) shows the frequency range covered by the modulation, i.e. the allowed region, shaded in red. For a better visualization similar plots as insets in the following figures are included. The vertical solid lines correspond to carrier frequency values ν_c selected for the plots in figure III.8 and figure III.11.

In the time-dependent driving experiments the AC-voltage is limited to the range between 1.5V and 2.5V. Within this range the position of the resonance depends

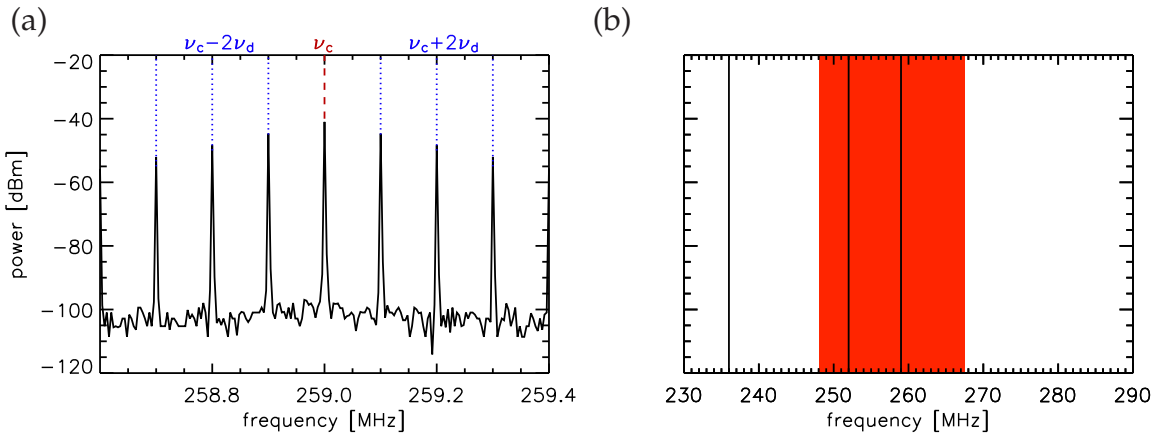

Figure III.7.: (a) Experimentally measured spectrum for sinusoidal driving with a driving frequency $\nu_d = \Omega/2\pi = 100\,\text{kHz}$ and a carrier frequency of $\nu_c = 259\,\text{MHz}$ is shown. The distance between the sidebands is exactly the driving frequency ν_d. (b) Sketch of the measured frequency range. Red shaded region corresponds to the range of eigenfrequencies covered by the modulation (extracted by *DC* measurements) and vertical black lines to several values of carrier frequency ν_c used to probe the spectrum.

linearly on the voltage and the width stays approximately constant, see figure III.3 (b) and (c). From figure III.3 (b) one can conclude that turning points lie at 248 MHz and 267.5 MHz.

I used several functional dependencies $U(t)$ to drive the varicap. In this section I will discuss cases of the sinusoidal and the rectangular driving. The theoretical model predicts a fundamental difference in the shapes of sideband structures in these two cases (see figures III.5 (c) and (d)), as it was discussed in section III.2.3.

Sinusoidal driving

In figure III.8 spectra for three different situations are shown. On the left hand side experimental results and on the right hand side numerical results are presented. For the numerics I performed a fourth order Runge-Kutta algorithm to solve equation (III.7). The parameters of the circuit were determined by the DC measurements (see section III.2.1). I decided to perform the numerical computation for two main reasons. The first is the complicated analytical procedure to obtain the amplitudes of the sidebands. The second reason is that the numerical calculation of equation

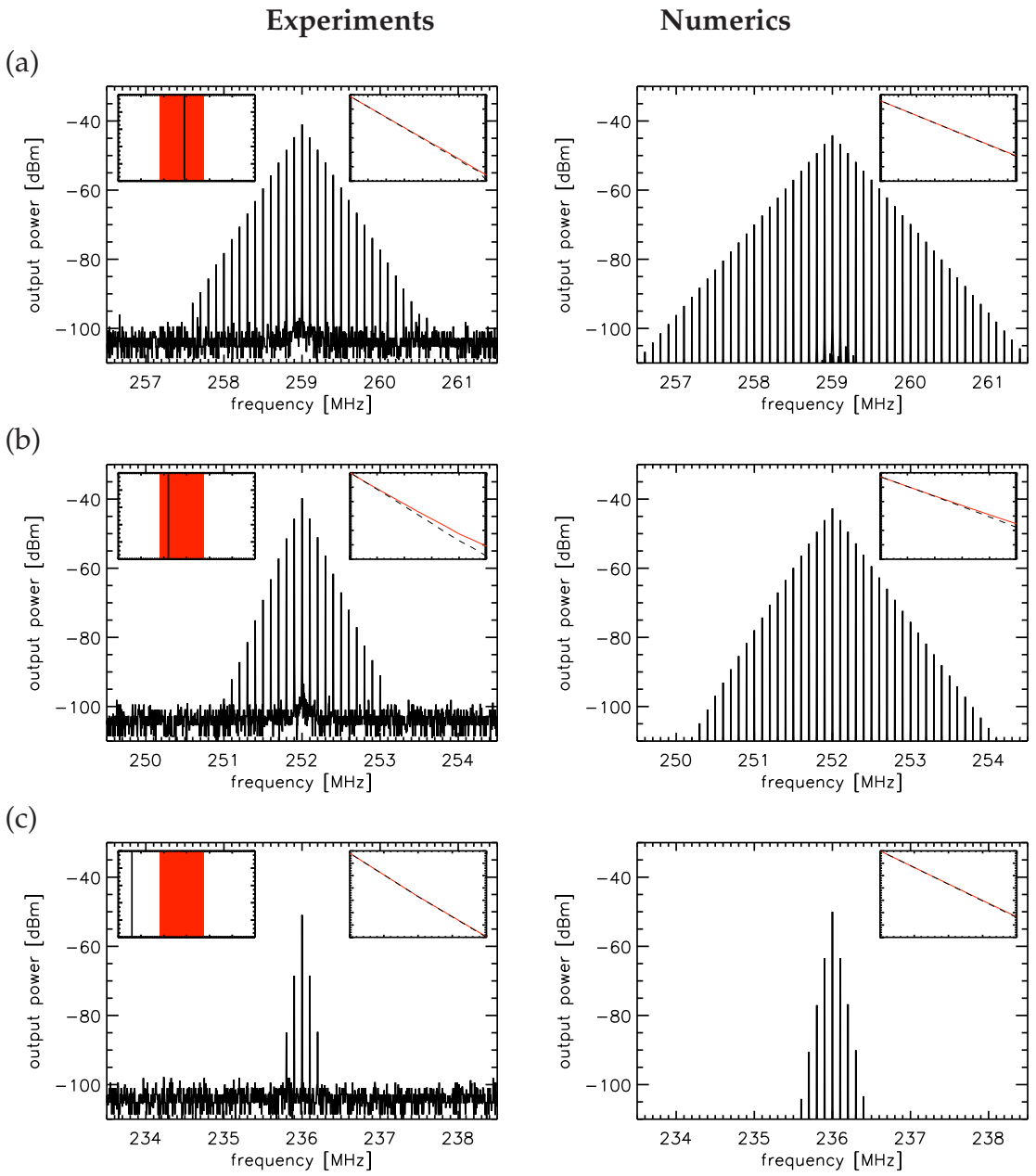

Figure III.8.: Experimental (left) and numerical (right) sideband structures observed for sinusoidal driving with ν_c= 259 MHz (a), near turning point (ν_c= 252 MHz) (b) and at ν_c= 236 MHz (c), for a driving frequency of $\nu_d = \Omega/2\pi = 100$ kHz. The left insets show the position of the driving frequency with respect to the band of the eigenfrequencies covered by the modulation. The right inset shows the envelope of the decay of the right (red solid) and left (black dashed) sidebands vs $|\nu_c - \nu_n|$ by connecting the data points.

(III.7) can test the simplification of the setup as circuit in figure III.1 (d). On the y-axis the output power is given in dBm, corresponding to a logarithmic scale. Both in the experiment and the numerics the expected exponential decay of side harmonics is clearly observed. Additionally one avoids uncertainties due to the neglects between equation (III.7) and equation (III.12).

For the spectra shown in figure III.8 (a) the carrier frequency is close to the center of the modulation band. A zoom of this spectrum has already been shown in figure III.7 (a). A broad sideband structure is found in accordance with the theoretical expectation. In figure III.8 (b) the carrier frequency is close to one of the turning points. This gives rise to a narrower asymmetric sideband structure. The asymmetry can be seen in the inset on the right. Due to the comparatively large absorption the observed asymmetry is small compared to the ones shown in figure III.6. Figure III.8 (c) corresponds to the carrier frequency outside the modulation band. Here the sideband structure is very narrow. For the sake of convenience the abscissa in figure III.8 (a)-(c) is the same.

The comparison of experimental and numerical data shows a minor quantitative discrepancy in the decay of harmonics. This discrepancy shows the drawback of the reconstruction procedure: the damping γ has been obtained from the time-independent measurement, while the sideband structures have been measured with a driven varicap. As one will see in the next paragraph the numerical sideband structures are very sensitive to a change of the damping and I decided to use the extracted value ($\sim 20\,\mathrm{MHz}$) instead of trying different γ-values systematically, until the discrepancies vanish, but no further physical knowledge is generated.

In figure III.6 an oscillating band structure close to the turning points is obtained, which is not observed in figure III.8. This is an effect of the strong damping, which is illustrated by the numerics shown in figure III.9. The damping is reduced by a factor of three from figure III.9 (a) to (d), respectively. The reduction of the damping transforms the slightly asymmetric triangle-like structure (figure III.9 (a)) to a very asymmetric one with a periodic modulation of the shape close to the turning point (figure III.9 (d)). It was not possible to resolve these oscillations experimentally due to the significant minimal damping that characterizes the setup.

In figure III.10 experimental sideband structures for five different carrier frequencies are superimposed. The solid black line is the envelope of the amplitude of the main peaks. The distance between main peaks was chosen to be $1\,\mathrm{MHz}$ for the

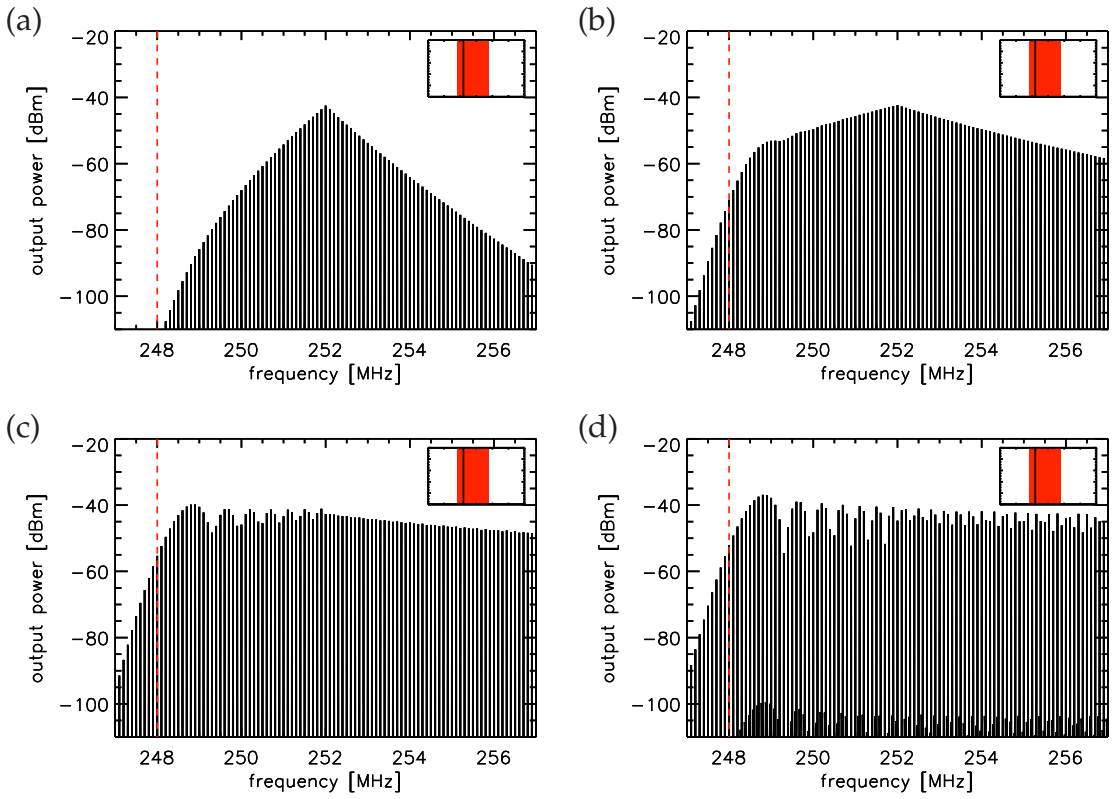

Figure III.9.: Numerical sideband structures observed for sinusoidal driving with $\nu_c = 252\,\mathrm{MHz}$, $\nu_d = \Omega/2\pi = 0.1\,\mathrm{MHz}$ near the turning point. From (a) to (d) the resistance is reduced so that (a) $\gamma = 6.4\,\mathrm{MHz}$, (b) $\gamma = 2\,\mathrm{MHz}$, (c) $\gamma = 0.6\,\mathrm{MHz}$, and (d) $\gamma = 0.2\,\mathrm{MHz}$.

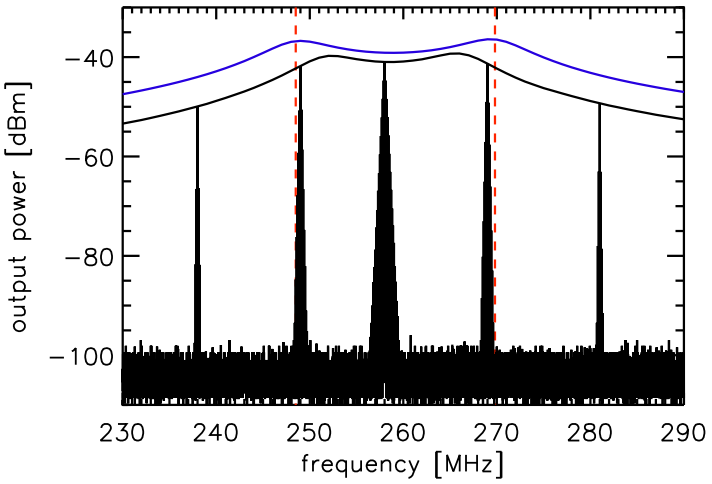

Figure III.10.: Superposition of sideband structures for five different carrier frequencies (sinusoidal driving as in figure III.8, $\nu_c = 238; 249; 258; 269; 281$ MHz). The black solid line corresponds to the envelop of the amplitude of the main peaks. The red dashed lines correspond to the turning points, the blue solid line to the envelop of the amplitude of the main peaks in the numerical calculation

envelope. The blue curve is the numerically found envelope. Red dashed lines indicate the turning points determined from the DC measurement (see figure III.3 (b)). The figure shows the highest amplitude of the main peak close to the turning points. This can be traced back to the divergency of the semiclassical wave function at the turning point, as already discussed in detail in section III.2.3. Since the envelope is symmetric with respect to the center of the modulation band the assumption that the absorption is approximately constant in case of the dynamic measurement is justified.

Rectangular driving

The realization of a rectangular driving was limited by the unavoidable distortion of the signal on the slopes at high driving frequencies. Therefore the experiments have been executed at a comparatively low frequency $\nu_d = \Omega/2\pi = 1\,\text{kHz}$.

Due to the low frequency, solving equation (III.7) numerically by a Runge-Kutta method is leading to two different time scales, one has to attend. One needs small

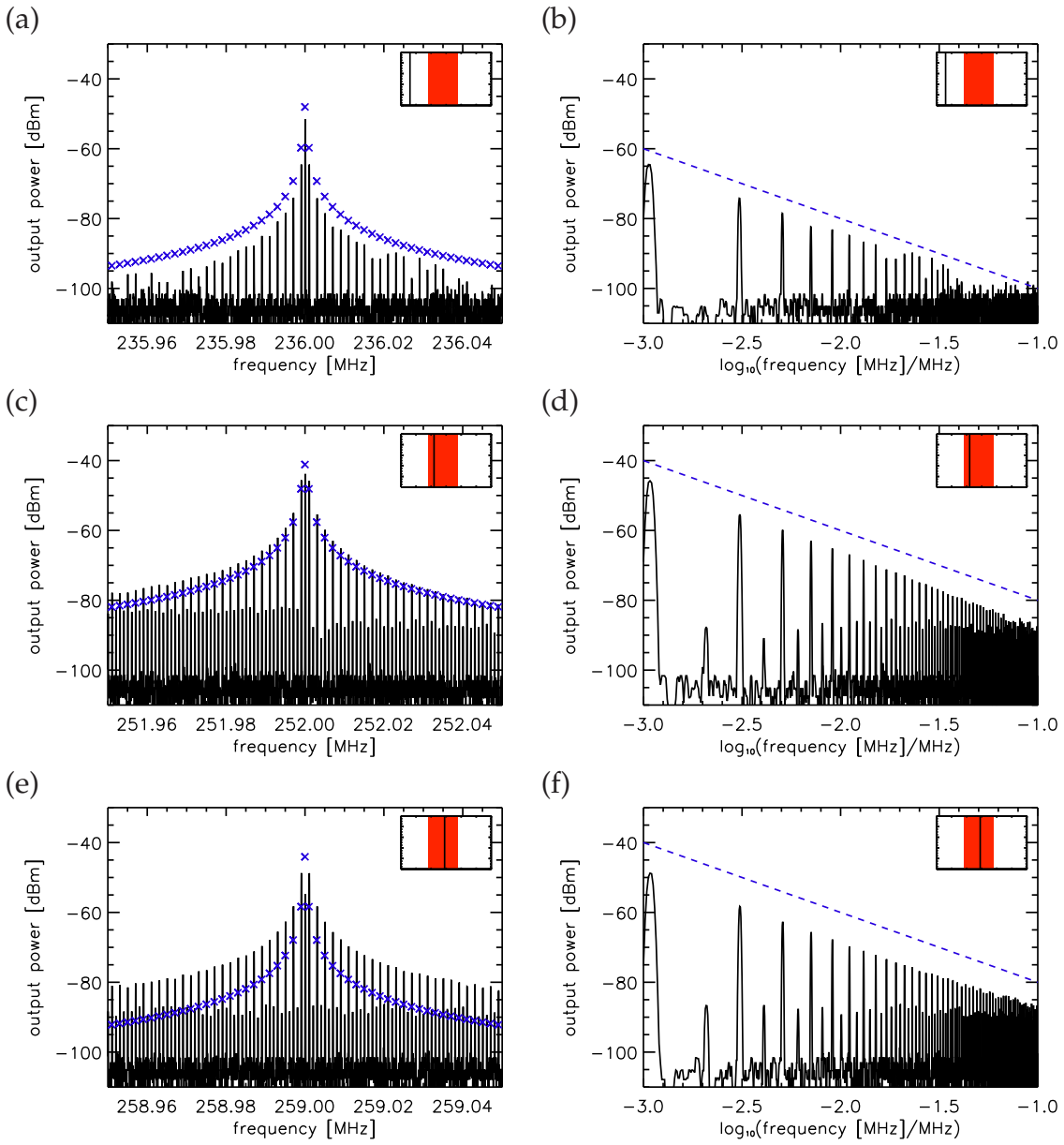

Figure III.11.: Experimentally measured sideband structure for rectangular driving are shown in logarithmic (left) and double logarithmic (right) scale. The blue crosses corresponds to the weights of the Fourier components obtained from the analytic solution of equation (III.7). On the right side the blue dashed lines corresponds to a decay with an exponent of -2.

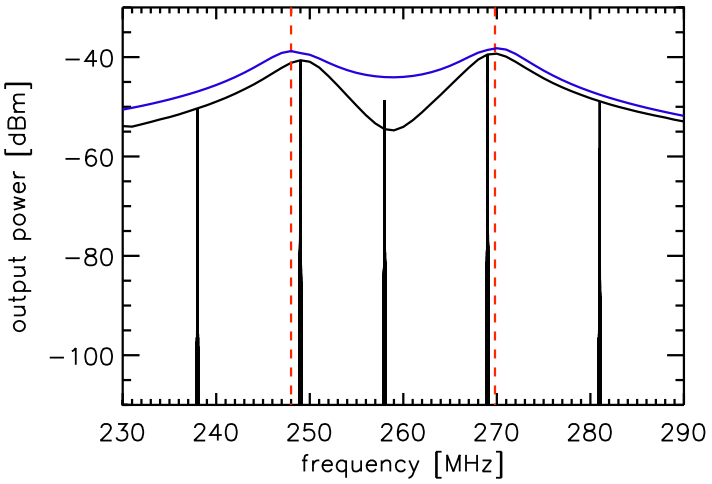

Figure III.12.: Overlay of sideband structures for different carrier frequencies (rectangular driving as in figure III.11), the black solid line corresponds to the envelop of the amplitude of the main peaks. The red dashed lines corresponds to the turning points, the blue solid line to the envelop of the amplitude of the main peaks for the analytical calculation

time steps due to the fast carrier frequency and long time intervals to simulate the slow driving frequency. Therefore numerical calculations are time consuming and inaccurate. Fortunately it is possible for the rectangular driving to solve equation (III.7) for the two different applied voltages individually (for a complete derivation see appendix J). The solution of each harmonic oscillator needs only to be matched at the switching times, i.e. leading only to a boundary value problem.

In figure III.11 (a)-(f) sideband structures for three different carrier frequencies are plotted. The right spectra are plotted on a logarithmical frequency scale which allows us to verify the expected algebraic decay. In figure III.11 (d) and (f) the power of the decay was found to be equal to -2 in accordance with the theoretical prediction. In the left column the theoretical values of the Fourier components are marked by the blue crosses. One can see a good qualitative agreement, but discrepancies in quantity. Besides the fact that the damping is extracted in the same way like in the sinusoidal driving case, the signal generator is not able to generate a precise rectangular signal. Another explanation of the observed discrepancies can be the validity of the simplified circuit in figure III.1 (d) when this description is applied to the rectangular driving.

The amplitude of the main peaks (see figure III.12) shows a behavior like in the sinusoidal driving case, but now the minimum between the turning points is significantly deeper than in the sinusoidal case. The main peak of the sideband structure may even be smaller than the first harmonic. This was not observed in the analytic results. Theoretically even harmonics vanish, experimentally they are substantially damped. The quantitative discrepancy may result from the non-perfect rectangular signal.

III.3. Single driven resonance - nonlinear regime

In the last section I presented a device for a microwave Floquet system, where a single resonance is perturbed periodically. This device is suited to introduce nonlinearities in the field of Floquet systems in a controlled way.

In fact, the system is nonlinear by its construction. A varicap is an electronic component, which is nonlinear by it self. As mentioned in section III.2.1, the capacitance is defined by the applied voltage at the varicap $\delta C_1 = g(U) \sim s \cdot U$. Due to the high offset voltage of the driving frequency ($\sim$ 2 V) in comparison to the applied carrier signal (0 dBm= 1 mW yields at a perfect 50 Ω matching $U = \sqrt{R \cdot P} \sim 0.2$ V), which is more than twice the value applied on the varicap due to $C_b > 2 \cdot C_V$ in figure III.1 (c)), this nonlinearity could be neglected for the powers chosen in section III.2. But if one increases this power, $\delta C_1(t)$ becomes dependent on the applied voltage, which is synonymic with a dependence of f. Thus the tin cup is descried by

$$\left(\frac{2(\omega_c - \omega_0)}{\omega_0} + \frac{\delta C_1(t,f)}{C} + \frac{2i\gamma}{\omega_0}\right) f + \frac{2i}{\omega_0}\dot{f} - \frac{\ddot{f}}{\omega_0^2} = 2, \tag{III.37}$$

or in accordance to equation (III.12)

$$\left(i\frac{d}{dt} + \omega_c - \omega_0 + d_1(t,f) + i\gamma\right) f = \omega_0. \tag{III.38}$$

Let us take a closer look at $d_1(t,f)$:

$$d_1(t,f) = \frac{\delta C_1(t,f)}{2C}\omega_0 = \frac{s \cdot (U_{\text{carrier}} + U_{\text{driving}})}{2C}\omega_0. \tag{III.39}$$

The change in the nominator implies a linear characteristic of the varicap, which is always acceptable in first order. $U_{driving}$ corresponds to the applied voltage by the signal generator. The more interesting part is performed by $U_{carrier}$, which is associated with the applied carrier signal by the source. To write $d_1(t,f)$ in terms of $f(t)$ we start with equations (III.5), (III.6),

$$U_{\text{carrier}} = \frac{q_1}{C_1} = u_0(t) - \frac{q_0}{C_0} \tag{III.40}$$

$$= u_0(t) - \frac{C_1}{C_0 + C_1} u_0(t) - \frac{q_2}{C_0 + C_1} \tag{III.41}$$

$$= \frac{C_0}{C_0 + C_1} u_0(t) - \frac{q_2}{C_0 + C_1}, \tag{III.42}$$

and now insert the definition $q_2(t) = -e^{-i\omega_c t} u_0 C_0 f(t)/2 = -u_0(t) C_0 f(t)/2$:

$$U_{\text{carrier}} = \frac{C_0 \cdot u_0(t)}{C_0 + C_1} \left(1 + \frac{1}{2} f(t)\right). \tag{III.43}$$

A direct consequence of this short calculation is that now the high frequency ω_c is not separable from $f(t)$. The second observation is that equation (III.38) got a quadratic nonlinearity

$$\left(i\frac{d}{dt} + \omega_c - \omega_0 + d_1(t) + h e^{-i\omega_c t}(1 + \frac{1}{2} f) + i\gamma\right) f = \omega_0. \tag{III.44}$$

We introduced $h = \frac{C_0 \cdot s \cdot \omega_0}{2C(C_0 + C_1)} u_0$ for the reason of clarity. In the paragraph after equation (III.11) we estimated the magnitude of f as $f \sim \omega_0/\Delta\omega$. As shown in the last sections this is of the order of 10, so we can write equation (III.44) in the form

$$\left(i\frac{d}{dt} - \omega_0 + d_1(t) + \frac{g}{2} + i\gamma\right) g = \kappa. \tag{III.45}$$

where g is introduced as $g = h e^{-i\omega_c t} f$ and $\kappa = \omega_0 h e^{-i\omega_c t}$. As we measure the current through the coil we can derive the measured quantity as in equation (III.13)

$$i_2 = \frac{i}{2} \omega_c C_0 g(t). \tag{III.46}$$

If we first ignore the time dependence of $d_1(t)$, we have one of the easiest possible equations to study deterministic chaos. It is very similar to the logistic map (compare [86]), which is perhaps the most used example to study bifurcation, period doubling, intermittence and many other characteristics, which are important

to understand deterministic chaos. Because of the fact that such systems were studied theoretically, numerically and also experimentally many years ago ([86, 87]) I do not want to focus on this system. A really similar system even with a varicap (at that time called varactor diode) was studied in 1981 by Linsey [88]. There he studied the period doubling route into chaos. In appendix K one example for a typical nonlinear behavior generated by this equation is shown.

A second possibility to generate nonlinearities is to consider the nonlinear characteristics of the used varicap. In principle, the dependence of the capacitance as a function of the voltage is exponential. If the range of the applied voltage is small, this does not affect the description of the circuit. If we choose a larger area, this assumption fails and $d_1(t)$ is now of the form

$$d_1(t) = \frac{\tilde{s} \cdot \exp[-U_{\text{driving}}]}{2C}\omega_0 = \frac{\tilde{s}_1 U_{\text{driving}} + \tilde{s}_2 U_{\text{driving}}^2 + \dots}{2C}\omega_0. \tag{III.47}$$

The deviation from the linear regime can be seen in figure III.3. From 0 V to 5-6 V a linear dependence of the resonance position as a function of the DC-voltage is found. Afterwards the curve flattens. This becomes clear in correspondence to equation (III.14), where the resonance position is shifted by d_1 .

In the case of sinusoidal driving this leads to additional terms in equation (III.12)

$$\left(i\frac{d}{dt} - \omega_0 + z_1 \sin(\omega_d t) + z_1 \sin^2(\omega_d t) + \dots + i\gamma\right) f = \omega_0. \tag{III.48}$$

If one thinks about trigonometric relations, for example $\sin^2(\alpha) = \frac{1}{2}(1 - \cos(2\alpha))$, one can see that this leads just to additional contributions for sidebands of higher numbers. E.g. for sinusoidal driving this might only lead to a deviation of the exponent, due to the exponentially fast decaying Taylor series of the exponential function describing the varicaps characteristics.

Obviously it is possible to combine both nonlinear dependencies if the voltage $U_{carrier}$ in equation (III.39) becomes too large for a linear description of the varicaps characteristics. This leads to higher orders of $g(t)$ in equation (III.45).

III.3.1. Nonlinear microwave Floquet system

Let us now consider the time dependence of $d_1(t)$ in equation (III.45). Up to now such systems were not studied, at least not in this context and to my knowledge.

The investigation of this nonlinear system is a future work. I will present two experimentally found effects, which are typical for nonlinear systems. First I will show a hysteresis effect. The second effect is associated with period doubling [86].

Both effects can be seen in the context of a nonlinear forced oscillator. A physical pendulum is an example as well as the in principle equivalent RLC circuit (compare e.g. sections 11 and 24 in [89]).

Hysteresis effects in nonlinear microwave Floquet systems

In appendix K it is shown for the non-driven system, how nonlinearities can become manifest in hysteresis effects. In the driven situation this is not as clear as in the non-driven case. There might be a memory effect not only for the carrier frequency, but also for the driving frequency and maybe for the carrier power as well. In addition the third parameter (ν_d) makes an easy discovery of a hysteresis impossible. In figure III.13 sideband structures for the tin cup at an input power of 15 dBm and with a driving frequency of $\nu_d = 400$ kHz are presented. With this adjustments the carrier frequency was applied in a range from 266 to 290 MHz. In the left column one can see four sideband structures chosen from a measurement series in steps of 1 MHz with increasing driving frequencies. Beginning at 290 MHz the same series was measured, but now with driving frequencies decreasing until 268 MHz. Sideband structures for the same carrier frequencies are plotted in the right column. The two sideband structures for 268 MHz are very similar as well as the two sideband structures at 290 MHz. For driving frequencies between approximately 271 MHz and 283 MHz the two sideband structures are completely different, as one can see in the two middle spectra. This is a clearly observable hysteresis effect. One can also find this effect for lower carrier powers, but then it is not as precise and obvious. By tests with lower input powers and attenuators at the signal generator it could be nearly excluded that these effects were produced by the signal generator.

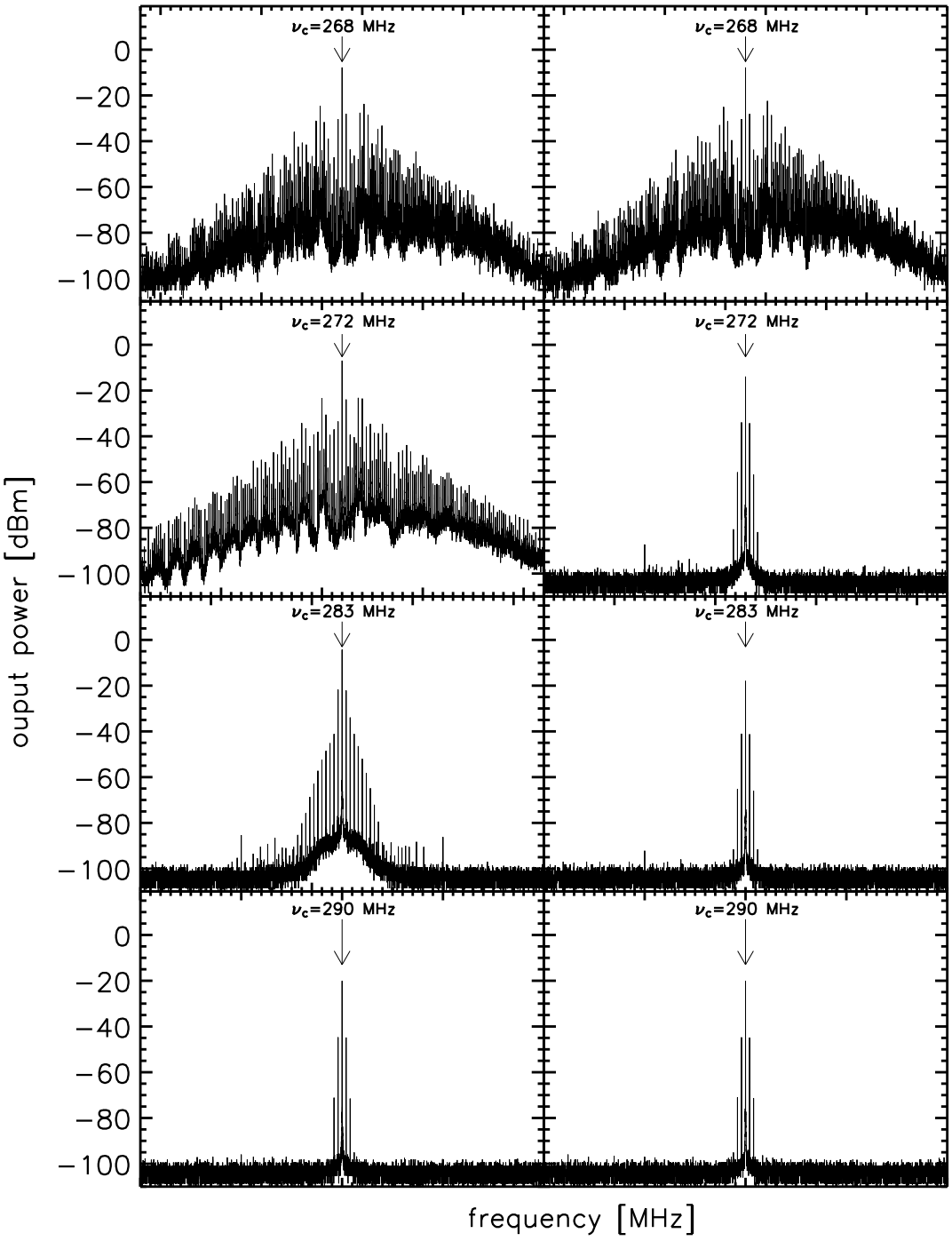

Figure III.13.: Illustration of hysteresis effect for a sinusoidal driving of 400 MHz and a carrier power of 15 dBm. The parameters for the measured spectra next to each other are identical except for the direction of the applied carrier signals. In the left column sideband structures for raising carrier frequencies in the right column for decreasing carrier frequencies.

Period doubling in nonlinear microwave Floquet system

In typical systems leading to chaos it is known since years that the so-called period doubling route to chaos can appear [86]. It was, as already mentioned, analyzed e.g. in nonlinear RLC circuits [88]. In a dirven nonlinear circuit besides the driving frequency additional frequencies with the one-half frequency, the one-third frequency and so on occurs as steps to a fully chaotic behavior.

By analyzing Floquet spectra with high input powers characteristics were found, which could be associated with this scenario. As it is not easy to extend the period doubling behavior to time-dependent nonlinear systems and this was not manageable in the context of this work I will show only two examples where these effects were found. In figure III.14 (a) and (b) spectra are plotted with two different carrier powers but with respect to the other possible parameters with the same adjustments.

In figure III.14 (a) it is clearly observable that in the spectrum for a higher applied carrier power (black) between the expected sidebands at $\nu_c, \nu_c \pm \nu_d, \nu_c \pm 2\nu_d, \ldots$ additionally sidebands occur with frequencies of $\nu_c \pm \frac{\nu_d}{2}, \nu_c \pm \frac{3\nu_d}{2}, \ldots$. As a second example one can see that in figure III.14 (b) between the typical sidebands now two equidistant sidebands occur. Up to now it was not observed that between the "new" sidebands another generation of sidebands (e.g. in figure III.14 (a) three black sidebands between the yellow ones) appear. For that reason this is not a proof of the observation of period doubling in nonlinear Floquet systems. But nevertheless there is an obvious similarity to this effect and this system can be seen as the first step of testing a period doubling scenario for nonlinear Floquet systems.

(a)

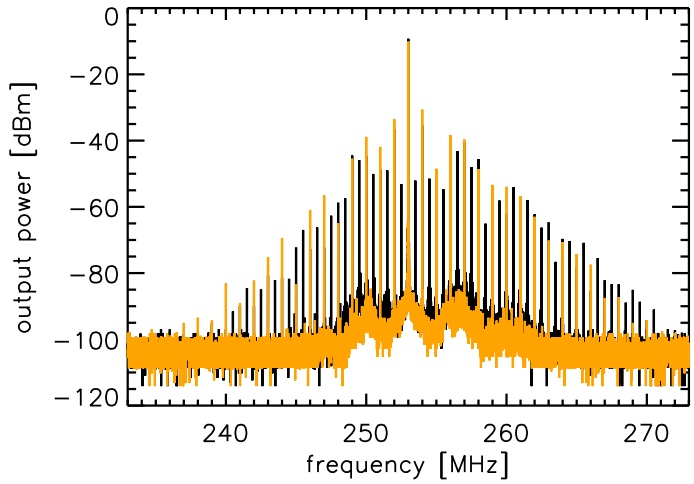

(b)

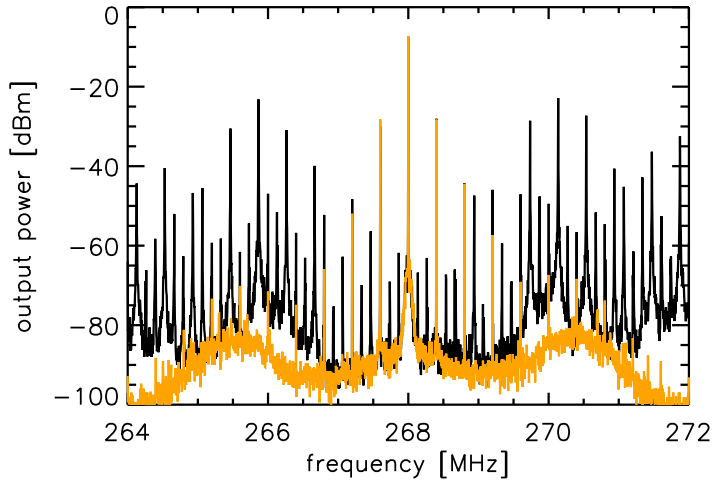

Figure III.14.: (a) Sideband structures for ν_c =253 MHz, ν_d =1 Mhz and carrier powers of 16 dBm for the black spectrum and 14 dBm for the yellow spectrum. (b) sideband structures for ν_c = 268 MHz, ν_d = 400 kHz and carrier powers of 15 dBm for the black spectrum and 12 GHz for the yellow spectrum.

III.4. Driven systems with several resonances

In the introduction the overall working schedule was presented. In sections III.2.1-III.2.4 I presented the introduction, analysis and understanding of one single driven resonance. The next step is to construct a system, where more than one resonance can be changed parametrically. Recapitulating the basic ingredients of dynamic localization the setup must have a certain frequency range, where the resonances can be shifted at least of the order of the mean level spacing. The frequency of the attached driving signal should be also by the order of the mean level spacing. It would give a big gain insight, if we could change the order of magnitude of the mean level spacing, the driving frequency and the shift of the system resonances with respect to each other.

In the following sections I will present two possibilities fulfilling the basic requirements. The first is in direct correspondence with the single driven resonant circuit and the schedule presented in the introduction. The second way was developed in a Bachelor thesis in our working group concerning the realization of quantum graphs by microwave measurements [90].

For both possibilities a proof of principle will be presented.

III.4.1. Microwave cavity

The first attempt of coupling the resonant circuit to a cavity might be a cavity with four antennas. One for the incoming signal from the signal generator and one for the outgoing signal to the spectrum analyzer. The third and fourth should lead to the channels of the tin cup. But in a basic DC measurement, which means an additional attached RLC circuit, the resonance of the circuit was not comparable with the cavity resonances. The coupling of the RLC circuit is not manageable in a way that one can think of one additional resonance in the spectrum of the whole cavity coming from the circuit.

The solution is to place the whole circuit inside the cavity. In figure III.15 (a) a sketch of the setup is presented. The RLC circuit is integrated in a wire connected to the grounding via a varicap. The circuit will now be called wire resonator,

because it is mainly a $\lambda/4$-resonator on the wire, with one effective changed capacitive termination (here to the top). A photograph of the wire resonator is given in figure III.15 (b). For preliminary measurement the cavity is cuboid with a length of $a \sim 50\,\text{cm}$, a width of $b \sim 20 - 100\,\text{cm}$ (changeable) and a height of $h \sim 10\,\text{cm}$. The height is essential for an adequate coupling to the wire resonator. Additionally the eigenfrequency of the wire resonator can be shifted in a suited frequency range. A length of $l = 10\,\text{cm}$ leads to a resonance frequency of about $\nu = \frac{c}{\lambda} = \frac{c}{4l} \sim 0.75\,\text{GHz}$.

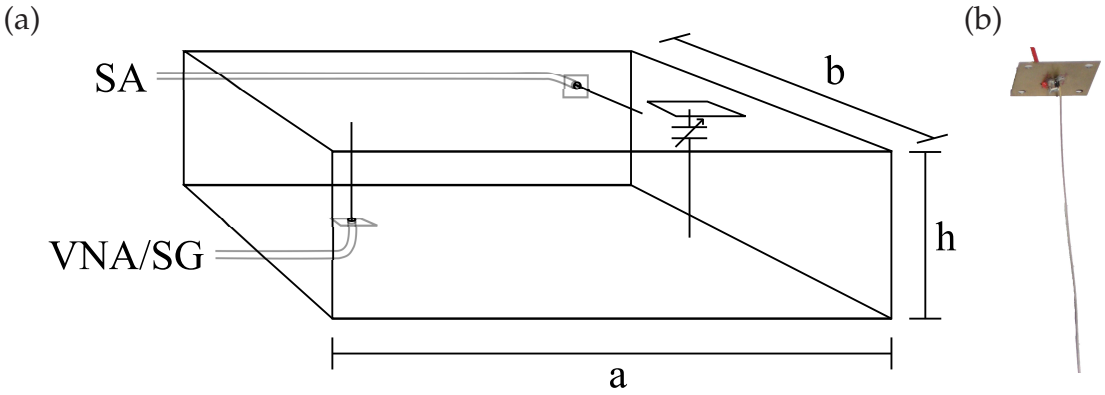

Figure III.15.: (a) Schematic illustration of the cuboid-formed resonator with the circuit in form of a wire resonator. (b) Photograph of the wire resonator

A DC- or AC-voltage can be applied at the varicap via the red cable. For static measurements the left antenna in figure III.15 (a) was used to measure the reflection signal with a vectorial network analyzer. If the wire resonator is driven the incoming signal is applied on the left cable (SG) and the spectral analyzer (SA) analyze the signal coming to the horizontal backmost antenna. The antenna were placed in this way to have a principle similarity to the tin cup (compare figure III.1 (b)). A comprehensive description and experimental analysis of this setup is an open task. Optimizations like connecting the wire antenna to the bottom plate and more suited antenna arrangements are possible and would make the description easier.

In figure III.16 spectra are presented with different applied DC voltages at the varicap. In figure III.16 (a) the width of the resonator is $b \sim 30\,\text{cm}$ in (b) $b \sim 50\,\text{cm}$. The applied voltages are in a range of 1 V to 7 V.

In the case of lower density of states (a) one can see that all three measurable modes are shifted with respect to the applied DC voltage. The shift of each mode is of the

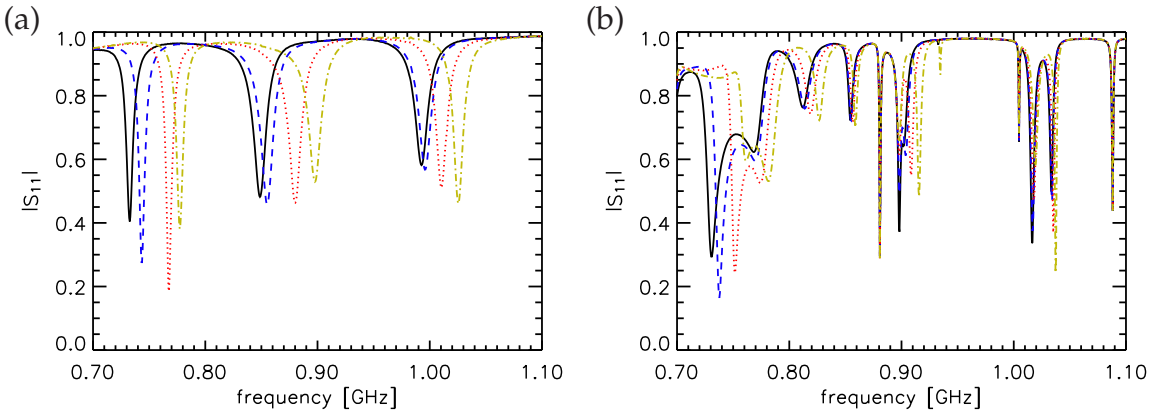

Figure III.16.: Reflection spectra for the setup shown in figure III.15 with a width of (a) $b = 30\,\text{cm}$ and (b) $b = 50\,\text{cm}$. In both figure black lines corresponds to 1 V, blue dashed to 3 V, red dotted to 5 V and green dash-dotted to 7 V applied at the varicap.

order of 50 MHz. The mean level spacing is according to $\Delta \sim \frac{c^2}{2A\cdot\pi\cdot\nu}$ approximative 100 MHz. As the mean level spacing is inverse proportional to the width b of the resonator it becomes comparable to the shift at approximatively $b \sim 60\,\text{cm}$. This is experimentally feasible. Even if the widths of the modes are already smaller than the shift, they could be decreased by better connecting the side walls with the top plate. The quality factor $Q = \langle \frac{\nu_n}{\Gamma_n} \rangle$ is about 10 in the presented measurements, for microwave cavities it is typically 500-1000. In figure III.16 (b) spectra with a higher density of states are presented. One can see very well that now some of the modes are shifted whereas others do not seem to be affected. In contrast to (a) not all modes are shifting in the same way dimension. This suggests that modes of the wire resonator couples to the modes of the cavity. For the two modes between 0.7 and 0.8 GHz one can extract the crossing behavior of the two modes and by averaging over many of such avoided crossings the coupling could be extracted.

To proof the principle working of a driven wire resonator, I present in figure III.17 a sideband structure for the setup shown in figure III.15.

The sideband structure is observable as one would expect from the similarity to the single driven system. The sidebands decay exponentially due to the sinusoidal driving of the varicap. This is a clear hint that after a comprehensive understanding of the wire resonator all peculiarities found for the single driven microwave Floquet system should be expandable to this setup. This is the point where the step

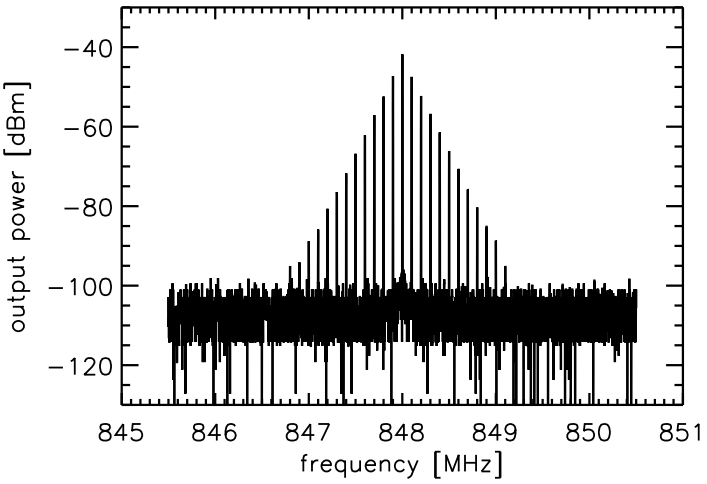

Figure III.17.: Sideband structure for the setup shown in figure III.15 with a sinusoidal AC voltage applied at the varicap. The input power is 0 dBm, $\nu_c = 848\,\text{MHz}$ and $\nu_d = 1\,\text{MHz}$.

from a single driven resonance presented in section III.2 to a system with several driven resonances can be performed.

III.4.2. Graphs

In the context of developing an optimal wire resonator device for the setup in section III.4.1 an intermediate solution was a variable reflection termination for a long antenna (a photograph of the termination is shown in figure III.18 (c)). The termination determines the phase difference between the incoming and outgoing wave. For this setup the shift of the resonance frequency was not large enough. But the principle operating of such terminations leads to the idea to use a coaxial cable terminated with such a reflection terminator. Coaxial cables can be used to form microwave graphs which are fully equivalent to quantum graphs. In figure III.18 (a) a photograph of such a device and in (b) a sketch is shown.

An introduction to quantum graphs can be found in [91, 92]. Their realization with microwave equipment was firstly investigated by Hul, Sirko and coworkers [93] and is still an active field [94].

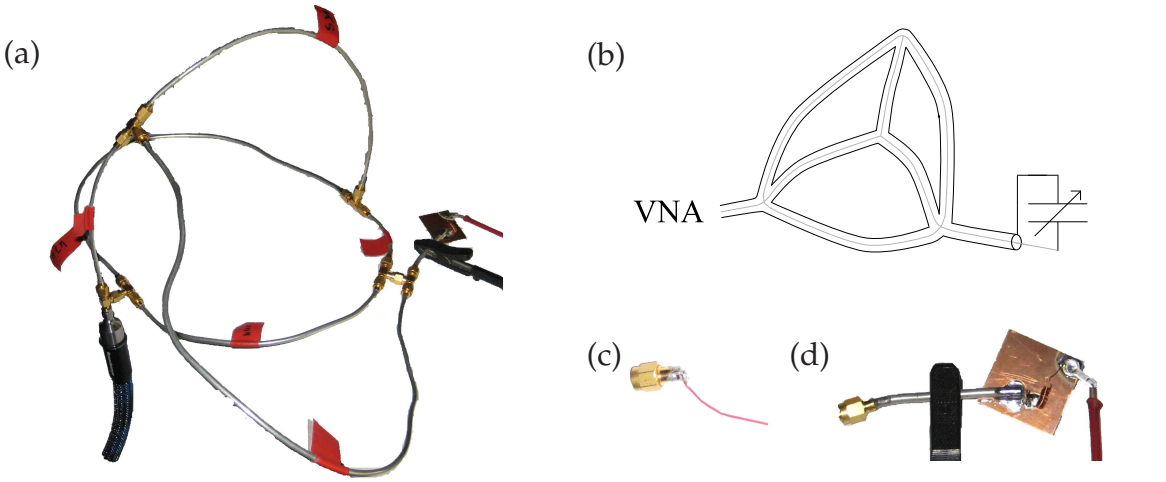

Figure III.18.: (a) Photograph of a microwave analog to quantum graph and in (b) a sketch o it. (c) a photograph of the termination using the varicap. (d) photograph of the termination using a switching diode.

The coaxial cables are connected with T-junctions giving several transmission and reflection probabilities to the other attached cables or backwards respectively. The idea for the introduction of Floquet systems is to attach at least one additional coaxial cable (in figure III.18 (b) bottom right) with the variable termination. The different phase relations for different applied voltages at the varicap can be transformed in an effective length modification. If the change of the varicap is large enough, the spectrum of the graph might be changed. In figure III.19 (a) the spectra for the same graph (see figure III.18 (a)) but with different applied voltages at the varicap are presented.

One can see that some of the modes are affected very much, whereas for example the mode at 0.66 GHz is nearly stable. Also not every shifting mode is affected in the same way. This can be understood from a semiclassical point of view, where one can see how different classical periodic orbits contribute to the spectrum. As an analysis of the spectrum is not the aim of this section, I will not go into detail.

To enlarge the observed effect of changing the spectra, instead of the varicap a switching diode was used. A photograph of the termination can be seen in figure III.18 (d). The switching diode can change from a high capacity to a nearly short circuit between inner and outer line. The spectra for the two possibilities can be seen in figure III.19 (b). In black the switching diode is operating as a conductor and in red it is operating as a short circuit. One can see two different spectra.

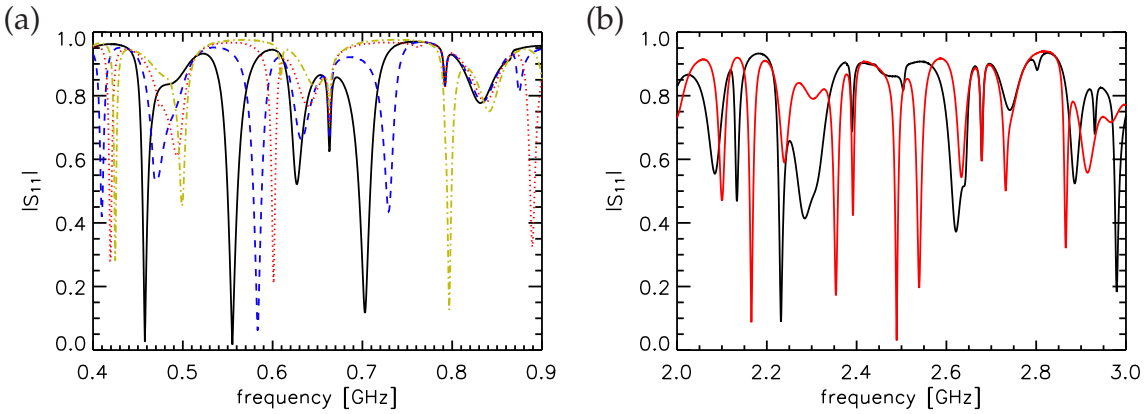

Figure III.19.: Reflection spectra for the setup shown in figure III.18 (b) with (a) the varicap and (b) the switching diode. In (a) black corresponds to 1 V, blue dashed to 3 V, red dotted to 5 V and green dash-dotted to 7 V applied at the varicap. In (b) is the black spectrum for the switching diode operating as a conductor and in red as a short circuit.

They may have some resonances in common but most resonances are completely different. The advantage of the switching diodes is that they are easy available for high frequencies (> 1 GHz), which is not the case for varicaps.

In figure III.19 (a) it is observable that the shift of the resonances is large enough to think of graphs with a mean level spacing of the order of the shift. So one can state that graphs might also be suited to perform a microwave Floquet experiment in a multi-frequency regime.

III.5. Conclusions

In this chapter I have first presented the realization of a tunable microwave system. The properties of the generated sideband structures were understood within the model of a resonance circuit with a single excited resonance. I have demonstrated the essentially different sideband structures produced by sinusoidal and rectangular driving. The decay of the sidebands could be verified as well as the expected amplitude height of the main peaks. Theoretically I have shown that for sinusoidal driving close to the borders of the modulation band sideband structures can display large oscillations. However, due to rather strong resistance of the current setup such structures have not been yet verified experimentally. The comparatively large resistance is not affecting a realization of systems which should show dynamical localization. The shown algebraic decay for sidebands generated by rectangular driving is suited to show a transition to an exponential localization in the time domain.

Then I studied non-linear effects and showed the principle arising of nonlinear equations caused by a nonlinear voltage-current characteristic of the varicap. In association with typical nonlinear systems I showed one hysteresis effect for the driven system, where the sideband structure completely changes if one changes the direction of the applied carrier frequency. Additionally a first hint of the period doubling route to chaos for driven microwave systems was presented, where additionally sidebands between those of the linear regime occur.

Until here the studies were restricted to a particular simple situation, namely one resonance circuit with just one eigenfrequency. As a next step a system with a high density of states within the modulation band was presented in two different realizations. The coupling of a wire resonator to a cavity is established and a sufficient number of modes in a wide range can be perturbed. The second idea is a more controllable setup. By changing the effective length of one edge of a microwave analogue quantum graph an easily manageable system is introduced, where also resonances at high frequencies (up to 3 GHz) could be varied in a controlled way. This opens up the field of a controllable analysis of dynamical localization. Additionally one can think of e.g. the investigation of noisy graphs [95].

Appendix

A. Mimicking quantum mechanics with microwave equipment

In the following a brief derivation of the equivalence of the Helmholtz equation for a flat cylindrical cavity and the two dimensional Schrödinger equation is given. The calculation is very similar to [9] and can be seen there more detailed.

Starting from Maxwell's equations for an electromagnetic field in three dimensions with a periodic time dependence of the $\vec{E}$ and $\vec{B}$-field, one obtains the Helmholtz equation (see e.g. section 8 [47])

$$(\Delta + k^2)\vec{E} = 0, \tag{A.1}$$

$$(\Delta + k^2)\vec{B} = 0. \tag{A.2}$$

The coordinate system should be chosen now in such a way, that the z-axis is perpendicular to the top and bottom plate. The z-component of the electric field are now 0 as well as the derivative in normal direction of the z-component of the magnetic field. The boundary conditions are in principle obtained by two different types of electromagnetic modes. Transverse magnetic (TM) and transverse electric (TE) modes have a vanishing z-component of the magnetic respectively electric field. The z-component of the electric field (TE-modes) respectively of the magnetic field (TM-mode) can be separated by a cosine (TE) or sine (TM) function (so e.g. $E_z(x,y,z) = E(x,y) \cdot \cos(n\pi z/d)$). Only TM modes with mode number 0 in z-direction exist. That means if the half of the wavelength λ is larger than the height d of the resonator

$$\lambda > 2 \cdot h, \tag{A.3}$$

only the so-called TM_0 modes can be excited. The Helmholtz-equation for the z-component of the electrical field reduces than to

$$-\left(\frac{\partial^2}{\partial x^2} + \frac{\partial^2}{\partial y^2}\right) E_z(x,y) = k^2 E_z(x,y). \tag{A.4}$$

This equation is fully equivalent to the two-dimensional stationary Schrödinger-equation

$$-\frac{\hbar^2}{2m}\left(\frac{\partial^2}{\partial x^2}+\frac{\partial^2}{\partial y^2}\right)\psi(x,y)=E\psi(x,y) \tag{A.5}$$

if one identifies

$$\psi(x,y)=E_z(x,y) \quad ; \quad E=k^2 \quad ; \quad \frac{\hbar^2}{2m}=1. \tag{A.6}$$

Therefore quantum mechanical effects can be investigated by microwave experiments if one considers equation (A.4) [9].

If one is interested in the time-dependent behavior one has to take the different dispersion relations for the electromagnetic case

$$w_{(ed)} \propto k_{(ed)} \tag{A.7}$$

and the quantum mechanical case

$$w_{(qm)} \propto k^2_{(qm)} \tag{A.8}$$

into account.

B. Spectra for stronger couplings

As it was mentioned at the end of section I.2.1, it is useful to minimize the coupling. To illustrate that, reflection spectra for two different couplings are plotted in figure B.1.

The black curve is for small coupling ($\mathrm{Re}(\lambda) \sim 0.002$) and the red dashed line for strong coupling ($\mathrm{Re}(\lambda) \sim 0.08$). The coupling was increased by using a longer and teflon coated antenna. One can see broader resonances with a higher amplitude. The regular modes seem to vanish and between them a quasi regular structure appears. The quasi degeneracy (in the neighborhood of every 1^{st} mode is a 4^{th}, etc.)

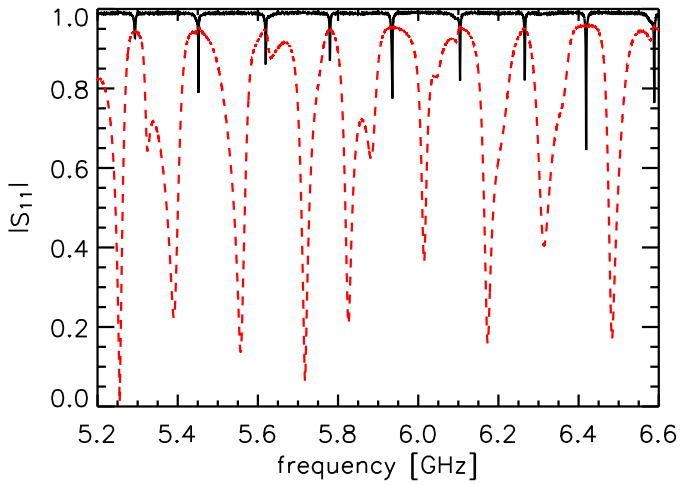

Figure B.1.: Two different reflection spectra for the same antenna position but with different antenna lengths. The black is for an antenna which extends 1 mm into the cavity. The red dashed spectrum is for a 8 mm long antenna with an additional 0.5 mm thick teflon film surrounding it.

for the weak coupling (black) is probably canceled by the antenna. One resonance became broad and deep and the other stays at its position and form Fano like profiles [96, 97, 2] like at 5.6 GHz. This can also be understood by resonance trapping as the strongly coupled antenna mimics an additional decay channel and some of the resonances take the main part of the widths and the rest stays relatively sharp [9]. Now the importance of adjusting the minimal possible coupling for the measurements in chapter I is obvious. There are a few additional resonances, which might be a hint for the third modes in the (3×3)-model presented in equation I.11.

C. Frequency depending tunneling rates - alternative analysis; other antenna position

For a clear, readable and comprehensive argumentation only one possibility to modify the experimental data was presented in the main part. For the sake of completeness, here the results for the other modification possibilities are presented

(figure C.2). In the main part the antenna coupling was considered by an approximative functional frequency dependence. In figure C.2 (a) the linear interpolation discussed in figure I.7 (b) was used. In (b) the measured amplitudes were subtracted directly.

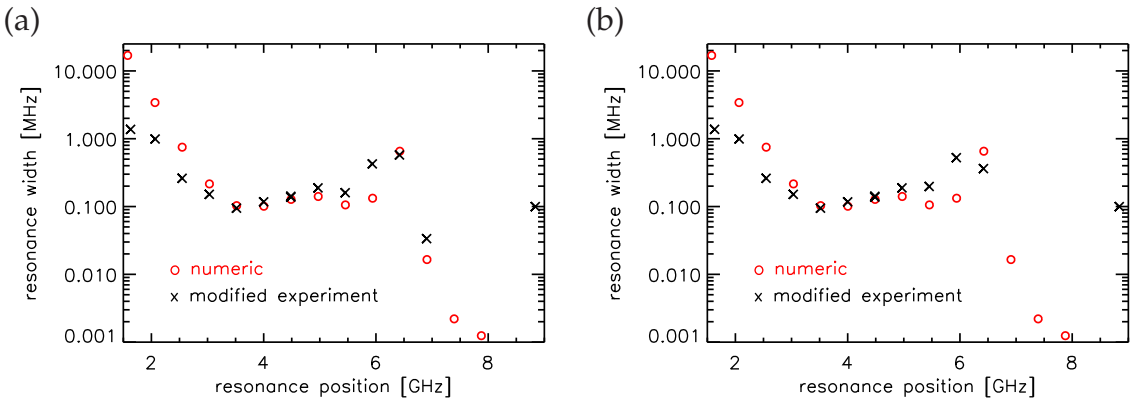

Figure C.2.: Modified experimental data by subtracting γ_{Wall} and γ_{Ant}, where γ_{Ant} are the linear fitted amplitudes (compare figure I.7 (b) black solid line) in (a) or the direct measured amplitudes (b). These measurements are performed at antenna position 1.

In both cases one can see the increase of the width at the numerical predicted position. As it is expected, for the direct subtract (figure C.2 (b)) one can see a shift to lower frequencies of the maxima, because of the high measured amplitude at 6.4 GHz. Both procedures show too small amplitudes above 6.4 GHz. Due to the very small tunneling rate the experimental uncertainties cannot resolve them, especially as the tunneling rates are becoming smaller than the measuring frequency increment the widths cannot be resolved and it is not surprising that they can be slightly negative after the modification (in the order of 0.02 MHz).

For the second and the third horizontal mode the amplitudes as function of the resonances position are plotted in figure C.3. One can clearly see the decrease of the amplitudes at 8.5-9.0 GHz for the second mode. This is in agreement with our expectation. In figure I.9 (c) one can see that this is nearly the frequency position where we expect an enhancement of the tunneling rate. In the extracted experimental widths this effect might not be noticeable due to the failing of the correction procedure. If one would pay more effort in better correction parameters, it might be possible to see the effect. It is also not useful to try to observe the resonance-assisted tunneling effect at the chosen antenna position. The amplitudes of the wave func-

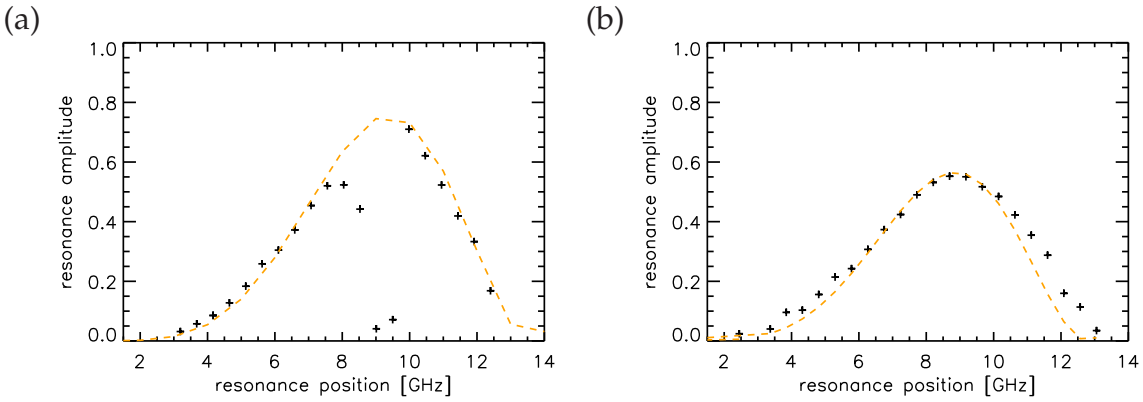

Figure C.3.: Amplitude as function of the resonance frequency for second (a) and third (b) horizontal modes. In yellow dashed lines are the correction for the diagrams in figure I.9 (c) and (d).

tion reach their maximal value here and thus the coupling to the antenna is strong. Already in this situation the antenna coupling might lead to mode splitting (for an overview see [55], calculations in [79]).

In section I.2.3 all presented measurements are performed at the antenna position 1 (blue point in I.2 (b), upper right corner). To show that the agreement presented in figure I.9 is independent of the position in figure C.4 the same series is shown, now excited at antenna position 2 (red point in I.2 (b), close to lower left corner). Here once again all three corrections are plotted. In comparison to the measurements presented in the main part the cavity was opened in between. Thus the absorber and half circle was position have changed within the precision of the experiment. That is why slight differences are expected.

In this compilation one can see that the different correction possibilities are leading to very similar results. In every situation one can see a very good agreement with the theory, only for the direct subtracting, the peak at 6.4 GHz is affected strongly. Nevertheless this is also showing a good agreement to the numerical expectations.

D. Parametric dependence of divers modes

In section I.2.4 the experimental setup was changed parametrically to analyze the effect of resonance assisted tunneling. Only evaluations for measurements at the

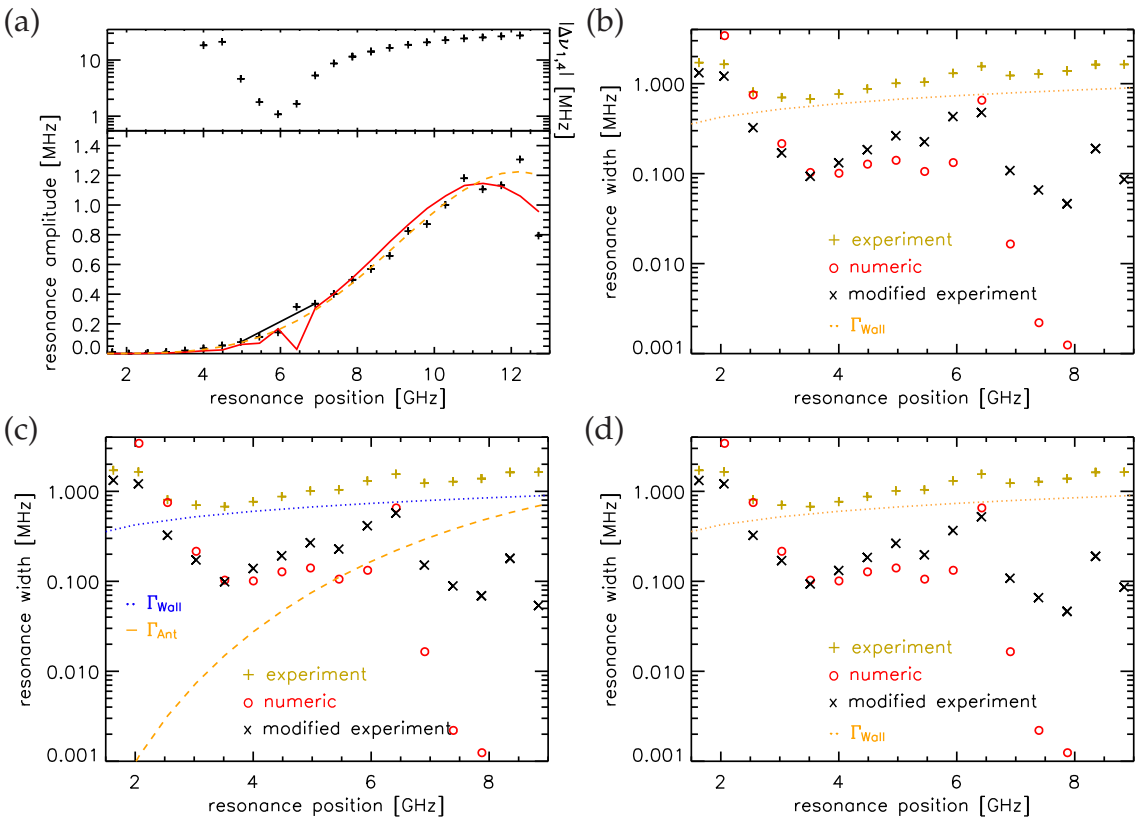

Figure C.4.: All measurements performed at antenna position 2 (red point in figure I.5). (a) amplitude of the Lorentz fits as function of the fitted resonance position. In red the amplitude of the numerical wave functions at the position of the antenna, multiplied with the coupling (as in figure I.7). The red dashed lines corresponds to an approximation like in figure I.7. In (b), (c) and (d) the modified experimental data is plotted. In (b) the measured amplitudes were subtracted directly. In (c) the approximative functional dependence (yellow dashed line) is subtracted and in (d) the linear fitted points and the other direct measured amplitudes were subtracted. Blue dotted lines corresponds to the wall absorption.

antenna position 2 are plotted. The main reason is that only there measurements were performed with the most suitable antenna. At antenna position 1 I measured with a slightly different antenna, which couples a little bit better to the system. Hence the widths are a little bit broader. In the following the same modes are presented that were shown in section I.2.4 but now at antenna position 1.

In figure D.5 it is noticeable that the crossing of the two modes happens at a slightly different position of the half circle. At this position a clear increase of the width of the first mode is seen. For the description with a (3×3)-model like in equation (I.11) the grey dashed and the yellow solid lines are plotted. In this situation deviations are found. The main reason is the changing amplitude as a function of the parameter. It changes in the order of 0.05 MHz which is 50% of the height of the enhancement of the first mode. This variation might be caused by the stronger coupling to the billiard. Such an enhancement was also found for the measurement series for antenna position 2, but not to the same extend. It is also noticeable that the last three points of the diagram (above 0.503) showed deviations in every evaluation of single modes (here noticeable in figure D.6). Although a clear enhancement in the case of the crossing of the two regular modes is presented.

I also present the parametrical dependence of the mode at approximately 6.4 GHz. Remembering that by starting at the half circle position of 0.5 and decreasing this value we would expect a decrease of the width of the first mode.

Figure D.6 shows clearly another resonance, which in this case also shows a width decrease of about 0.4 GHz.

To clarify that the chosen crossing is not an individual case, in the following additional parametrically changed modes are presented for excitations at antenna position 1.

Figure D.7 (a) to (d) show four different crossing behaviors. In (a) another simple and clear crossing is observable. As the angle of the crossing of the real part is smaller, the range of the increase of the width of the first mode is larger. Figure D.7 (b) shows that also the dependence of the 4^{th} mode do not have to be monotonic. One can think of an interaction with left chaotic modes, which are performing an additional avoided crossing. It is very interesting that if the real part of the fourth mode is increasing the width of the first mode is not affected. Therefor I assume that in this part this is not a 4^{th} mode any more and thats why the coupling is very

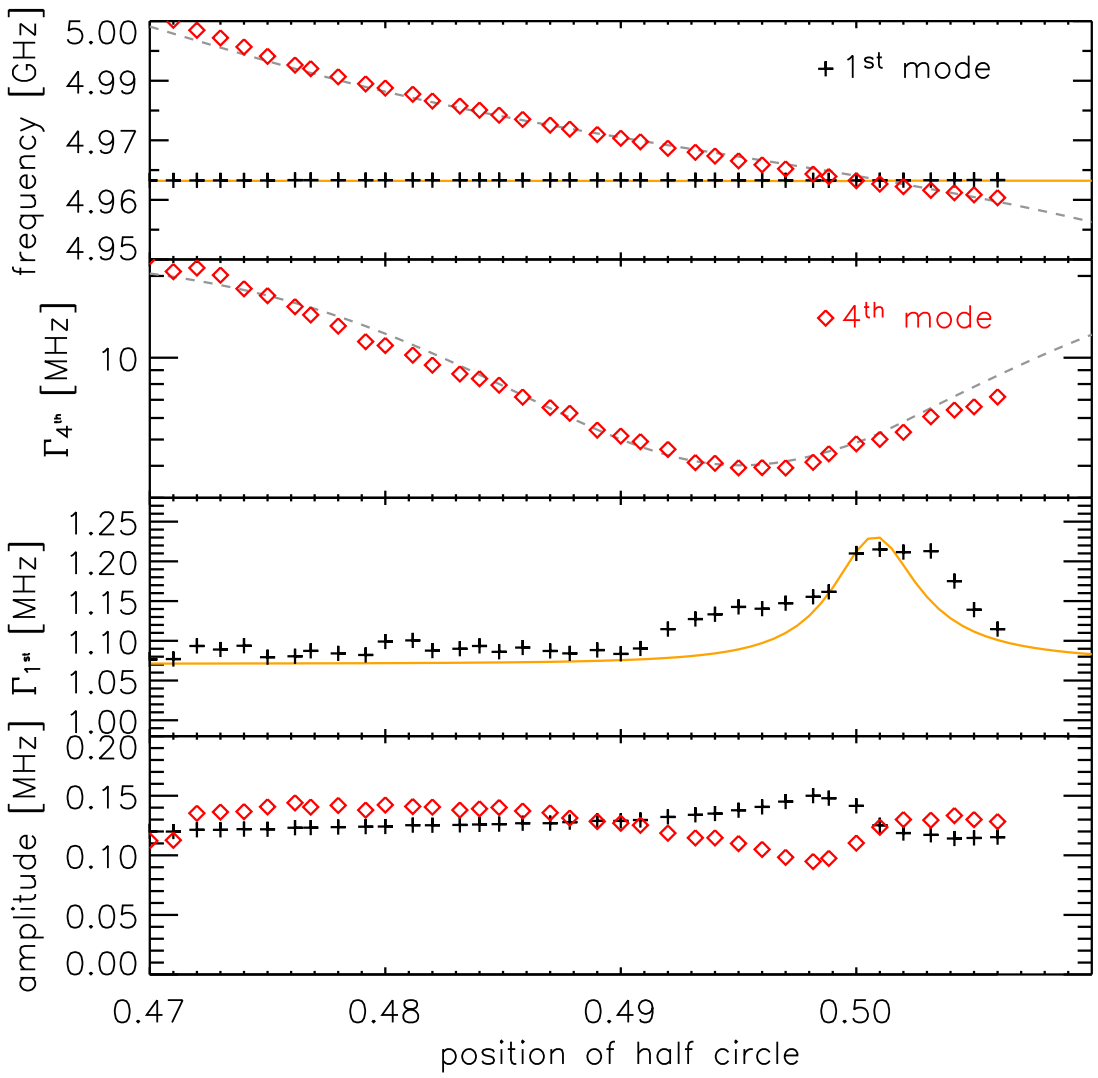

Figure D.5.: Resonance positions and widths of the two interacting modes near 4.97 GHz as a function of the half circle position. On top resonance positions of the first (black pluses) and fourth (red diamonds) mode. In the upper middle the width of the fourth mode and on lower middle the width of the first mode. In all three diagrams underlying numerical results out of the 3-matrix model. To explain the deviations the amplitudes of the modes are plotted on the bottom.

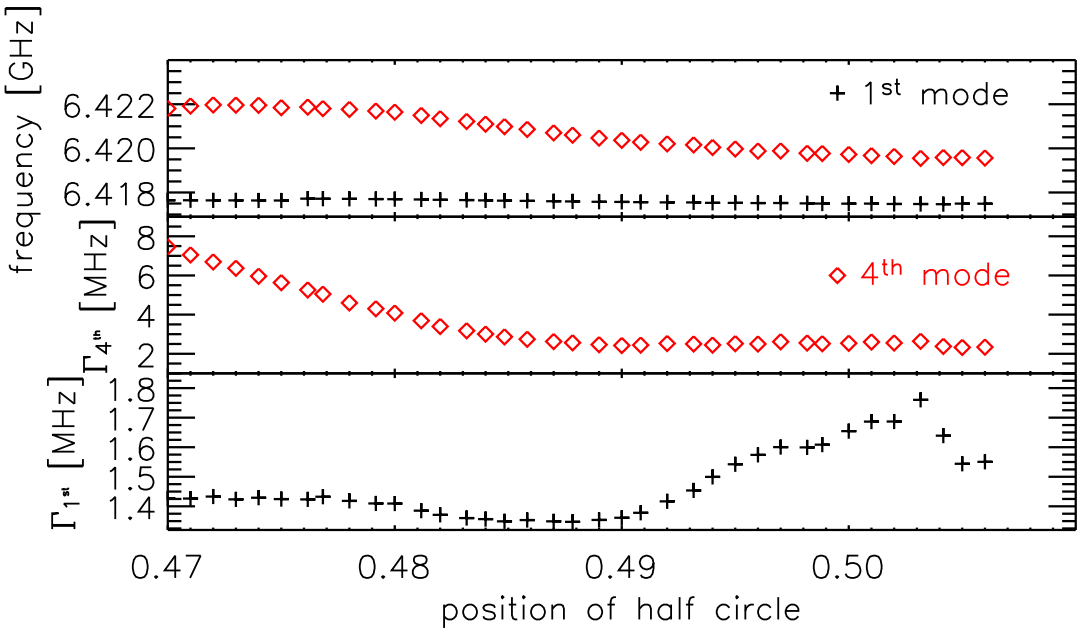

Figure D.6.: Resonance positions and widths of the two interacting modes near 6.42 GHz as a function of the half circle position. On top resonance positions of the first (black pluses) and fourth (red diamonds) mode. In the middle the width of the fourth mode and on the bottom the width of the first mode.

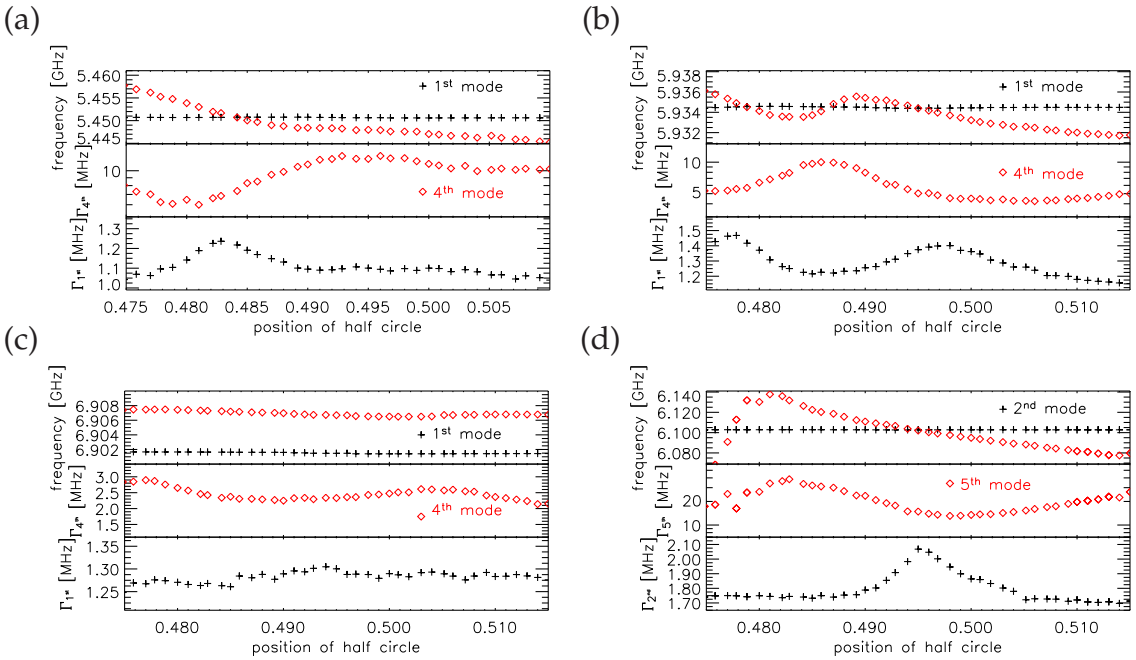

Figure D.7.: Resonance positions and widths of the two interacting modes near 5.46 GHz; 5.94 GHz; 6.91 GHz and 6.1 GHz (now second and fifth modes) as a function of the half circle position. On top resonance positions of the first (2^{nd}) (black pluses) and fourth (5^{th}) (red diamonds) mode. In the middle the width of the fourth mode and on the bottom the width of the first mode. In (a), (b) and (d) a logarithmic scale in the middle, in (c) a linear.

different. In (c) a situation is presented where the real parts do not cross and so no enhancement of the width of the first mode is expected. This example was chosen to clarify that such sharp resonant like enhancements of the first modes only arises in the case of a crossing of the two regular modes. Additionally in figure D.7 (d) a crossing of a second and a fifth mode is presented, as we also expect a resonance-assisted tunneling effect if these two mode are coming close in energy.

E. Resonance-assisted tunneling description by (2×2)-model

In section I.2.4 it was mentioned that one could also model the resonance assisted tunneling by a (2×2)-model. Again we calculate the quantum mechanical energies(E) and widths(Γ) out of the electromagnetic ones. The Hamiltonian is then of the form

$$\mathcal{H} = \begin{pmatrix} E_1 - i\frac{\Gamma_{nat,1}}{2} & \mathcal{V}_{3:1} \\ \mathcal{V}_{3:1} & E_4(d) - i\frac{\Gamma_{nat,4}(d)}{2} \end{pmatrix} \tag{E.9}$$

The frequency dependence of the fourth mode has to be considered by an appropriate function. For the real part again a linear slope was used, whereas the imaginary part ($\gamma_{nat,4}(d)$) was reproduced by a cosine shaped function. Only the coupling is now a free parameter and can be found with nearly no deviations (just 2-3%) of the theoretical value. The experimental data with the fits are presented in figure E.8.

For the width I used the dependence $\gamma_{nat,4}(d) = 14.8 - \cos\left((d - 0.4945) \cdot 100\right)\,\mathrm{MHz}$, with the half circle position d. To verify that the functional dependence of the width of the broad mode is not important for the extraction of the enhancement of the tunneling process, I plotted in the middle and bottom part an additional grey dashed line. This lines corresponds to a constant width of the broad mode $\gamma_{nat,4}(d) = 5.2\,\mathrm{MHz}$. One can clearly see that also this assumption for the second mode is leading to a similar agreement as the curved dependencies.

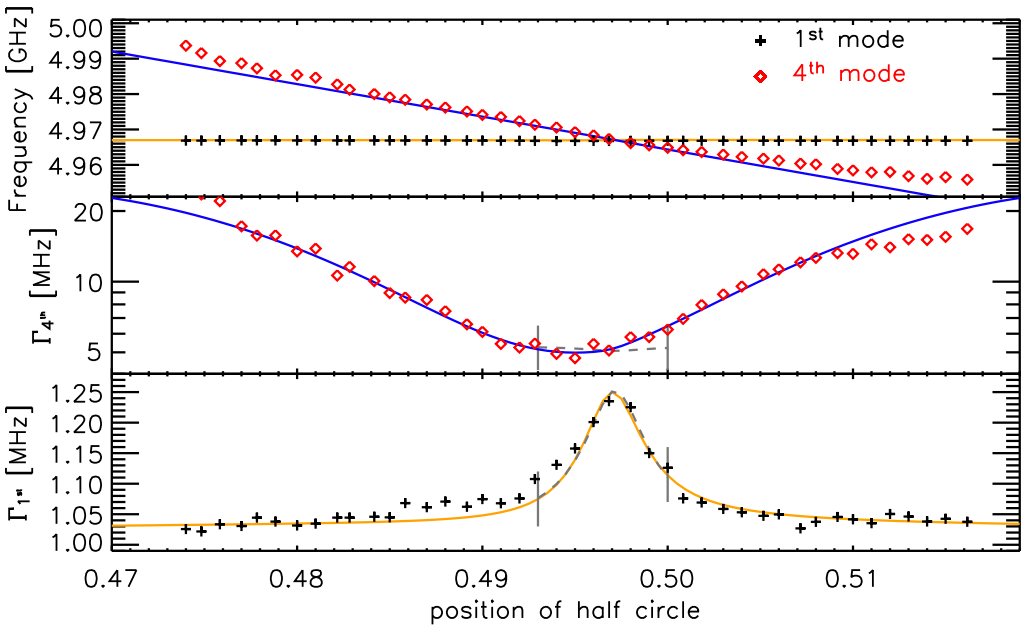

Figure E.8.: Resonance positions and widths of the two interacting modes near 4.98 GHz as a function of the half circle position. On top resonance positions of the first (black pluses) and fourth (red diamonds) mode are plotted. In the middle the width of the fourth mode and on the bottom the width of the first mode. In addition the numerical values due to a (2×2)-model are plotted for the first mode in yellow and for the fourth mode in blue.

F. Width characteristics by opening an one dimensional potential well by one realistic absorbing wall

In the context of the chosen parameters for the (3×3)-model in section I.2.4 (equation (I.11)) it was mentioned that the width of the channel resonance is surprisingly small ($\sim 70\,\mathrm{MHz}$). To understand this characteristics one can reduce the problem to a one dimensional situation [98]. One considers an one dimensional system with one absorbing wall and one hard reflecting wall at a distance of L (compare figure F.9). In the sketch the left wall represents the absorber (marked as hatched line) and the right solid line represents the hard wall.

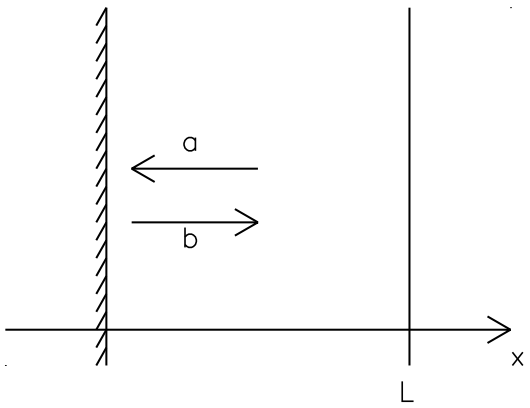

Figure F.9.: Sketch of a one dimensional potential well with one absorbing wall (left).

As in the sketch symbolized the wave function is of the form

$$\psi(x) = ae^{-ikx} + be^{ikx}. \tag{F.10}$$

The reflection coefficient R is defined as

$$R = \frac{a}{b} = |R|e^{i\phi}. \tag{F.11}$$

The reflection at the right wall ($\psi(L) = 0$) is leading to

$$b = -ae^{-2ikL} \tag{F.12}$$

$$\Rightarrow \quad R = -e^{-2ikL} = |R|e^{i\phi} \tag{F.13}$$

$$\Rightarrow \quad -e^{-2ikL - i\pi - \ln|R| - i\phi} = 1 \tag{F.14}$$

$$\Rightarrow \quad 2ik_nL + i\pi + \ln|R| + i\phi = 2\pi in \tag{F.15}$$

$$\Rightarrow \quad k_nL = \frac{\pi}{L}\left(n - \frac{1}{2} - \frac{\phi}{2\pi}\right) i\gamma \tag{F.16}$$

with

$$\gamma = -\frac{1}{2L}\ln|R|. \tag{F.17}$$

The level distance for this one dimensional situation is

$$\Delta = \frac{\pi}{L} \tag{F.18}$$

and so we end up with

$$\gamma = -\frac{\Delta}{2\pi}\ln|R|. \tag{F.19}$$

In the situation of section I.2.4 we can mimic the two dimensional system by a quasi one dimensional model with M open channels, where M is the number of half wavelengths corresponding to the length of the absorber. For a frequency of 5 GHz this means by a length of the absorber of approximately $l = 20\,\text{cm}$

$$M = \frac{l}{\lambda/2} = \frac{2 \cdot l \cdot \nu}{c} = \frac{2 \cdot 0.2\text{m} \cdot 5 \cdot 10^9 1/s}{3 \cdot 10^8 m/s} \sim 7. \tag{F.20}$$

For that reason we can estimate the width of the modes as

$$\gamma \sim -\Delta \ln|R|. \tag{F.21}$$

G. Scattering theory for open quantum mechanical systems

As the calculation of scattering matrices out of the so-called Heidelberg-ansatz is well known from multiple publications, also from our group, I will just give a short introduction. For a complete derivation see e.g. [9].

As it was shown in appendix A there is a complete correspondence between the electromagnetic Helmholtz equation and the quantum mechanical Schrödinger equation. Therefor we use technics well known from scattering in nuclear physics. In addition of the excitation and measuring of the antennas we want also to model the wall absorption. Similar to nuclear physics we mimic them by decay channels. A nice picture for that is, if one imagine the walls of the cavity as parallel attached channels with a certain reflection and transmission coefficient. The derivation starts at the general definition of the scattering matrix

$$b = Sa. \tag{G.22}$$

Here the vector a denotes the amplitudes of the incoming waves and b of the outgoing. As we handle the antennas as equal channels like the walls a and b corresponds to i antenna channels and j wall channels. As we use dipole antennas we have to solve a boundary value problem which matches the incoming waves in the antenna with the field inside the cavity (calculated by the unperturbed Hamiltonian) and in addition with the outgoing antennas. In the same manner we have to match the wave function of the cavity with the boundary conditions of the wall channels. This can be done by a Green function method. The scattering matrix is now of the form

$$S = \frac{\mathbb{1} - W^{\dagger} G W}{\mathbb{1} + W^{\dagger} G W}. \tag{G.23}$$

The matrix G is the quantum mechanical Green function of the unperturbed system and W contains the information of the coupling of the channels to the quantum mechanical wave functions. This is considered by the overlap of the n^{th} wave func-

tion in the cavity $\psi_n(r)$ with the wave function in the k^{th} channel $u_k(r)$ (a channel can be either an antenna or a wall channel!)

$$W_{nm} = \int \psi_n(r) u_k(r) dr. \tag{G.24}$$

After some mathematics one ends up with

$$S(E) = \mathbb{1} - 2iW^{\dagger} \frac{1}{E - \mathcal{H}_0 + iWW^{\dagger}} W. \tag{G.25}$$

That means that now the poles of the scattering matrix are the eigenvalues of the Hamiltonian

$$\mathcal{H} = \mathcal{H}_0 - iWW^{\dagger}, \tag{G.26}$$

which one can call an effective Hamiltonian. As already mentioned these calculations are well known and for reasons of comparability to the more complete derivations I used the same notations as in [9].

H. Global phase calibration

In theory e.g. equation (G.25) it is assumed that $\langle \mathrm{Im}(S) \rangle = 0$ and $S_{aa} = 1$ if there is no resonance. For that reason one should take attention to the global phase of the reflection spectra.

With modern calibration devices for vectorial network analyzer (VNA) it is possible to calibrate nearly every effect performed by the cables connecting the VNA with the dipole antennas. Unfortunately the dipole antenna and its component coupling the cable (engineers call them chassis jack) have a phase development. This is caused by the conductivity while passing the top plate and an unperfect attachment of the cable to the chassis jack. In figure H.10 (a) the real and imaginary part of the reflection signal are plotted.

To consider this effect in the data one measurement was performed without any cavity. This free radiation contains mainly only the phase effect of the chassis jack.

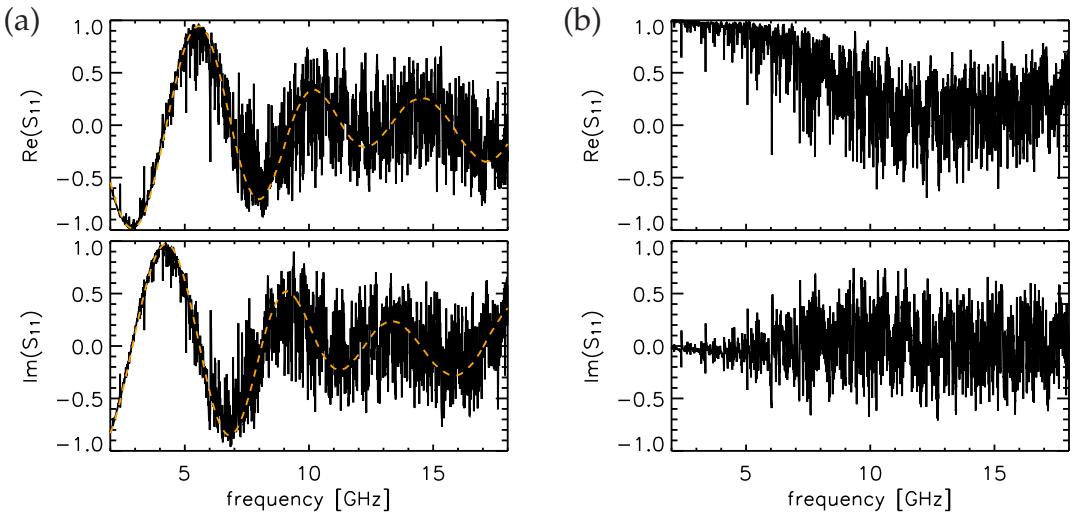

Figure H.10.: Real and imaginary part of the reflection spectrum before (a) and after the phase calibration (b). In (a) the global phase measured by a free radiance in plotted in yellow.

This is illustrated by the yellow dashed line in H.10 (a). A so-called phase calibration can be performed which rotates the measured spectrum in the complex plane in such a way that the real and imaginary part of the reflection spectrum are of the form represented in figure H.10 (b). The main advantage is, that the reflection spectrum is now mainly real.

I. Capacity and inductivity of the tin cup

The capacity of the tin can be estimated by the assumption of a cylindrical capacitor. Its capacity is given by [83]

$$C = 2\pi\epsilon_0\epsilon_r h \frac{1}{\ln(D/d)}, \tag{I.27}$$

where d is the diameter of the inner cylinder ($d = 1.5\,\text{cm}$) and D of the outer one ($D = 10\,\text{cm}$). The height h of the tin cup is 12 cm. The capacity is then

$$C = 2\pi 8.85410^{-12} 1 \cdot 0.12 \frac{1}{\ln(10/1.5)}\,\text{F} \sim 3.5\,\text{pF}. \tag{I.28}$$

The inductivity can be calculated analogously to a cylindrical capacitor and is calculated in many electrical engineering text books for a coaxial cable (see e.g. section 2.1 in [82]). As we are in a high frequency regime only the inductivity of the outer cylinder is contributing

$$L = \frac{\mu_0 \mu_r h}{2\pi} \ln(D/d). \tag{I.29}$$

With the diameters of the tin cup it is

$$L = \frac{4\pi \cdot 10^{-7} \cdot 1 \cdot 0.12}{2\pi} \ln(10/1.5) \sim 45\,\text{nH}. \tag{I.30}$$

For a resonance circuit the eigenfrequency is calculated by

$$\nu = \frac{1}{2\pi\sqrt{(CL)}} \sim 400\,\text{MHz}, \tag{I.31}$$

which is the expected range and leads to the measured eigenfrequency of the whole circuit if one considers the varicap, which has an capacity of $\sim 10\,\text{pF}$.

J. Analytic calculation of sidebands generated by rectangular driving

If one would like to solve the differential equation (compare equation (III.7))

$$C(t)\ddot{Q} + \frac{R_L C(t)}{L}\dot{Q} + \frac{1}{L}Q = C_0 u_0 \cos(\omega_c t), \tag{J.32}$$

where $C(t)$ is a rectangular function, which means that

$$C(t) = \begin{cases} C_A, & \text{for} \quad 0 < t < T/2 \quad \text{(interval A)} \\ C_B, & \text{for} \quad T/2 < t < T \quad \text{(interval B)}. \end{cases} \tag{J.33}$$

That means in particular that the converted equation (J.32) which is now

$$\ddot{Q} + \frac{R_L}{L}\dot{Q} + \frac{1}{LC(t)}Q = \frac{C_0 u_0}{LC(t)} \cos(\omega_c t), \tag{J.34}$$

becomes just an universal oscillator equation in two different intervals (A and B). These equations

$$\ddot{Q}_A + \frac{R_L}{L}\dot{Q}_A + \frac{1}{LC_A}Q_A = \frac{C_0 u_0}{LC_A}\cos(\omega_c t) \tag{J.35}$$

$$\ddot{Q}_B + \frac{R_L}{L}\dot{Q}_B + \frac{1}{LC_B}Q_B = \frac{C_0 u_0}{LC_B}\cos(\omega_c t) \tag{J.36}$$

can be solved and have to be conformed with the boundary conditions:

$$Q_A(T/2) = Q_B(T/2) \tag{J.37}$$

$$Q_A(0) = Q_B(T) \tag{J.38}$$

$$\dot{Q}_A(T/2) = \dot{Q}_B(T/2) \tag{J.39}$$

$$\dot{Q}_A(0) = \dot{Q}_B(T). \tag{J.40}$$

For the solution of equation (J.35) and equation (J.36) one needs the general solution of the homogeneous differential equation and one special solution of the inhomogeneous differential equation. The inhomogeneous solutions are

$$Q_{A,inh} = \frac{f_A}{\sqrt{(\omega_A^2 - \omega_c^2)^2 + \omega_c^2/\tau^2}}\cos\left(\omega_c t - \alpha_A\right) \tag{J.41}$$

$$Q_{B,inh} = \frac{f_B}{\sqrt{(\omega_B^2 - \omega_c^2)^2 + \omega_c^2/\tau^2}}\cos\left(\omega_c (t - T/2) - \alpha_B\right), \tag{J.42}$$

where $\tau = L/R$, $f_K = C_0 u_0/(LC_K)$, $\omega_K = 1/\sqrt{LC_K}$ and $\alpha_K = \arctan\frac{\omega_c/\tau}{\omega_K^2 - \omega_c^2}$ for $K = A, B$. Possible representations of the full homogeneous solutions are

$$\begin{aligned} Q_{A,hom} = \quad & A_c \cos\left(\omega_A t\right)e^{-\tau t} + \\ & A_s \sin\left(\omega_A t\right)e^{-\tau t} \end{aligned} \tag{J.43}$$

$$\begin{aligned} Q_{B,hom} = \quad & B_c \cos\left(\omega_B (t - T/2)\right)e^{-\tau(t - T/2)} + \\ & B_s \sin\left(\omega_B (t - T/2)\right)e^{-\tau(t - T/2)}. \end{aligned} \tag{J.44}$$

Now it is only a question of studiousness to determine A_c, A_s, B_c and B_s in such a way that the boundary conditions (equation (J.37) to equation (J.40)) are fulfilled. A complete expression of these pre-factors is not manageable due to the big amount of parameters. For the analytic results presented in section III.2.4, A_c, A_s, B_c and

B_s were calculated for the concrete parameters for each measurement. To get the amplitude of the sidebands one has just to calculate

$$c_n = \int_0^{T/2} (Q_{A,in} + Q_{A,hom}) e^{i(\frac{2\pi n}{T})t} + \int_{T/2}^{T} (Q_{B,in} + Q_{B,hom}) e^{i(\frac{2\pi n}{T})t}, \tag{J.45}$$

due to the periodicity in T. To see the overall behavior we just perform the real part of the first integral in equation (J.45)

$$\begin{aligned} Re[c_{n,A}] &= \int_0^{T/2} (Q_{A,in} + Q_{A,hom}) \cos(\frac{2\pi n}{T}t) \\ &= \int_0^{T/2} \tilde{f}_A \cos(\omega_c t - \alpha_A) \cos(\frac{2\pi n}{T}t) + \\ &\quad \int_0^{T/2} \left[A_c \cos(\omega_A t) e^{-\tau t} + A_s \sin(\omega_A t) e^{-\tau t}\right] \cos(\frac{2\pi n}{T}t), \end{aligned} \tag{J.46}$$

where $\tilde{f}_A$ is the whole pre-factor of equation (J.41). The first integral in equation (J.46) can be calculated for $n \neq \omega_c T/(2\pi)$ to

$$\begin{aligned} &\int_0^{T/2} \tilde{f}_A \cos(\omega_c t - \alpha_A) \cos(\frac{2\pi n}{T}t) = \\ &\frac{1}{2} \int_0^{T/2} \tilde{f}_A \cos((\omega_c + \frac{2\pi n}{T})t - \alpha_A) + \\ &\frac{1}{2} \int_0^{T/2} \tilde{f}_A \cos((\omega_c - \frac{2\pi n}{T})t - \alpha_A) = \\ &\frac{1}{2(\omega_c + \frac{2\pi n}{T})} \left[\sin((\omega_c + \frac{2\pi n}{T})T/2) - 1\right] + \qquad \text{(J.47)} \\ &\frac{1}{2(\omega_c - \frac{2\pi n}{T})} \left[\sin((\omega_c - \frac{2\pi n}{T})T/2) - 1\right]. \qquad \text{(J.48)} \end{aligned}$$

The first part (equation (J.47)) can be neglected, because it is relatively small (see the sum in the denominator). The second part (equation (J.48)) shows a pole for $n = \omega_c T/(2\pi)$ and decays in an algebraic way, where the power is minus one.

Since this is the leading term it is the reason for the algebraic decay with the power of -2 due to the fact that one measures the power which is proportional to the square of the current. All the other terms are performing an offset or an additional algebraic decay with the power of -2.

K. Foldover in a nonlinear RLC-circuit

In the textbook of Landau and Lifschitz (compare section 29 in [99]) it is shown that for a nonlinear driven pendulum an effect called foldover can occur. The resonance curve is becoming a wave like form. That means that the amplitude of the driven pendulum can have more than one possible value for one driving frequency. It is determined by the starting condition which amplitude arises. In our specific situation this condition is the frequency range from which the system is coming. Either it is coming from frequencies higher than the resonance frequency or from lower frequencies. In this context I want to use the term hysteresis. It is a memory effect, because the system is choosing its amplitude depending on its past.

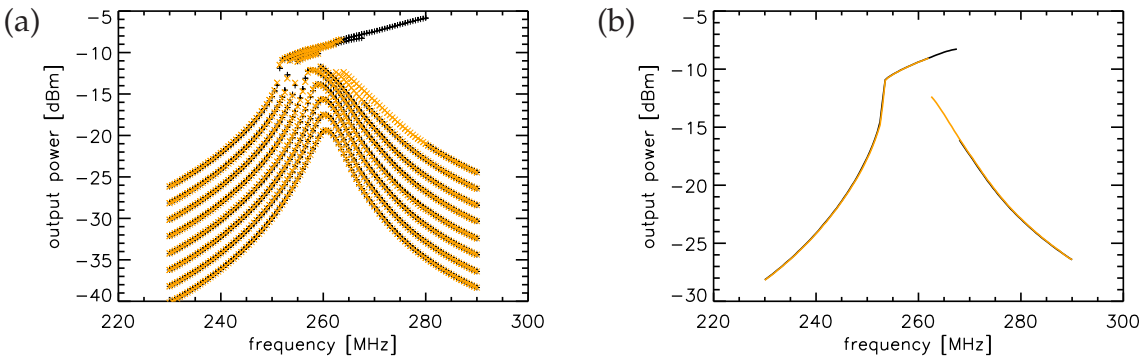

Figure K.11.: Amplitudes of the excited oscillation as a power output. (a) for different powers of the driving signal, (b) for one special input power. black plusses/line for increasing frequencies, yellow crosses/line for decreasing frequencies.

To find this effect I measured the non driven Floquet system (figure III.1, equation (III.45)). The system was excited by the signal generator, to excite only one frequency without any drift in the frequency range. Comparable experiments with a vector network analyzer are not suited due to the fixed frequency direction (the signals are created in a different way in the two devices). The outcoming signal

is measured with the spectrum analyzer where just the amplitude of the peak was extracted. In figure K.11 (a) and (b) the results are presented.

In (a) one can see that for higher excitation powers the resonance structure is becoming asymmetric and at the end a fold over occurs. In the left figure resonance curves for input powers of -4,-2,0,2,4,6,8,10 dBm are plotted in the same window. The lowest two curves are nearly just shifted by the difference of their excitation power. For higher powers the difference is becoming non-uniform. Up to a certain value of the input power the resonance curve seems to become discontinuous and for the highest two curves there is a clear difference between the increasing driving frequency and the decreasing driving frequency. To visualize the effect better in figure K.11 (b) only the two resonances curves are plotted for the same setup, but with different directions the frequencies are coming.

Bibliography

[1] W. H. Zurek. Decoherence, einselection, and the quantum origins of the classical. *Rev. Mod. Phys.*, 75:715, 2003.

[2] A. Bärnthaler, S. Rotter, F. Libisch, J. Burgdörfer, S. Gehler, U. Kuhl, and H.-J. Stöckmann. Probing decoherence through Fano resonances. *Phys. Rev. Lett.*, 105:056801, 2010.

[3] S. Gehler. Probing decoherence through Fano resonances - realization of a microwave Floquet experiment. Master's thesis, Philipps-Universität Marburg, 2010.

[4] C. Mahaux and H. A. Weidenmüller. *Shell-Model Approach to Nuclear Reactions*. North-Holland, Amsterdam, 1969.

[5] Stefan Gehler, Ulrich Kuhl, Hans-Jürgen Stöckmann, Steffen Löck, Arnd Bäcker, and Roland Ketzmerick. Experimental realization of resonance assited tunneling. *to be published*, 2013.

[6] Stefan Gehler, Bernd Köber, and Ulrich Kuhl. Channel correlation in transport through chaotic wave mechanical system. *to be published*, 2013.

[7] S. Gehler, T. Tudorovskiy, C. Schindler, U. Kuhl, and H.-J. Stöckmann. Microwave realisation of a periodically driven system, 2013. arXiv:1302.1289, accepted at New J. of Physics.

[8] Hojeong Kwak, Younghoon Shin, Songky Moon, and Kyungwon An. Observation of resonance-assisted dynamical tunneling in an asymmetric microcavity, 2013. arXiv:1305.6019.

[9] H.-J. Stöckmann. *Quantum Chaos - An Introduction*. University Press, Cambridge, 1999.

[10] M. L. Mehta. *Random Matrices. 2nd edition*. Academic Press, San Diego, 1991.

[11] R. Schäfer, T. Gorin, T. H. Seligman, and H.-J. Stöckmann. Correlation functions of scattering matrix elements in microwave cavities with strong absorption. *J. Phys. A*, 36:3289, 2003.

[12] P. A. Lee and T. V. Ramakrishnan. Disordered electronic systems. *Rev. Mod. Phys.*, 57:287, 1985.

[13] P. A. Lee and A. Douglas Stone. Universal conductance fluctuations in metals. *Phys. Rev. Lett.*, 55:1622–1625, 1985.

[14] D Agassi, H.A Weidenmüller, and G Mantzouranis. The statistical theory of nuclear reactions for strongly overlapping resonances as a theory of transport phenomena. *Physics Reports*, 22(3):145 – 179, 1975.

[15] J. J. M. Verbaarschot, H. A. Weidenmüller, and M. R. Zirnbauer. Grassmann integration in stochastic quantum physics: The case of compound-nucleus scattering. *Phys. Rep.*, 129:367, 1985.

[16] G. L. Celardo, F. M. Izrailev, V. G. Zelevinsky, and G. P. Berman. Open system of interacting fermions: Statistical properties of cross sections and fluctuations. *Phys. Rev. E*, 76:031119, 2007.

[17] G. L. Celardo, F. M. Izrailev, S. Sorathia, V.G. Zelevinsky, and G. P. Berman. Continuum shell model: From Ericson to conductance fluctuations. In P. Dnielewicz, P. Peicuch, and V. Zelevinsky, editors, *Semi-Classical Approximation in Quantum Mechanics. In: Mathematical Physics and Applied Mathematics 7, Contemporary Mathematics 5. Dordrecht etc.*, volume 995 of *AIP Conference Proceedings*, page 75. Springer, East Lansing, Michigan, 2008.

[18] G. Casati, B. V. Chirikov, F. M. Izrailev, and J. Ford. Stochastic behavior of a quantum pendulum under a periodic perturbation. In G. Casati and J. Ford, editors, *Stochastic Behaviour in Classical and Quantum Hamiltonian Systems*, Volta mem. Conf. , Como 1977, Lect. Notes Phys. 93, page 334, Berlin, 1979. Springer.

[19] S. Fishman, D. R. Grempel, and R. E. Prange. Chaos, quantum recurrences and Anderson localization. *Phys. Rev. Lett.*, 49:509, 1982.

[20] D. L. Shepelyansky. Localization of diffusive excitation in multi-level systems. *Physica D*, 28:103, 1987.

[21] P. M. Koch. Microwave "ionization" of excited hydrogen atoms: How non-classical local stability brought about by scarred matrix states is affected by broadband noise and by varying the pulse envelope. *Physica D*, 83:178, 1995.

[22] F. L. Moore, J. C. Robinson, C. F. Bharucha, P. E. Williams, and M. G. Raizen. Observation of dynamical localization in atomic momentum transfer: A new testing ground for quantum chaos. *Phys. Rev. Lett.*, 73:2974, 1994.

[23] C. F. Bharucha, J. C. Robinson, F. L. Moore, B. Sundaram, Q. Niu, and M. G. Raizen. Dynamical localization of ultracold sodium atoms. *Phys. Rev. E*, 60:3881, 1999.

[24] H. G. Schuster. *Deterministic Chaos: An Introduction*. Physik Verlag, Weinheim, 1984.

[25] A. Bäcker and R. Schubert. Amplitude distribution of eigenfunctions in mixed systems. *J. Phys. A*, 35:527, 2002.

[26] A. Bäcker and R. Schubert. Autocorrelation function of eigenstates in chaotic and mixed systems. *J. Phys. A*, 35:539, 2002.

[27] Denis Ullmo, Maurice Grinberg, and Steven Tomsovic. Near-integrable systems: Resonances and semiclassical trace formulas. *Phys. Rev. E*, 54:136–152, 1996.

[28] C. Dembowski, H.-D. Gräf, A. Heine, T. Hesse, H. Rehfeld, and A. Richter. First experimental test of a trace formula for billiard systems showing mixed dynamics. *Phys. Rev. Lett.*, 86:3284, 2001.

[29] M. Kopp and H. Schomerus. Fractal Weyl laws for quantum decay in dynamical systems with a mixed phase space. *Phys. Rev. E*, 81:026208, 2010.

[30] Martin J Körber, Matthias Michler, Arnd Bäcker, and Roland Ketzmerick. Hierarchical fractal weyl laws for chaotic resonance states in open mixed systems. *arXiv preprint arXiv:1304.2662*, 2013.

[31] A. Bäcker, R. Ketzmerick, S. Löck, M. Robnik, G. Vidmar, R. Höhmann, U. Kuhl, and H.-J. Stöckmann. Dynamical tunneling in mushroom billiards. *Phys. Rev. Lett.*, 100:174103, 2008.

[32] L. Bittrich. *Flooding of Regular Phase Space Islands by Chaotic States*. PhD thesis, Technische Universität Dresden, 2010.

[33] G. Binnig, H. Rohrer, Ch. Gerber, and E. Weibel. Surface studies by scanning tunneling microscopy. *Phys. Rev. Lett.*, 49:57–61, 1982.

[34] George Gamow. Zur quantentheorie des atomkernes. *Zeitschrift für Physik*, 51(3-4):204–212, 1928.

[35] Claude Cohen-Tannoudji, Bernard Diu, and Franck Laloë. *Quantenmechanik*. Walter de Gruyter, Berlin, 2007.

[36] L. D. Landau and E. M. Lifshitz. *Quantum Mechanics: (Nonrelativistic Theory). In: Theoretical Physics 3.* Pergamon Press, Oxford, London, Edinburgh, 1965.

[37] A. Messiah. *Quantum Mechanics, Volume I*. North-Holland, Amsterdam, 1961.

[38] M. J. Davis and E. J. Heller. Quantum dynamical tunneling in bound states. *J. Chem. Phys.*, 75:246, 1981.

[39] James D. Hanson, Edward Ott, and Thomas M. Antonsen. Influence of finite wavelength on the quantum kicked rotator in the semiclassical regime. *Phys. Rev. A*, 29:819–825, 1984.

[40] Steffen Löck, Arnd Bäcker, Roland Ketzmerick, and Peter Schlagheck. Regular-to-chaotic tunneling rates: From the quantum to the semiclassical regime. *Phys. Rev. Lett.*, 104:114101, 2010.

[41] Olivier Brodier, Peter Schlagheck, and Denis Ullmo. Resonance-assisted tunneling in near-integrable systems. *Phys. Rev. Lett.*, 87:064101, 2001.

[42] O. Brodier, P. Schlagheck, and D. Ullmo. Resonance-assisted tunneling. *Ann. Phys.*, 300:88, 2002.

[43] Arnd Bäcker, Roland Ketzmerick, and Steffen Löck. Direct regular-to-chaotic tunneling rates using the fictitious-integrable-system approach. *Physical Review E*, 82(5):056208, 2010.

[44] I. C. Percival. Regular and irregular spectra. *J. Phys. B*, 6:229, 1973.

[45] M. V. Berry. Regular and irregular semiclassical wavefunctions. *J. Phys. A*, 10:2083, 1977.

[46] H.-J. Stöckmann and P. Šeba. The joint energy distribution function for the Hamiltonian $H = H_0 - iWW^\dagger$ for the one-channel case. *J. Phys. A*, 31:3439, 1998.

[47] John David Jackson. Classical electrodynamics. 1998.

[48] J. Stein, H.-J. Stöckmann, and U. Stoffregen. Microwave studies of billiard Green functions and propagators. *Phys. Rev. Lett.*, 75:53, 1995.

[49] J. Barthélemy, O. Legrand, and F. Mortessagne. Complete S-matrix in a microwave cavity at room temperature. *Phys. Rev. E*, 71:016205, 2005.

[50] B. Köber, U. Kuhl, H.-J. Stöckmann, T. Gorin, D. V. Savin, and T. H. Seligman. Microwave fidelity studies by varying antenna coupling. *Phys. Rev. E*, 82:036207, 2010.

[51] Bruno K. Meyer. native copper oxide on copper. *private communication*, 2013.

[52] A. Potzuweit, T. Weich, S. Barkhofen, U. Kuhl, H.-J. Stöckmann, and M. Zworski. Weyl asymptotics: From closed to open systems. *Phys. Rev. E*, 86:066205, 2012.

[53] U. Kuhl, R. Höhmann, J. Main, and H.-J. Stöckmann. Resonance widths in open microwave cavities studied by harmonic inversion. *Phys. Rev. Lett.*, 100:254101, 2008.

[54] Steffen Löck and Ulrich Kuhl. numerical tunnelingrates. *private communication*, 2013.

[55] U. Kuhl. Microwave scattering on complex systems, 2008. Habilitationsschrift, Philipps-Universität Marburg.

[56] U. Kuhl, H.-J. Stöckmann, and R. Weaver. Classical wave experiments on chaotic scattering. *J. Phys. A*, 38:10433, 2005.

[57] D. Dubbers and H.-J. Stöckmann. *Quantum Physics: The Bottom-Up Approach*. Springer, Berlin Heidelberg, 2013.

[58] Christopher Eltschka and Peter Schlagheck. Resonance-and chaos-assisted tunneling in mixed regular-chaotic systems. *Phys. Rev. Lett.*, 94(1):014101, 2005.

[59] Steven Tomsovic, Maurice Grinberg, and Denis Ullmo. Semiclassical trace formulas of near-integrable systems: resonances. *Phys. Rev. Lett.*, 75(24):4346–4349, 1995.

[60] I. Rotter. A non-Hermitian Hamilton operator and the physics of open quantum systems. *J. Phys. A*, 42:153001, 2009.

[61] C. H. Lewenkopf and H. A. Weidenmüller. Stochastic versus semiclassical approach to quantum chaotic scattering. *Ann. Phys. (N.Y.)*, 212:53, 1991.

[62] N. Lehmann, D. Saher, V. V. Sokolov, and H.-J. Sommers. Chaotic scattering: the supersymmetry method for large number of channels. *Nucl. Phys. A*, 582:223, 1995.

[63] H. P. Baltes and E. R. Hilf. *Spectra of Finite Systems*. BI-Wissenschaftsverlag, Mannheim, 1976.

[64] W. T. Lu, S. Sridhar, and M. Zworski. Fractal Weyl laws for chaotic open systems. *Phys. Rev. Lett.*, 91:154101, 2003.

[65] F. Haake. *Quantum Signatures of Chaos. 2nd edition*. Springer, Berlin, 2001.

[66] H.-J. Stöckmann and J. Stein. "Quantum" chaos in billiards studied by microwave absorption. *Phys. Rev. Lett.*, 64:2215, 1990.

[67] O. Bohigas, M. J. Giannoni, and C. Schmit. Characterization of chaotic spectra and universality of level fluctuation laws. *Phys. Rev. Lett.*, 52:1, 1984.

[68] R. Schäfer, H.-J. Stöckmann, T. Gorin, and T. H. Seligman. Experimental verification of fidelity decay: From perturbative to Fermi golden rule regime. *Phys. Rev. Lett.*, 95:184102, 2005.

[69] Torleif Ericson. Fluctuations of nuclear cross sections in the "continuum" region. *Phys. Rev. Lett.*, 5:430–431, 1960.

[70] T. Ericson. A theory of fluctuations in nuclear cross sections. *Ann. Phys. (N.Y.)*, 23:390, 1963.

[71] T. Ericson and T. Mayer-Kuckuk. Fluctuations in nuclear reactions. *Ann. Rev. Nucl. Sci.*, 16:183, 1966.

[72] E. Persson, I. Rotter, H.-J. Stöckmann, and M. Barth. Observation of resonance trapping in an open microwave cavity. *Phys. Rev. Lett.*, 85:2478, 2000.

[73] T. Gorin and T. H. Seligman. Signatures of the correlation hole in total and partial cross sections. *Phys. Rev. E*, 65:026214, 2002.

[74] R. Blümel and U. Smilansky. A simple model for chaotic scattering. II. Quantum mechanical theory. *Physica D*, 36:111, 1989.

[75] E. Doron, U. Smilansky, and A. Frenkel. Experimental demonstration of chaotic scattering of microwaves. *Phys. Rev. Lett.*, 65:3072, 1990.

[76] H. Alt, H.-D. Gräf, H. L. Harney, R. Hofferbert, H. Lengeler, A. Richter, P. Schardt, and H. A. Weidenmüller. Gaussian orthogonal ensemble statistics in a microwave stadium billiard with chaotic dynamics: Porter-Thomas distribution and algebraic decay of time correlations. *Phys. Rev. Lett.*, 74:62, 1995.

[77] R. A. Méndez-Sánchez, U. Kuhl, M. Barth, C. H. Lewenkopf, and H.-J. Stöckmann. Distribution of reflection eigenvalues in absorbing chaotic microwave cavities. *Phys. Rev. Lett.*, 91:174102, 2003.

[78] U. Kuhl, M. Martínez-Mares, R. A. Méndez-Sánchez, and H.-J. Stöckmann. Direct processes in chaotic microwave cavities in the presence of absorption. *Phys. Rev. Lett.*, 94:144101, 2005.

[79] T. Tudorovskiy, R. Höhmann, U. Kuhl, and H.-J. Stöckmann. On the theory of cavities with point-like perturbations. Part I: General theory. *J. Phys. A*, 41:275101, 2008.

[80] T. Tudorovskiy, U. Kuhl, and H.-J. Stöckmann. Singular statistics revised. *New J. of Physics*, 12:123021, 2010.

[81] T. Tudorovskiy, S. Gehler, U. Kuhl, and H.-J. Stöckmann. Time-dependent point-like perturbations. to be published, 2013.

[82] O. Zinke and H. Brunswig. *Lehrbuch der Hochfrequenztechnik, Band 1 (Hochfrequenzfilter, Leitungen, Antennen)*. Springer Verlag, 1986.

[83] R. Feynmam, R. Leighton, and M. Sands. *The Feynman Lectures on Physics, vol. 2*. Addison Wesley, Reading, Mass, USA, 1977.

[84] V. P. Maslov and N. V. Fedoriuk. *Semi-Classical Approximation in Quantum Mechanics*. Reidel, Dordrecht, 1981.

[85] B. Eckhardt. Quantum mechanics of classically non-integrable systems. *Phys. Rep.*, 163:205, 1988.

[86] H. G. Schuster. *Deterministisches Chaos*. VCH Verlagsgesellschaft, Weinheim, 1994.

[87] Thomas Klinker, Werner Meyer-Ilse, and Werner Lauterborn. Period doubling and chaotic behavior in a driven toda oscillator. *Physics Letters A*, 101:371–375, 1984.

[88] Paul S. Linsay. Period doubling and chaotic behavior in a driven anharmonic oscillator. *Phys. Rev. Lett.*, 47:1349–1352, 1981.

[89] E. Otten. *Repetitorium Experimentalphysik*. Springer, 2003.

[90] M. Allgaier. Microwave studies on quantum graphs, 2012. Bachelor Thesis, Philipps-Universität Marburg.

[91] T. Kottos and U. Smilansky. Quantum chaos on graphs. *Phys. Rev. Lett.*, 79:4794, 1997.

[92] T. Kottos and U. Smilansky. Quantum graphs: a simple model for chaotic scattering. *J. Phys. A*, 36:3501, 2003.

[93] O. Hul, S. Bauch, P. Pakoñski, N. Savytskyy, K. Życzkowski, and L. Sirko. Experimental simulation of quantum graphs by microwave networks. *Phys. Rev. E*, 69:056205, 2004.

[94] O. Hul, M. Ławniczak, S. Bauch, A. Sawicki, M. Kuś, and L. Sirko. Are scattering properties of graphs uniquely connected to their shapes? *Phys. Rev. Lett.*, 109:040402, 2012.

[95] D. Waltner and U. Smilansky. Quantum graphs with time dependent bond lengths, 2013. Talk on DPG spring session DY 26.7, DPG Verhandlungen.

[96] U. Fano. Sullo spettro di assorbimento dei gas nobili presso il limite dello spettro d'arco. *Nuov. Cim.*, 12:154, 1935.

[97] U. Fano. Effects of configuration interaction on intensities and phase shifts. *Phys. Rev.*, 124:1866, 1961.

[98] Hans-Jürgen Stöckmann. opening a one dimensional box by a realsitic absorber. *private communication*, 2013.

[99] L.D. Landau, E.M. Lifschitz, and P. Ziesche. *Lehrbuch der theoretischen Physik, I Mechanik*. Harri Deutsch, 1997.

Acknowledgements

I thank everybody who contributed to the succeed of this thesis. Especially I would like to thank the following persons:

Prof. Dr. U. Kuhl for the choice of the topics, all the suggestions concerning measurements and data analyze, for giving me the opportunity to take part in many conferences and events and the friendly supervision not only during my time in Nice,

Prof. Dr. H.-J. Stöckmann for many fruitful discussions, the support with the theory, the substantial feedback to my work and that he often preferred to discuss physical problems instead of going swimming,

Prof. Dr. B. Eckhardt as the second referee for his kind interest in this work,

Prof. Dr. Roland Ketzmerick, Dr. Arnd Bäcker and Dr. Steffen Löck for the fruitful and nice collaboration within the framework of the tunneling experiments and the stays in Dresden,

Dr. T. Tudorovskiy for the helpful discussions about the results of the Floquet experiment,

Dr. L. Celardo, Dr. M. Miski-Oglu, Dr. B. Dietz, Prof. Dr. L. Kaplan, Prof. Dr. S. Rotter, Prof. Dr. F. Mortesagne, Prof. Dr. O. Legrande, Dr. S. Wimberger, Dr. W. Wustmann and all the other discussion partners at many conferences who participated me in their knowledge, which gave a substantial progress in the understanding of my topics,

My colleagues Sonja Barkhofen, Markus Allgaier, Kristof Beck, Julian Böhm, Otto Dietz, Bernd Köber and Tobias Weich of the quantum chaos group in Marburg for the pleasant working atmosphere, reading this manuscript and the nice time we had in our small offices,

The members of the electronic workshop, especially Carsten Schindler, Matthias Born and Clemens Stieler for many versions of the Floquet system, short-termed help and of course for the rescue of the Agilent,

The members of the mechanic workshop for the help with finding affordable copper and the recovery of believed lost knowledge of CNC control units,

My parents and grandparents for many phone calls, their lending ears and of course for their moral support,

My brother Jan for diversificating conversations, not always about physics,

My former physic teacher Axel Landmann for motivating me to study physics,

My dear girlfriend Sonia for all her patience, bearing my bad moods and for supporting my work all the time.